2022

Studies of *Staphylococcus aureus'* cell cycle:

New approaches for automated analysis

Bruno M. Saraiva

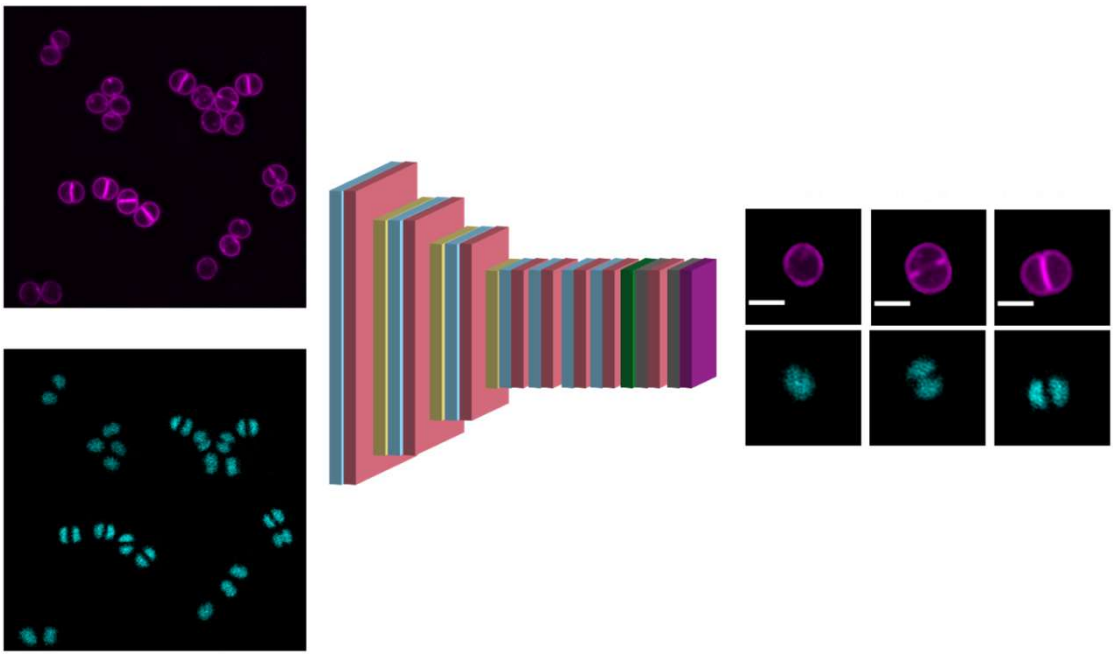

Dissertation presented to obtain the **Ph.D degree in**

Molecular Biosciences

Oeiras, May, 2022

Studies of *Staphylococcus aureus*' cell cycle:

New approaches for automated analysis

Bruno Manuel Santos Saraiva

Dissertation presentation to obtain the PhD degree in Molecular Biosciences

Instituto de Tecnologia Química e Biológica
António Xavier | Universidade Nova de Lisboa

Oeiras, May 2022

Financial Support from European Research Council through grant ERC-2017-CoG-771709 and Doctoral Program of Fundação para a Ciência e a Tecnologia (FCT)
PhD grant - SFRH/BD/147052/2019

Work performed at:

Bacterial Cell Biology Laboratory
Instituto de Tecnologia Química e Biológica António Xavier
Av. da República (EAN)
2780-157 Oeiras – Portugal
Tel: +351-214469548
Fax: +351-214469549

Supervisor:

Dr. Mariana G. Pinho, Instituto de Tecnologia Química e Biológica António Xavier, Universidade Nova de Lisboa, Oeiras, Portugal

Co-supervisors:

Ricardo Henriques, Instituto Gulbenkian de Ciência, Oeiras, Portugal MRC Laboratory for Molecular Cell Biology, University College London, London, United Kingdom

Fábio Fernandes, Centro de Química-Física Molecular and Institute of Nanoscience and Nanotechnology, Instituto Superior Técnico, University of Lisbon, Lisbon, Portugal; Institute for Bioengineering and Biosciences, Department of Bioengineering, Instituto Superior Técnico, University of Lisbon, Lisbon, Portugal

"The isolated man does not develop any intellectual power. It is necessary for him to be immersed in an environment of other men, whose techniques he absorbs during the first twenty years of his life. He may then perhaps do a little research of his own and make a very few discoveries which are passed on to other men. From this point of view the search for new techniques must be regarded as carried out by the human community as a whole, rather than by individuals."

Alan Turing

Acknowledgments

I would like to thank Professor Mariana Pinho, my thesis supervisor. I will always regard the opportunity to do my PhD in your laboratory as the major contribution to my career. Thank you for all the help, for always being available to discuss any idea or question that I had, for being open to discussion when I had a contrary opinion and, above all, thank you for always pushing to become a better scientist. Without a doubt, you taught me how to do research, how to pursue excellence and how to make a contribution to the scientific community.

I thank Dr. Ricardo Henriques and Dr. Fábio Fernandes, my co-supervisors, for always being available to discuss my work and for providing guidance when I was not sure how to proceed. This thesis would not be possible without your contribution and for that I am very thankful. I would also like to thank Dr. Jorge Carneiro and Dr. Ludwig Krippahl, for accepting to be part of my thesis committee and for the helpful discussions.

I would also like to thank Professor Sérgio Filipe, for always showing in interest in my work and for always being eager to ask questions. You taught me how we should always ask whatever question we might have and to search for the answers to those question. Your enthusiasm for science and knowledge is contagious and I hope to never lose it.

I also want to thank Professor Rui Vitorino and Professor António Barros. You gave me an opportunity to develop computational approaches for biological problems when I barely had any programming knowledge. With that opportunity, you allowed me to find my true passion in science and set me on my own scientific path.

I thank all the members of both Bacterial Cell Biology Laboratory and Bacterial Cell Surfaces and Pathogenesis Laboratory, former and present, for making it a fun environment to work in and for all the support throughout the years. I cannot name all the important contributions from everyone, but I have to thank Ambre Josselin, Ana Raquel Pereira, Andreia Duarte, Andreia Tavares, Helena Veiga, João Monteiro, Mário Ferreira, Marta Sporniak, Moritz Sorg, Nathalie Reichmann, Nils Meiresonne, Patricia Reed, Pedro Fernandes, Pedro M. Pereira, and Simon Schäper for being available to manually classify thousands of cells. Also, for your contributions to the development of eHooke, always being available to test it and provide feedback. Without your contribution my work would not be possible. To the old MGP2 members, you guys made it feel like we were a family. No matter the issue, work related or not, you were always there to help find a solution and when no solution was available, to laugh it off and move on. To Andreia, António, Leonor, Mário, Pedrinho and Sara for all the fun moments, the good and bad jokes, the relaxing moments and also for all the drama, because how dull would our lives be without it. Hopefully, the truck will be ready with everyone aboard when it is finally time for it to depart. I also want to thank my ITQB friends from the MolBioS PhD program, Ana, André, Andreia, Catarina, Guillem and Tiago. You guys rock and turned the PhD program into an amazing experience.

I also thank FCT and ERC for funding, ITQB-NOVA for providing me with a place to develop my research and for the MolBios PhD program. I want to thank NEUBIAS, its training schools and all the people I met there. I had the opportunity to attend one of the training schools and it was an enlightening experience.

I thank all my family and friends for their unconditional support. To Raquel, my wife, best friend, and soulmate. You make me the best

version of myself. Thank you for your support in everything I do. With you in my life, I feel like nothing is impossible. The love you make me feel from the moment I wake up to the moment I go to sleep is something that I never thought to be possible. Thank you for sharing your life with me, there is nothing that I cherish more than our “vidinha”. To our son, Gui. You are the purest joy in this world. You may still be one year old, but there are no words to describe how important you are to me. If there was a graphical dictionary, your face could be definition of love and happiness. Your excitement with the world is something marvellous. You truly make everything worth it. I am extremely grateful for being your father and I hope I can give you as much love and happiness as you do to me. I want to thank all my college friends for providing me with some of the best years of my life. To “Brunio” for always being there, for all the late-night coffees that turned into nights out, for all the nights we spent writing our master thesis, for all the support and especially for friendship. You may not remember it, but it was by writing those few dozen lines of code to analyse your microscopy images that I discovered the field of image analysis and gave me the confidence to pursue this PhD. To Fábio (Mitsu), thank you for always being there. No matter the time, you are always ready to talk and to help in whatever is needed, even to just make me laugh and forget about any problem I might be dealing with.

Um grande obrigado à minha avó Mila, é e sempre será a personificação de uma pessoa perfeita. Não há ninguém que ame tanto os seus e se preocupe tanto como a avó. Ensinou-me que fazer os outros felizes nos pode trazer felicidade e sentido de realização, é provavelmente a maior lição de vida que alguma vez tive e espero um dia conseguir ensinar isso ao Gui. À minha tia Adélia, o seu amor e carinho foram sempre uma constante na minha vida, esteve sempre disponível para tomar conta de mim e de todos. Foi, e é, um apoio essencial na nossa

vida. Por fim, um enorme obrigado aos meus pais. Sempre me permitiram sonhar e ensinaram-me a lutar pelos meus sonhos. Obrigado por todos os sacrifícios que fizeram para que eu pudesse ter as oportunidades que tive e por poder estar aqui hoje. Nada disto seria possível sem vocês! Mas acima de tudo obrigado por todo o amor incondicional que sempre me deram e que eu espero conseguir retribuir.

Index

Abbreviations and Acronyms

ANN	Artificial neural network
CFP	Cyan fluorescent protein
CLEM	Correlative light and electron microscopy
EM	Electron microscopy
Ery	Erythromycin
FR	Fluorescence ratio
GFP	Green fluorescent protein
IPTG	Isopropyl β-D-1-thiogalactopyranoside
MRSA	Methicillin-resistant *Staphylococcus aureus*
MSSA	Methicillin-sensitive *Staphylococcus aureus*
NN	Neural network
NTML	Nebraska transposon mutant library
PALM	Photoactivated localization microscopy
PBS	Phosphate-buffered saline
PBP	Penicillin-binding protein
PCA	Principal component analysis
PCC	Pearson's correlation coefficient
PG	Peptidoglycan
PMT	Photomultiplier tube
PSF	Point spread function
SEDS	Shape, elongation, division and sporulation
SEM	Scanning electron microscopy
SIM	Structured illumination microscopy
SMC	Structural maintenance of chromosomes
SMLM	Single molecule localization microscopy
STED	Stimulated emission depletion
STORM	Stochastic optical reconstruction microscopy

SVM	Support vector machine
TEM	Transmission electron microscopy
TSA	Tryptic soy agar
TSB	Tryptic soy broth
WGA	Wheat germ agglutinin

Abstract

Infections by antibiotic resistant bacteria are a rising problem in today's world health and are expected to become a major cause of death over the next decades. *Staphylococcus aureus* is a gram-positive bacterium that is often associated with antibiotic resistant infections. In order to find new strategies to deal with this type of infections, it is important to better understand how bacteria regulate their cell cycle. The study of cell cycle regulation is an understudied field in most bacteria, and it is of particular interest in pathogens such as *S. aureus*. We imaged by widefield fluorescence microscopy a mutant library containing a transposon insertion in virtually every non-essential gene of *S. aureus*, to find new key players involved in cell cycle regulation.

Fluorescence microscopy techniques have proved to be an essential tool for cell biology studies on bacterial cell cycle progression and morphogenesis. These techniques have developed over the years to a point where we are now able to acquire images at a speed and resolution previously unheard of. The bottleneck is now often the analysis of a large number of acquired images. To address this, there is a need for new automated tools capable of performing unbiased and reproducible analysis of microscopy images.

In this work we describe eHooke, a new microscopy image analysis framework optimized for automatic analysis of *S. aureus* cells' microscopy images. eHooke performs cell segmentation, defines subcellular regions (membrane, cytoplasm, and septum), measures both morphological and fluorescence features, and automatically classifies the cell cycle phase of individual cells. Considering that most cellular processes occur in specific phases of the cell cycle, it is important to study

morphological changes and proteins´ localization based on cell cycle progression. While in rod-shaped or ovococci bacteria, elongation can be used as a proxy for cell cycle progression, that is not the case for cocci, such as *S. aureus*. For the classification of cell cycle phases of individual cells, eHooke contains an artificial neural network trained to classify cells based on the morphology of the membrane and nucleoid. With eHooke, users are able to obtain biologically relevant information on morphological features of individual cells and cellular localization of proteins, in the context of the cell cycle.

To identify new key players in the regulation of *S. aureus* cell cycle, we imaged 1920 mutants from the Nebraska Transposon Mutant Library, which contains a transposon insertion in virtually every non-essential gene. We performed visual inspection of the acquired images to identify mutants with altered phenotypes related to chromosome segregation, cell morphology, and membrane or septum structure. In total we identified 233 out of the 1920 mutants with an altered phenotype. Then, using eHooke, we performed an automatic quantitative analysis to measure the median cell area and eccentricity of every mutant to identify those with highest deviation from the library mutants' average. We also used eHooke to automatically classify the frequency of cells in each phase of the cell cycle to identify mutants with an overrepresentation of cells in a specific phase, an indication of possible dysregulation of cell cycle progression.

Lastly, we challenged the existing model of division for *S. aureus* which suggested that cells divided in three alternating orthogonal planes over three consecutive division cycles. This model was originally proposed over four decades ago and implied the existence of a molecular mechanism to keep track of previous planes of division. However, this

mechanism remained elusive. In this work, we showed, in three different wildtype strains, that *S. aureus* cells do not always divide in three alternating orthogonal planes. Imaging of fluorescent derivatives of divisome proteins showed that the plane of division is always perpendicular to the previous one, which avoids bisection of the nucleoid since the chromosome segregates parallel to the closing septum. By measuring the angle between the divisome of sister cells, we showed that daughter cells can select any of a multitude of division planes that are perpendicular to the previous one and divide the cell in two identical halves, irrespective of its orientation in relation to the penultimate division plane. With these results, we showed that the proposed model for cell division in three orthogonal planes is not the rule in *S. aureus*.

This work contributed to the development of new tools that enable reproducible and accurate automated analysis of microscopy images and to a better understanding of cell cycle progression and cell division of the important pathogen *S. aureus*.

Resumo

As infeções causadas por bactérias resistentes a antibióticos são um problema grave em termos saúde mundial e é expetável que nas próximas décadas passem uma das principais causas de morte. *Staphylococcus aureus* é uma espécie bacteriana gram-positiva que é frequentemente associada a infeções resistentes a antibióticos. Para encontrar novas estratégias capazes de lidar com este problema, é importante expandir o nosso conhecimento sobre como as bactérias regulam a progressão do ciclo celular. O estudo da regulação do ciclo celular é uma área pouco estudada na maioria das bactérias, sendo particularmente importante em bactérias patogénicas como *S. aureus*. Usando microscopia de fluorescência, obtivemos imagens de uma biblioteca de mutantes de transposição em virtualmente todos os genes não essenciais de *S. aureus*.

As diferentes técnicas de microscopia de fluorescência são ferramentas importantes para o estudo de biologia celular na área da progressão do ciclo celular e morfogénese. Estas técnicas têm sido melhoradas ao longo dos anos e atualmente permitem adquirir imagens de microscopia a uma velocidade e resolução anteriormente impensáveis. O passo limitante é agora frequentemente a capacidade de analisar o elevado número de imagens adquiridas, pelo que se torna essencial o desenvolvimento de novos métodos automatizados de análise, capazes de analisar imagens de forma imparcial e reprodutível.

Neste trabalho descrevemos o eHooke, uma nova ferramenta para a análise de imagens de microscopia de *S. aureus*. O eHooke permite fazer a segmentação das imagens, definir regiões subcelulares de cada célula (membrana, citoplasma e septo), medir parâmetros morfológicos

e de fluorescência e quantificar a fase do ciclo celular de células individuais. Dado que muitos dos processos celulares ocorrem em fases específicas do ciclo celular, é importante estudar alterações morfológicas e a localização de proteínas no contexto da progressão do ciclo celular. Enquanto em bactérias com forma de bastonete ou ovococos, o alongamento das células pode ser usado como uma referência para a progressão do ciclo celular, o mesmo não acontece para bactérias esféricas como *S. aureus*. O eHooke permite a classificação das fases do ciclo celular de células individuais, através do uso de uma rede neuronal artificial que classifica as células com base na morfologia da membrana e do nucleoide. Com o eHooke, os utilizadores podem obter dados biologicamente relevantes sobre parâmetros morfológicos de células individuais ou sobre a localização de proteínas, no contexto das fases do ciclo celular.

Para identificar novas proteínas envolvidas na regulação do ciclo celular de *S. aureus*, adquirimos imagens dos 1920 mutantes da Nebraska Transposon Mutant Library, cada um dos quais contem a inserção de um transposão num gene não essencial. Foi feita uma inspeção visual das imagens adquiridas para identificar genes cuja inativação leva a fenótipos relacionados com segregação dos cromossomas, morfologia celular e alterações da membrana e do septo. No total, foram identificados 233 dos 1920 mutantes como tendo uma alteração de fenótipo. Em seguida, usando o eHooke, foi feita uma análise automática quantitativa para medir a mediana da área e excentricidade celular de cada mutante, de modo a identificar quais têm uma maior alteração em relação à média de todos os mutantes. Também usámos o eHooke para, de forma automática, quantificar a frequência de células em cada fase do ciclo celular e identificar mutantes com um aumento de células numa fase específica do

ciclo celular, o que poderá ser uma indicação de desregulação do ciclo celular.

Por último, questionámos o modelo vigente para o modo de divisão de *S. aureus* que propõe que as células se dividem em três planos ortogonais alternados ao longo de três ciclos de divisão. Este modelo foi inicialmente proposto há mais de quatro décadas e implica que haja um mecanismo molecular capaz de manter "memória" dos planos em que as células se dividiram. Contudo, este mecanismo continua desconhecido. Neste trabalho, mostrámos, em 3 estirpes diferentes, que células de *S. aureus* não se dividem sempre em três planos ortogonais alternados. A aquisição de imagens de derivados fluorescentes de proteínas do divisoma mostrou que um plano é sempre perpendicular ao anterior, o que evita a formação do septo sobre o nucleoide, dado que o eixo de segregação do cromossoma é sempre paralelo ao septo. Através de medições do ângulo entre o divisoma de pares de células filhas, que nos informam sobre a geometria do processo de divisão, mostrámos que estas podem ter como plano de divisão qualquer um dos planos perpendiculares ao anterior desde que divida a célula em duas metades idênticas, independentemente da orientação em relação ao penúltimo plano de divisão. Com estes resultados mostramos que a divisão de *S. aureus* não segue necessariamente o modelo proposto de divisão em três planos ortogonais alternados.

Este trabalho contribuiu para o desenvolvimento de novas ferramentas que permitem a análise automática e reprodutível de imagens de microscopia, bem como para uma melhor compreensão da progressão do ciclo celular e divisão celular em *S. aureus*.

CHAPTER I

General Introduction

Chapter I Summary

1. The origins of microscopy and microbiology

Humanity has always been fascinated with discovering what cannot normally be seen by eye. It started with trying to see far away objects, such as stars that illuminate the night sky, but soon evolved into trying to see smaller objects that were invisible to the naked eye. Galileo Galilei in 1610 found out that he could focus his telescope to visualize small objects up close. However, it was in 1665 that Robert Hooke published *Micrographia*, the first illustrated book on microscopy. In this work, even though Hooke´s main interests were in mechanics and physical sciences, he visualized biological samples under his microscope. It was in this work that he coined the term "cell" (Gest, 2004). Although microscopes were already being used to visualize living organisms, it was not until the 1670s that the existence of a living world hidden from us due to the small size of these organisms was first acknowledged. This was brought to light by Antonie van Leeuwenhoek, recognized as the first microbiologist who reported the observation of small organisms that were contained in a mouth swab (Figure 1A). Leeuwenhoek developed a simple and yet high magnification microscope (Figure 1B) that was used for this observation, marking the discovery of the bacterial world.

A

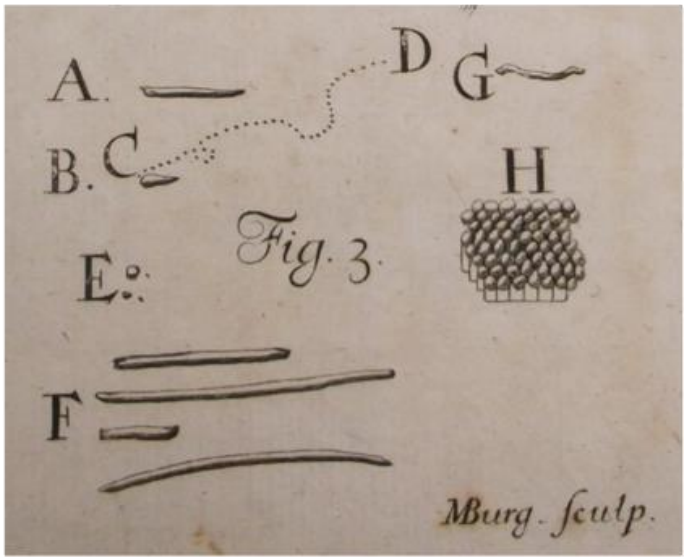

B

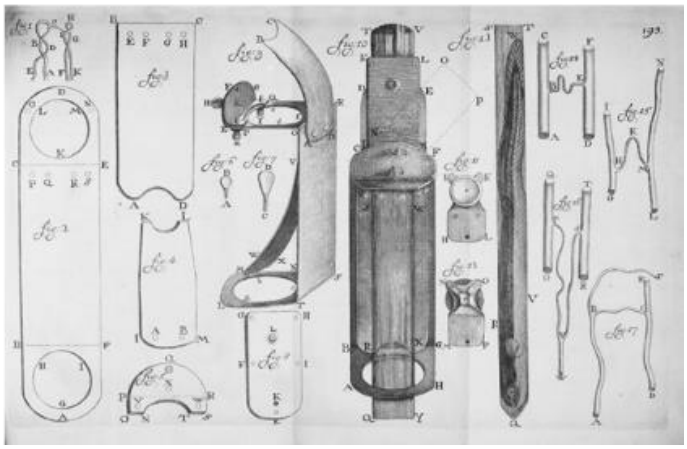

Figure 1 – Leeuwenhoek first observation of microorganisms, using its original microscope design. A – Drawings by Leeuwenhoek showing what he had observed at the microscope: several microorganisms with different shapes and even depicting movement of some of these organisms. **B** - Schematic of the design of one of van Leeuwenhoek's microscopes containing a high magnification lens and a sample holder. Image from (Leeuwenhoek, 1695).

2. Current microscopy techniques

Nearly four centuries after Hooke's and Leeuwenhoek's seminal work, microscopy remains a core technique for studying living organisms, especially when it comes to bacteria. Nowadays, imaging can be performed using several microscopy approaches such as widefield fluorescence microscopy, with its many super resolution modalities, and electron microscopy.

2.1 Widefield fluorescence microscopy

Widefield fluorescence microscopy is based on the usage of a fluorophore that is integrated in the sample, such as a fluorescent protein or organic dye. The fluorophore is excited using a light-source emitting light in a specific wavelength and, after excitation, it emits fluorescence. The emitted fluorescence can then be captured through the usage of a digital camera or visualized at the microscope (Figure 2). While the concept of fluorescence microscopy is simple, it brings its own challenges. The first and most important is that the resolution that we can achieve is limited by the light diffraction limit (Rayleigh, 1896). Second, a fluorophore can only be excited for a certain amount of time before it starts to bleach, eventually becoming unable to emit more fluorescence even if continuously excited. Third, illuminating a biological sample with light to excite its fluorophores can introduce phototoxicity to the sample and affect its cellular processes.

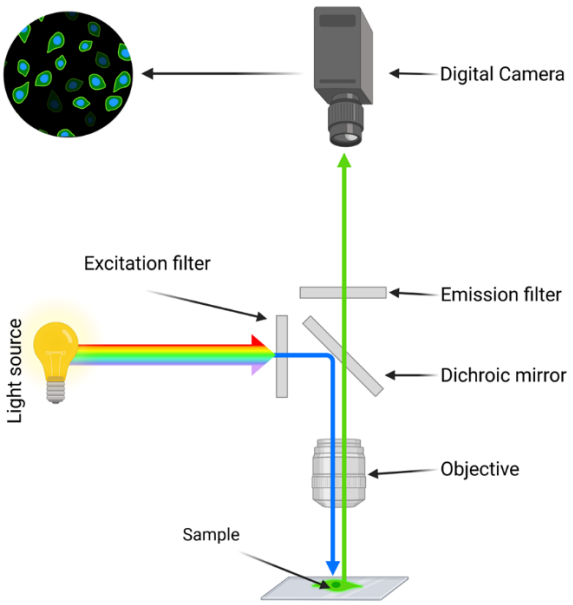

Figure 2 – Schematic of a typical fluorescence microscopy setup. The filtered excitation light is reflected by the dichroic mirror and excites the sample. The sample emits light in a different wavelength which goes through the dichroic mirror and is then filtered by the emission filter. The resulting light reaches the camera, generating a digital image of the illuminated sample. Adapted from "Light path (fluorescence microscopy)", by BioRender.com (2022).

2.2 Surpassing the light diffraction limit

As bacteria have a small size, imaging of these organisms is often hindered by the resolution achievable using conventional microscopy techniques, which are limited by the light diffraction limit (Rayleigh, 1896). However, over the last years there has been an effort to develop ways of circumventing this limit and achieve higher resolutions. The first effort to create a super resolution technique was Stimulated Emission-Depletion (STED) microscopy (Klar et al., 2000; Wichmann and Hell, 1994), whose inventor was awarded a Nobel prize. This technique is

based on the usage of two simultaneous lasers: one for excitation and one donut-shaped laser for depletion. The first laser will excite the molecules to emit fluorescence while the second is responsible for getting them back to the ground state (Figure 3A). Due to its donut shape, this will leave only the molecules in the central spot excited and emitting fluorescence, making it possible to obtain a resolution between 30-80nm. A second technique that can be used to obtain super resolution is Structured Illumination Microscopy (SIM). Throughout the years there have been several implementations of this approach but all of them are based on applying a set of illumination patterns to the sample. This results in interference patterns, which contain information regarding the structural patterns of the sample (Figure 3B). By analysing the Fourier transforms of the interference patterns it is possible to obtain super resolved structural information of the sample (Frohn et al., 2000; Gustafsson, 2000, 2005; Heintzmann and Cremer, 1999). This approach can achieve an improvement in resolution of about two times (Frohn et al., 2000; Gustafsson, 2000) and it can be further improved by utilizing non-linear fluorescence responses (Gustafsson, 2005). The third modality of super resolution is based on single-molecule localization microscopy (SMLM). There are two main techniques that use this principle: Photoactivated Localization Microscopy (PALM) (Betzig et al., 2006) and Stochastic Optical Reconstruction Microscopy (STORM) (Bates et al., 2007; Rust et al., 2006), with the former resulting in a Nobel prize to the author. The key for this method is the use of photoactivatable fluorophores that can transition stochastically between bright and dark emission states when exposed to specific light wavelengths. Activation is kept at a low level to guarantee that only a few fluorophores are fluorescing at any given time. Thousands of frames are acquired, and the position of each single molecule is calculated with high accuracy by fitting the intensity profile

to a Gaussian function, approximating to the microscope's point spread function (PSF). The final image is then reconstructed using the localizations detected in all acquired frames (Figure 3C). Using this method, it is possible to resolve objects as close to each other as 10nm (Betzig et al., 2006; Rust et al., 2006).

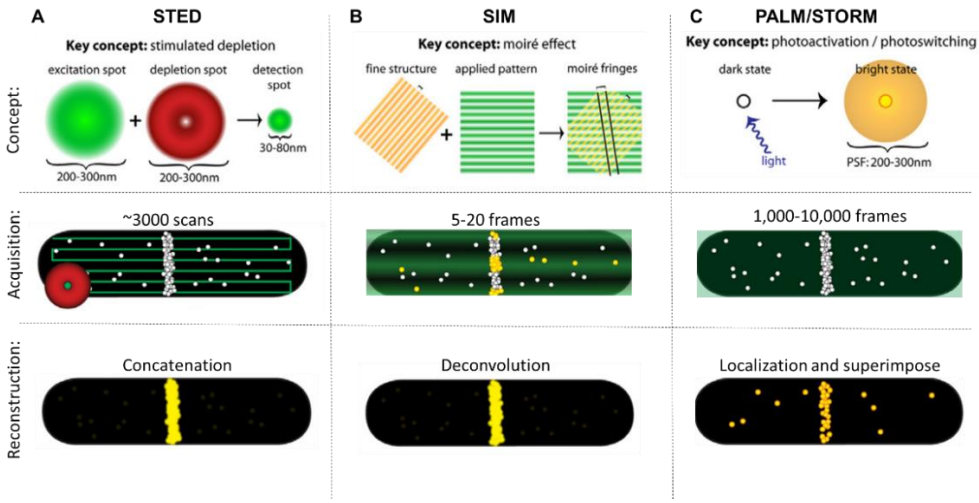

Figure 3 – Comparison between different super resolution microscopy approaches. A – STED imaging is based on applying both an excitation laser beam and a donut-shaped depletion beam that returns the fluorophores to the ground state. This results in only the fluorophores in the central region of the beams emitting fluorescence. Acquisition is performed by scanning the full sample and then reconstruction the individual scans in a super-resolved image. **B** – SIM imaging is performed by applying several illumination patterns and then extracting spatial information by using Fourier transforms. This information is then combined onto a single image with 2 times the original resolution. **C** –PALM and STORM, both methods of single-molecule localization microscopy, are based on the stochastic photoactivation of fluorophores. Thousands of frames are acquired where only a few molecules are activated, and for each molecule a diffraction-limited spot is detected which is then fitted to a Gaussian function. The final super resolution image is reconstructed by superimposing all the single molecule detections onto a single frame. Image adapted from (Coltharp and Xiao, 2012).

2.3 Electron microscopy

Electron microscopy (EM) can achieve better resolutions than conventional light microscopy techniques. This is mainly due to EM using electrons instead of light and the fact that electrons have a much smaller wavelength than light. The most common techniques used are Transmission Electron Microscopy (TEM) and Scanning Electron Microscopy (SEM). The former requires an ultrathin sample, less than 100nm thick, and generates an image from the electrons being transmitted through the sample. SEM is based on the scanning of the sample's surface and tracking the loss of energy of the electron beam when interacting with the sample.

While these techniques can provide the users with highly resolved images it is difficult to label specific proteins to be visualized using EM. Moreover, fixation of the sample is typically required, making it impossible to perform live cell imaging which can be essential to follow and understand dynamic processes happening in cells.

3. Acquiring an optimal image

To image bacteria there are several possible microscopy techniques available. Besides the ones discussed in this work, there are others such as confocal microscopy or scanning probe microscopy that can also be used. When it comes to choosing the technique that provides the best possible image, there is probably no universal right answer. Each technique has its own advantages and disadvantages and the choice of which one to use will depend on the biological question in study.

The choice of which microscopy technique to use can be thought in terms of a few different acquisition aspects: general overview of the sample vs specific labelling of a molecule, live-cell imaging vs fixed cells, spatial vs temporal resolution and acquisition time (Table 1). Regarding the first aspect, if the goal is to obtain an image of the full sample, without the need for a specific labelling, then EM may be the technique of choice as the obtained resolution is unparalleled. However, EM requires the sample to be fixed, making it incompatible with live-cell imaging, and as such EM cannot be used to image dynamic processes over time. Recently, a new approach was developed that combines fluorescence microscopy with electron microscopy, correlative light and electron microscopy (CLEM), which tries to provide the best of both worlds by combining label specific information from fluorescence microscopy with high-resolution structural information from EM (Hampton et al., 2016). However, this approach can take from 5 to 15 days to acquire and process the images, which makes it unfeasible for several applications (Hampton et al., 2016). Widefield fluorescence microscopy shines for imaging of live cells, as phototoxicity should be minimal, it allows specific labelling as well as the continuous imaging of a sample over a long time-lapse. Nonetheless, the spatial resolution might not be enough for certain applications and for

those cases, super resolution fluorescence microscopy methods can be used. If the only concern is to have the highest possible spatial resolution, either STED or SMLM are usually the answer, as both can provide a considerable increase in resolution when compared with widefield fluorescence microscopy, with SMLM achieving resolutions of up to 10nm (Betzig et al., 2006). However, as both methods require acquisition of thousands of either frames or scans, temporal resolution is lost. This is due not only to the time it takes to finish acquisition but also to the photodamage and photobleaching caused during acquisition. SIM imaging can provide a good balance between spatial and temporal resolution, as it requires a significantly smaller number of frames than single-molecule localization microscopy, while still typically providing a two-fold increase in spatial resolution.

Table 1 – Comparison between different microscopy techniques. Green check marks represent aspects in which the technique excels, yellow marks indicate that the technique is better than widefield fluorescence microscopy but not optimal and red crosses indicate that the technique struggles in that aspect.

	Spatial resolution	Temporal resolution	Specific Labelling	Live-cell Imaging
Electron Microscopy	✓	✗	✗	✗
Widefield Fluorescence Microscopy	✗	✓	✓	✓
Stimulated Emission-Depletion Microscopy	✓	✗	✓	✓
Structured Illumination Microscopy	✓	✓	✓	✓
Single-molecule Localization Microscopy	✓	✗	✓	✓

4. Extracting meaningful data from fluorescence microscopy images

Although we are now able to do high-throughput imaging of bacteria and have several microscopy techniques available, that can even surpass the light diffraction limit, proper analysis is key to extract meaningful data from those images. Therefore, performing single cell image analysis is crucial, as there is significant variation from cell to cell in several cellular processes. Manual analysis is possible using several available tools, such as ImageJ (Rueden et al., 2017) or Fiji, its distribution with several plugins included (Schindelin et al., 2012). However, to get a statistically meaningful measurement of a population of cells, for example of the effect of a mutation in cell morphology, measurements of a statistically significant number of cells are required (Kuwada et al., 2015). Doing this manually is time-consuming and not feasible for large scale studies, such as screenings of different compounds or of libraries of strains. Besides the fact that manual analysis is time consuming, it is also important to note that it might introduce user bias. For example, if two different users are measuring the area of cells in an image, how they perceive the cell boundaries might be different, resulting in different cell area measurements and creating reproducibility issues. Considering this, it is of utter importance to have reliable, fast, and easy to use tools that can automate this analysis.

5. The artificial intelligence revolution in microscopy image analysis

The recent boom in the machine learning field has been a powerful ally in advancing and improving microscopy image analysis. While more traditional machine learning techniques such as Principal Component Analysis (PCA) or Support-Vector Machine (SVM) have been widely used before, nowadays there has been an incredible development of new microscopy image analysis approaches thanks to the rapid development of deep learning techniques. Deep learning is a subtype of machine learning that tries to imitate the way humans acquire knowledge. In its simplest form, deep learning is a way to automate predictive analysis. Neural networks (NNs), a typical tool used in deep learning, are commonly used in a supervised manner by feeding training data along with the expected output to the network, which it then uses to train itself. After training, the network should be able to process images and generate the expected output (Figure 4). NNs can be used in a variety of different tasks for microscopy, ranging from image segmentation, classification, and restoration. In a recent work by Spahn and colleagues, the authors demonstrated the potential of several deep learning algorithms for the analysis of bacterial images (Spahn et al., 2021).

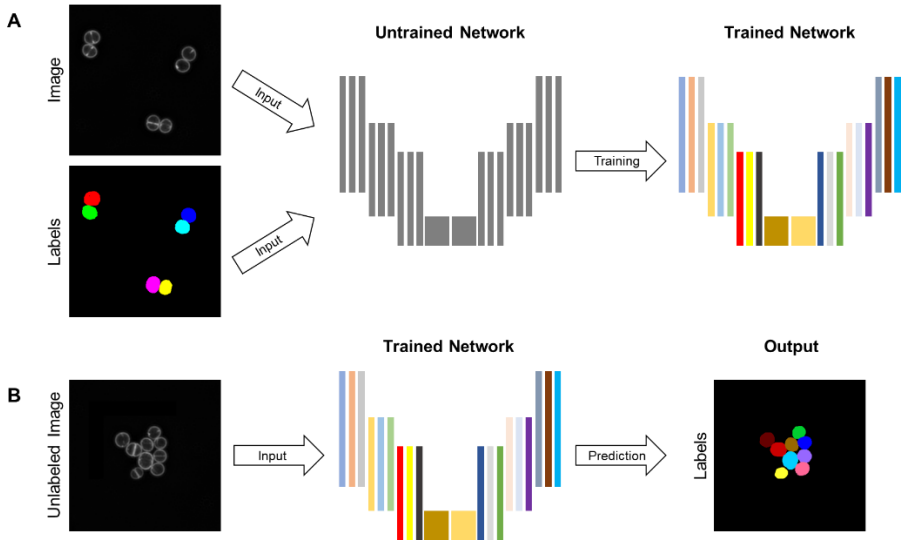

Figure 4 – Example workflow of a Convolution Neural Network used for instance segmentation. A - Training data, consisting of a microscopy image and a label image, with different labels for each cell, is fed to the neural network. The network will go through training and generate a trained network. **B** – The trained network can now be fed an unlabelled image and will generate a mask containing different labels for each cell enabling instance segmentation.

5.1 Image segmentation

Neural networks for segmentation are probably the most widely used type of NNs for microscopy image analysis. Among these, U-net is possibly the most commonly used architecture for image segmentation (Thévenaz et al., 1998). StarDist is a more recent network that excels in the segmentation of star-shaped objects (Schmidt et al., 2018; Weigert et al., 2020). Besides separating foreground from background, this network also performs instance segmentation. SplineDist is a new network architecture based on StarDist that instead of describing objects as star convex polygons, describes them as planar parametric spline curves, which makes this network more flexible and of general use (Mandal and Uhlmann, 2021).

5.2 Image classification

Besides their use for image segmentation, NNs are also powerful tools for automating classification of images or individual objects. An example of this type of networks is the R-CNN (Girshick et al., 2014). This network starts by generating bounding boxes for independent regions inside an image, then performs feature extraction of each region using a deep convolutional neural network and finally classifies each region based on the extracted features. Another network that performs object detection and classification is the YOLOv2 (Redmon and Farhadi). This network was shown in the work of Waithe and colleagues to have good performance in the classification of cell nuclei (Waithe et al., 2020).

5.3 Other uses of NNs in microscopy images

Image denoising is another challenging task where the usage of more traditional methods often falls short. This task encompasses the removal of noise signal from an image, to improve its signal-to-noise ratio. NNs such as CARE (Weigert et al., 2018) and Noise2Void (Krull et al., 2018) are powerful tools capable of performing image denoising and restoration. CARE is capable of restoring signal when using as low as 60-fold less photons during image acquisition than the required photons for an image with a good signal-to-noise ratio (Weigert et al., 2018). This network is also capable of generating super resolution images from diffraction limited images (Spahn et al., 2021). Noise2Void provides a way to perform denoising without having to train a network using noisy image pairs, allowing the training to occur on the actual image to be denoised. More recently, NNs are also being used to perform artificial labelling of cells, creating pseudo-fluorescence images from unlabelled cell images (Li et al., 2021).

5.4 Making deep learning available to the nonexpert scientific community

Although deep learning and NNs are a powerful tool for image analysis, their usage can still be challenging to the general scientific community. However, there have been efforts to make NNs available in an easy-to-use manner. ZeroCostDL4Mic provides Google Colab notebooks that implement several deep learning models, including all neural networks described above (von Chamier et al., 2021). These notebooks make the use of previously trained models easy and also provide a graphical user interface to make the retraining of these models easy for the general microscopy community. DeepImageJ is another project that focuses on making these techniques available as a plugin of the widely used ImageJ software (Gómez-de-Mariscal et al., 2021). Besides enabling the use of a vast library of provided pre-trained modules, DeepImageJ also allows the user to use their own custom models in ImageJ. The work from these projects, combined with all the available image analysis techniques and workflows, makes the analysis of bacteria microscopy images easier and more accessible, extending the possibilities of further studies in microbiology.

6. *Staphylococcus aureus* morphology and cell division

Since Leeuwenhoek´s seminal work, the development of microscopy techniques and microscopy image analysis tools has expanded our knowledge of the microbial world. Although the best studied bacterial species are either spherical (cocci) or rod shaped (bacilli), for example *Staphylococcus aureus* (Figure 5) and *Escherichia coli*, respectively, bacteria of several different shapes can be found in nature (Young, 2006). Morphology plays an important role in the fitness and adaptability of bacteria to the environment (Yang et al., 2016; Young, 2007). As such, it is important to understand the key players and mechanisms involved in determining and maintaining bacterial cell morphology during its cell cycle, especially in pathogenic bacteria such as *S. aureus*. While *S. aureus* is a common commensal organism, which can be present in the skin and nasopharynx of healthy hosts (Edwards et al., 2012; Otto, 2010), it can also act as a pathogen. This usually happens if there is a breach of the skin barrier or mucous membranes, leading to an invasive infection and potentially causing several medical conditions, ranging from minor skins lesions to more serious conditions such as bacteraemia, endocarditis or pneumonia (Tong et al., 2015). However, what truly makes *S. aureus* an important organism to study is its ability to develop antibiotic resistance (Worthington and Melander, 2013). According to the 2014 Review on Antimicrobial Resistance (O'Neill, 2014), by the year 2050 more than 10 million people are expected to die every year due to antibiotic resistant infections. Considering the impact of antibiotic resistant infections in human health, it is crucial to find new antimicrobial targets for new antibiotics than can help in controlling these infections. Given that morphology maintenance and cell cycle progression are essential for cell viability, the proteins and mechanisms

involved in these processes are potential prime targets for new antibiotics.

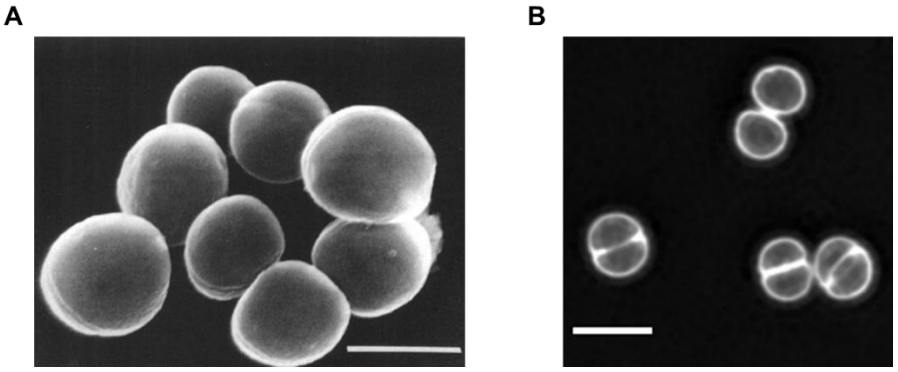

Figure 5 – *Staphylococcus aureus* cells have a spherical morphology. A - Scanning electron micrographs of *S. aureus* wildtype strain SAK-101. Reproduced from (Koyama, Yamada and Matsuhashi, 1977). **B –** Super resolution SIM images of membrane labelled (Nile red) *S. aureus* COL strain. Scale bars, 1 μm.

6.1 Keeping in shape

Peptidoglycan (PG) is a polymer consisting of glycans chains crosslinked by peptide bridges, that forms a mesh-like wall outside the plasma membrane of bacteria and protects cells from lysing due to turgor pressure. PG is thought to be the major determinant of bacterial cell morphology. This is evidenced by the fact that inhibition of PG synthesis results in loss of cell shape (Allan et al., 2009; Gilpin et al., 1973). Interestingly, while different bacteria have a wide range of different shapes, PG chemical structure was found to be relatively conserved in bacteria with different shapes (Vollmer et al., 2008). This suggests that differences in bacterial shape do not come from differences in the

chemical structure of PG, but from the temporal and spatial regulation of PG is synthesis and incorporation into the cell wall mesh.

In rod shaped bacteria such as *E. coli*, new PG synthesis is controlled by two protein complexes, the elongasome and the divisome. The elongasome is responsible for insertion of PG along the major axis of the cell and this process is coordinated through the actin-like protein MreB (van den Ent et al., 2014). The divisome is a protein complex that synthetises the septum leading to cell division, which is coordinated by the tubulin homologue FtsZ (Nogales et al., 1998). In ovococci bacteria, such as *Streptococcus pneumoniae*, that do not possess MreB, cell elongation is thought to be controlled by FtsZ, that in this case coordinates both elongation and septation (Pinho et al., 2013). *S. aureus* is a cocci and does not have a canonical elongasome machinery. However, it is capable of peripheral PG incorporation leading to a slight cell elongation (Monteiro et al., 2015) This process was shown to be dependent on RodA, a protein of the shape, elongation, division, and sporulation (SEDS) family, in coordination with the penicillin-binding protein PBP3, while PG septal synthesis, coordinated by FtsZ, is dependent on the activity of the SEDS protein FtsW and PBP1 (Reichmann et al., 2019).

6.2 The divisome protein complex of *S. aureus*

The divisome consists of several cell division proteins, including proteins responsible for PG synthesis at midcell leading to septation. Divisome assembly starts with the mid cell recruitment of FtsZ and its membrane anchors, forming a ring-like structure called the Z-ring (Rico et al., 2013). FtsA is a widely conserved protein in bacteria and is thought to be main membrane anchor for the Z-ring (Pichoff and Lutkenhaus,

2005). EzrA is a membrane protein that is thought to be a negative regulator of cell division as in its absence the frequency of Z-ring formations is increased (Levin et al., 1999). In *S. aureus* this protein forms a complex interaction network with both cytoplasmic and membrane proteins of the division machinery (Steele et al., 2011). After assembling of the Z-ring, the process of recruitment of downstream proteins starts, apparently following a hierarchical order where the recruitment of FtsW, PBP1 and DivIB, precedes the recruitment of MurJ and PBP2 (Monteiro et al., 2018). FtsW and PBP1 are key PG synthesis proteins that form a SEDS/PBP cognate pair which is also proposed to stabilize the divisome at midcell, as in its absence the divisome appears as multiple rings that synthetise lateral PG leading to elongation (Reichmann et al., 2019). DivIB, DivIC and FtsL form a complex that appears to be required for the recruitment of MurJ to midcell (Monteiro et al., 2018). In *S. aureus*, MurJ is the proposed flippase of the PG precursor lipid II. Its septal localization leads to transport of lipid II mostly at that location, directing PG synthesis to midcell (Monteiro et al., 2018).

6.3 *S. aureus* cell cycle

The assembly of the divisome and septum synthesis are key processes in the cell cycle of *S. aureus* (Figure 6), along with chromosome replication and segregation, and cell splitting. *S. aureus* cell cycle can be described as having 3 different phases (Monteiro et al., 2015). Phase 1 cells have the chromosome distributed all over the cytoplasm and lack a division septum. During this phase cells increase in volume and slightly elongate (Monteiro et al., 2015) and at the end the divisome starts to assemble. Then, MurJ arrives to the divisome and cells start to synthetise the septum, initiating Phase 2. During Phase 2, while there is an increase

in volume, there is no significant cell elongation (Monteiro et al., 2015). Finally, Phase 3 cells have a fully synthetised septum with the chromosome fully segregated into the two future daughter cells. During this phase the septum undergoes maturation and cells increase in volume and elongate once more (Monteiro et al., 2015). Phase 3 cells will then divide, in an extremely fast popping-like event that only takes milliseconds (Monteiro et al., 2015; Zhou et al., 2015), generating two new Phase 1 cells.

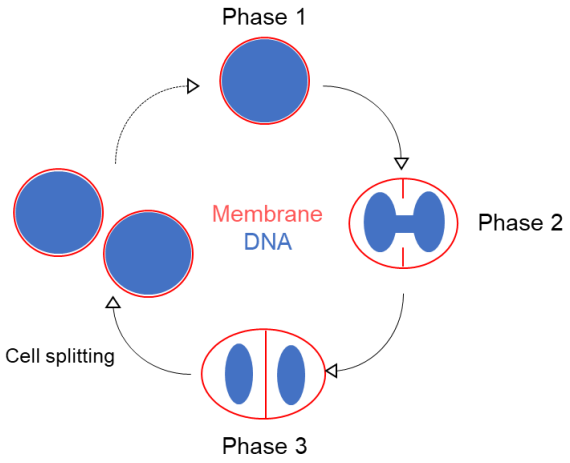

Figure 6 - Cell cycle progression in *Staphylococcus aureus.* The cell cycle of *S. aureus* can be described as three phases: Phase 1, when cells have recently divided, the chromosome is distributed all over the cytoplasm and septum synthesis has yet to start; Phase 2, when cells are undergoing septum synthesis; Phase 3, when cells have a fully synthetised septum and chromosome segregation has finished. Phase 3 cells will then split into two new Phase 1 daughter cells.

6.4 *S. aureus* mode of division

Both rod-shaped bacteria and ovococci cells divide in successive parallel planes, perpendicular to the major axis of the cells. However, this was thought to not be the case for *S. aureus,* based on light microscopy images of cells embedded in soft agar undergoing three consecutive divisions (Tzagoloff and Novick, 1977) and on the cubic packages seen in scanning electron microscopy images (Koyama et al., 1977). The proposed model for *S. aureus* was that division occurs in three alternating orthogonal planes over three consecutive division cycles (Figure 7).

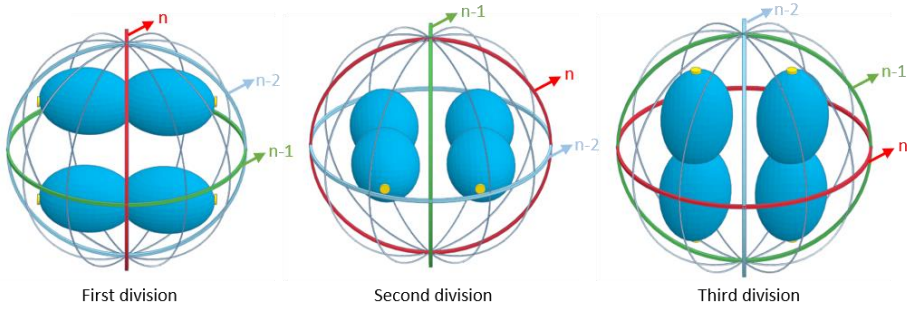

Figure 7 – Model of *S. aureus* division in three alternating orthogonal planes. Representation of *S. aureus* cell undergoing three consecutive divisions. The current division plane is represented in red (n), the previous one in green (n-1) and the one before in light blue (n-2). Chromosomes are represented in blue and origins of replication in yellow.

This mode of division is possibly shared by other cocci, such as *Micrococcus* luteus, which was shown to form cubic packets of cells, similar to *S. aureus* (Monodane et al., 1978; Yamada et al., 1975). Importantly, for this mode of division to be correct, cells must keep information regarding the previous division planes. However, a mechanism for this "memory" remains to be found. One of the proposed

mechanisms states that the large belt of peptidoglycan formed at the division site, that remains as orthogonal ribs after cell division, could signal the localization of the previous division planes (Turner et al., 2010). These scars of cell division could possibly be used as epigenetic information that ensure the orthogonality of the following division planes (Turner et al., 2010). Another proposed mechanism is that the junction of two scars could be used as a geometric cue for the axis in which chromosomes segregate (Veiga et al., 2011). *S. aureus* produces the nucleoid occlusion protein Noc, which inhibits the assembly of the divisome in its proximity (Wu and Errington, 2004). Since Noc was shown to preferably bind to origin-proximal half of the chromosome (Wu and Errington, 2004, 2011), segregation happening in the direction of the previous planes' junctions could release the inhibition of divisome assembly from the next orthogonal plane (Wu and Errington, 2004, 2011). Notably both proposed mechanisms rely on scars of previous divisions dividing cells in quadrants. However, this was shown to not be accurate (Figure 8), as the septum of *S. aureus* cell, upon splitting, does not generate a full hemisphere of each daughter cells but only approximately one third (Monteiro et al., 2015), which makes it less likely that scars can provide information on where the cell will divide next. Therefore, the mechanism for *S. aureus* division in three alternating orthogonal planes remains unknown.

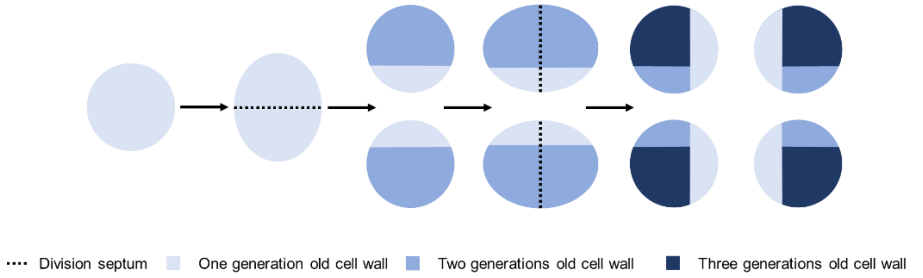

Figure 8 – *S. aureus* septum only generates one third of each daughter cell surface. *S. aureus* cells are approximately spherical at the beginning of the cell cycle and slightly elongate as the cell cycle progresses. Upon splitting of the mother cell there is no increase in the surface area of the previous septum, which becomes approximately one third of the surface area of each daughter cell (Monteiro et al., 2015).

7. Bibliography

Allan, E.J., Hoischen, C., and Gumpert, J. (2009). Bacterial L-forms. Advances in Applied Microbiology *68*, 1–39.

Bates, M., Huang, B., Dempsey, G.T., and Zhuang, X. (2007). Multicolor Super-resolution Imaging with Photo-switchable Fluorescent Probes. Science *317*, 1749.

Betzig, E., Patterson, G.H., Sougrat, R., Lindwasser, O.W., Olenych, S., Bonifacino, J.S., Davidson, M.W., Lippincott-Schwartz, J., and Hess, H.F. (2006). Imaging intracellular fluorescent proteins at nanometer resolution. Science *313*, 1642–1645.

von Chamier, L., Laine, R.F., Jukkala, J., Spahn, C., Krentzel, D., Nehme, E., Lerche, M., Hernández-Pérez, S., Mattila, P.K., Karinou, E., et al. (2021). Democratising deep learning for microscopy with ZeroCostDL4Mic. Nature Communications 2021 12:1 *12*, 1–18.

Coltharp, C., and Xiao, J. (2012). Superresolution microscopy for microbiology. Cellular Microbiology *14*, 1808.

Edwards, A.M., Massey, R.C., and Clarke, S.R. (2012). Molecular mechanisms of *Staphylococcus aureus* nasopharyngeal colonization. Molecular Oral Microbiology *27*, 1–10.

van den Ent, F., Izoré, T., Bharat, T.A.M., Johnson, C.M., and Löwe, J. (2014). Bacterial actin MreB forms antiparallel double filaments. ELife 2014;3:e02634.

Frohn, J.T., Knapp, H.F., and Stemmer, A. (2000). True optical resolution beyond the Rayleigh limit achieved by standing wave illumination. Proceedings of the National Academy of Sciences *97*, 7232–7236.

Gest, H. (2004). The discovery of microorganisms by Robert Hooke and Antoni van Leeuwenhoek, Fellows of The Royal Society. Notes and Records of the Royal Society of London *58*, 187–201.

Gilpin, R.W., Young, F.E., and Chatterjee, A.N. (1973). Characterization of a stable L-form of *Bacillus subtilis* 168. Journal of Bacteriology *113*, 486–499.

Girshick, R., Donahue, J., Darrell, T., and Malik, J. (2014). Rich feature hierarchies for accurate object detection and semantic segmentation Tech report. ArXiv.

Gómez-de-Mariscal, E., García-López-de-Haro, C., Ouyang, W., Donati, L., Lundberg, E., Unser, M., Muñoz-Barrutia, A., and Sage, D. (2021). DeepImageJ: A user-friendly environment to run deep learning models in ImageJ. Nature Methods 2021 18:10 *18*, 1192–1195.

Gustafsson, M.G.L. (2000). Surpassing the lateral resolution limit by a factor of two using structured illumination microscopy. Journal of Microscopy *198*, 82–87.

Gustafsson, M.G.L. (2005). Nonlinear structured-illumination microscopy: Wide-field fluorescence imaging with theoretically unlimited resolution. Proceedings of the National Academy of Sciences *102*, 13081–13086.

Hamoen, L.W., Meile, J.C., de Jong, W., Noirot, P., and Errington, J. (2006). SepF, a novel FtsZ-interacting protein required for a late step in cell division. Molecular Microbiology *59*, 989–999.

Hampton, C.M., Strauss, J.D., Ke, Z., Dillard, R.S., Hammonds, J.E., Alonas, E., Desai, T.M., Marin, M., Storms, R.E., Leon, F., et al. (2016). Correlated fluorescence microscopy and cryo-electron tomography of virus-infected or transfected mammalian cells. Nature Protocols 2016 12:1 *12*, 150–167.

Heintzmann, R., and Cremer, C.G. (1999). Laterally modulated excitation microscopy: improvement of resolution by using a diffraction grating. Proc. SPIE *3568*, 185–196.

Klar, T.A., Jakobs, S., Dyba, M., Egner, A., and Hell, S.W. (2000). Fluorescence microscopy with diffraction resolution barrier broken by stimulated emission. Proceedings of the National Academy of Sciences *97*, 8206–8210.

Koyama, T., Yamada, M., and Matsuhashi, M. (1977). Formation of regular packets of *Staphylococcus aureus* cells. Journal of Bacteriology *129*, 1518–1523.

Krull, A., Buchholz, T.O., and Jug, F. (2018). Noise2Void - Learning Denoising from Single Noisy Images. Proceedings of the IEEE Computer Society Conference on Computer Vision and Pattern Recognition *2019-June*, 2124–2132.

Kuwada, N.J., Traxler, B., and Wiggins, P.A. (2015). Genome-scale quantitative characterization of bacterial protein localization dynamics throughout the cell cycle. Molecular Microbiology *95*, 64.

Leeuwenhoek, A. van (1695). Arcana naturae detecta: Delphis Batavorum: apud Henricum a Krooneveld.

Levin, P.A., Kurtser, I.G., and Grossman, A.D. (1999). Identification and characterization of a negative regulator of FtsZ ring formation in *Bacillus subtilis*. Proceedings of the National Academy of Sciences of the United States of America *96*, 9642.

Li, X., Zhang, G., Qiao, H., Bao, F., Deng, Y., Wu, J., He, Y., Yun, J., Lin, X., Xie, H., et al. (2021). Unsupervised content-preserving transformation for optical microscopy. Light: Science & Applications 2021 10:1 *10*, 1–11.

Mandal, S., and Uhlmann, V. (2021). Splinedist: Automated cell segmentation with spline curves. Proceedings - International Symposium on Biomedical Imaging *2021-April*, 1082–1086.

Monodane, T., Matsushima, Y., Kotani, S., Monodane, T., Matsushima, Y., and Kotani, S. (1978). Process of consecutive cell divisions and separations in a regular tetrads-forming mutant of *Micrococcus lysodeikticus (luteus)*. Microbiology and Immunology *22*, 453–462.

Monteiro, J.M., Fernandes, P.B., Vaz, F., Pereira, A.R., Tavares, A.C., Ferreira, M.T., Pereira, P.M., Veiga, H., Kuru, E., Vannieuwenhze, M.S., et al. (2015). Cell shape dynamics during the staphylococcal cell cycle. Nature Communications *6*, 1–12.

Monteiro, J.M., Pereira, A.R., Reichmann, N.T., Saraiva, B.M., Fernandes, P.B., Veiga, H., Tavares, A.C., Santos, M., Ferreira, M.T., Macário, V., et al. (2018). Peptidoglycan synthesis drives an FtsZ-treadmilling-independent step of cytokinesis. Nature *554*, 528–532.

Nogales, E., Downing, K.H., Amos, L.A., and Löwe, J. (1998). Tubulin and FtsZ form a distinct family of GTPases. Nature Structural Biology 1998 5:6 *5*, 451–458.

O'Neill, J. (2014). Antimicrobial resistance: tackling a crisis for the health and wealth of nations. Wellcome Collection.

Otto, M. (2010). *Staphylococcus* colonization of the skin and antimicrobial peptides. Expert Review of Dermatology *5*, 183.

Pichoff, S., and Lutkenhaus, J. (2005). Tethering the Z ring to the membrane through a conserved membrane targeting sequence in FtsA. Molecular Microbiology *55*, 1722–1734.

Pinho, M.G., Kjos, M., and Veening, J.W. (2013). How to get (a)round: mechanisms controlling growth and division of coccoid bacteria. Nature Reviews. Microbiology *11*, 601–614.

Rayleigh, Lord (1896). On the Theory of Optical Images, with special reference to the Microscope. Philosophical Magazine *42*, 167–195.

Redmon, J., and Farhadi, A. YOLO9000: Better, Faster, Stronger.

Reichmann, N.T., Tavares, A.C., Saraiva, B.M., Jousselin, A., Reed, P., Pereira, A.R., Monteiro, J.M., Sobral, R.G., VanNieuwenhze, M.S., Fernandes, F., et al. (2019). SEDS–bPBP pairs direct lateral and septal peptidoglycan synthesis in *Staphylococcus aureus*. Nature Microbiology *4*, 1368–1377.

Rico, A.I., Krupka, M., and Vicente, M. (2013). In the beginning, *Escherichia coli* assembled the proto-ring: an initial phase of division. The Journal of Biological Chemistry *288*, 20830–20836.

Rueden, C.T., Schindelin, J., Hiner, M.C., Dezonia, B.E., Walter, A.E., Arena, E.T., and Eliceiri, K.W. (2017). ImageJ2 : ImageJ for the next generation of scientific image data. BMC Bioinformatics *18*, 1–26.

Rust, M.J., Bates, M., and Zhuang, X. (2006). Sub-diffraction-limit imaging by stochastic optical reconstruction microscopy (STORM). Nature Methods 2006 3:10 *3*, 793–796.

Schindelin, J., Arganda-Carreras, I., Frise, E., Kaynig, V., Longair, M., Pietzsch, T., Preibisch, S., Rueden, C., Saalfeld, S., Schmid, B., et al. (2012). Fiji: An open-source platform for biological-image analysis. Nature Methods *9*, 676–682.

Schmidt, U., Weigert, M., Broaddus, C., and Myers, G. (2018). Cell Detection with Star-convex Polygons. Lecture Notes in Computer Science (Including Subseries Lecture Notes in Artificial Intelligence and Lecture Notes in Bioinformatics) *11071 LNCS*, 265–273.

Spahn, C., Laine, R.F., Pereira, P.M., Gómez-de-Mariscal, E., Chamier, L. von, Conduit, M., Pinho, M.G. de, Jacquemet, G., Holden, S., Heilemann, M., et al. (2021). DeepBacs: Bacterial image analysis using open-source deep learning approaches. BioRxiv 2021.11.03.467152.

Steele, V.R., Bottomley, A.L., Garcia-Lara, J., Kasturiarachchi, J., and Foster, S.J. (2011). Multiple essential roles for EzrA in cell division of *Staphylococcus aureus*. Molecular Microbiology *80*, 542–555.

Thévenaz, P., Ruttimann, U.E., and Unser, M. (1998). A pyramid approach to subpixel registration based on intensity. IEEE Transactions on Image Processing *7*, 27–41.

Tong, S.Y.C., Davis, J.S., Eichenberger, E., Holland, T.L., and Fowler, V.G. (2015). *Staphylococcus aureus* Infections: Epidemiology, Pathophysiology, Clinical Manifestations, and Management. Clinical Microbiology Reviews *28*, 603.

Turner, R.D., Ratcliffe, E.C., Wheeler, R., Golestanian, R., Hobbs, J.K., and Foster, S.J. (2010). Peptidoglycan architecture can specify division planes in *Staphylococcus aureus*. Nature Communications *1*.

Tzagoloff, H., and Novick, R. (1977). Geometry of cell division in *Staphylococcus aureus*. Journal of Bacteriology *129*, 343–350.

Veiga, H., Jorge, A.M., and Pinho, M.G. (2011). Absence of nucleoid occlusion effector Noc impairs formation of orthogonal FtsZ rings during *Staphylococcus aureus* cell division. Molecular Microbiology *80*, 1366–1380.

Vollmer, W., Blanot, D., and de Pedro, M.A. (2008). Peptidoglycan structure and architecture. FEMS Microbiology Reviews *32*, 149–167.

Waithe, D., Brown, J.M., Reglinski, K., Diez-Sevilla, I., Roberts, D., and Eggeling, C. (2020). Object detection networks and augmented reality for cellular detection in fluorescence microscopy. The Journal of Cell Biology *219*.

Weigert, M., Schmidt, U., Boothe, T., Müller, A., Dibrov, A., Jain, A., Wilhelm, B., Schmidt, D., Broaddus, C., Culley, S., et al. (2018). Content-aware image restoration: pushing the limits of fluorescence microscopy. Nature Methods 2018 15:12 *15*, 1090–1097.

Weigert, M., Schmidt, U., Haase, R., Sugawara, K., and Myers, G. (2020). Star-convex Polyhedra for 3D Object Detection and Segmentation in Microscopy. The IEEE Winter Conference on Applications of Computer Vision (WACV).

Wichmann, J., and Hell, S.W. (1994). Breaking the diffraction resolution limit by stimulated emission: stimulated-emission-depletion fluorescence microscopy. Optics Letters, Vol. 19, Issue 11, Pp. 780-782 *19*, 780–782.

Worthington, R.J., and Melander, C. (2013). Overcoming Resistance to β-Lactam Antibiotics. The Journal of Organic Chemistry *78*, 4207.

Wu, L.J., and Errington, J. (2004). Coordination of cell division and chromosome segregation by a nucleoid occlusion protein in *Bacillus subtilis*. Cell *117*, 915–925.

Wu, L.J., and Errington, J. (2011). Nucleoid occlusion and bacterial cell division. Nature Reviews. Microbiology *10*, 8–12.

Yamada, M., Hirose, A., and Matsuhashi, M. (1975). Association of lack of cell wall teichuronic acid with formation of cell packets of *Micrococcus lysodeikticus (luteus)* mutants. Journal of Bacteriology *123*, 678.

Yang, D.C., Blair, K.M., and Salama, N.R. (2016). Staying in Shape: the Impact of Cell Shape on Bacterial Survival in Diverse Environments. Microbiology and Molecular Biology Reviews *80*, 187–203.

Young, K.D. (2006). The Selective Value of Bacterial Shape. Microbiology and Molecular Biology Reviews *70*, 660–703.

Young, K.D. (2007). Bacterial morphology: Why have different shapes? Current Opinion in Microbiology *10*, 596.

Zhou, X., Halladin, D.K., Rojas, E.R., Koslover, E.F., Lee, T.K., Huang, K.C., and Theriot, J.A. (2015). Mechanical crack propagation drives millisecond daughter cell separation in *Staphylococcus aureus*. Science *348*, 574–578.

CHAPTER II

eHooke: a tool for automated image analysis of spherical bacteria based on cell cycle progression

Saraiva, B. M., contribution:

Saraiva, B. M., performed all described experiments and data analysis, except imaging of *Staphylococcus aureus COL* in the presence and absence of PC190723 (performed by Monteiro, J.) and manual classification of cell cycle phases for the dataset to train the artificial neural network (performed together with several other members of the lab, named below).

Acknowledgements:

We thank Ambre Josselin, Ana Raquel Pereira, Andreia Duarte, Andreia Tavares, Helena Veiga, João Monteiro, Mário Ferreira, Marta Sporniak, Moritz Sorg, Nathalie Reichmann, Nils Meiresonne, Patricia Reed, Pedro Fernandes, Pedro M. Pereira, and Simon Schäper for their outstanding contribution in the manual classification of cell cycle phases. We also thank Pedro M. Pereira for the construction of strain BCBPM090.

Data contained in this chapter was published in:

Saraiva, B.M., Krippahl, L., Filipe, S.R., Henriques, R., and Pinho, M.G. (2021). eHooke: a tool for automated image analysis of spherical bacteria based on cell cycle progression. Biological Imaging 1–25

Chapter II Summary

1. Abstract

Fluorescence microscopy is a critical tool for cell biology studies on bacterial cell division and morphogenesis. As the analysis of fluorescence microscopy images evolved beyond initial qualitative studies, numerous images analysis tools were developed to extract quantitative parameters on cell morphology and organization. To understand cellular processes required for bacterial growth and division, it is particularly important to perform such analysis in the context of cell cycle progression. However, manual assignment of cell cycle stages is laborious and prone to user bias. While cell elongation can be used as a proxy for cell cycle progression in rod-shaped or ovoid bacteria, that is not the case for cocci, such as *Staphylococcus aureus*. Here we describe eHooke, an image analysis framework developed specifically for automated analysis of microscopy images of spherical bacterial cells. eHooke contains a trained artificial neural network to automatically classify the cell cycle phase of individual *S. aureus* cells. Users can then apply various functions to obtain biologically relevant information on morphological features of individual cells and cellular localization of proteins, in the context of the cell cycle.

2. Introduction

Automated analysis of microscopy images of bacterial cells has been a booming field, with several tools being developed in recent years. These include general image analysis software and associated plugins, mainly ImageJ (Rueden et al., 2017) or its "batteries-included" distribution, Fiji (Schindelin et al., 2012), but also more specific tools focused on image analysis of bacterial cells, such as Oufti (Paintdakhi et al., 2016) or MicrobeJ (Ducret et al., 2016). These approaches can be instrumental in measuring various morphology parameters of bacterial cells. Most of these parameters vary during cell cycle progression, and relevant information can be extracted from their correlation with cell cycle stages. This is particularly important for studying processes at specific cell cycle stages, such as DNA replication, assembly of the divisome, or splitting of a mother cell to originate two daughter cells. Cell length can be used as a proxy for the cell cycle stage in cells with a clear growth axis, such as rods or ovococcoid bacteria. However, this is not the case for cocci, which have a spherical shape. One example of a particularly relevant coccus is the gram-positive pathogen *Staphylococcus aureus,* a major cause of antibiotic-resistant infections and a powerful model for cell division studies (Lakhundi and Zhang, 2018; Monteiro et al., 2018). However, analysis of *S. aureus* microscopy images is hampered by the frequent presence of clumps of adjacent or overlapping cells that result from its characteristic mode of division in orthogonal planes (Saraiva et al., 2020; Tzagoloff and Novick, 1977). Furthermore, the nearly spherical shape of staphylococcal cells impairs simple analysis of the cell cycle (Monteiro et al., 2015). Therefore, a different approach is required for cell segmentation and cell cycle stage assignment of *S. aureus* cells, when compared with model organisms that are elongated, such as *Escherichia coli*, *Bacillus subtilis* or *Caulobacter crescentus*.

The cell cycle of *S. aureus* can be described as having three different phases: Phase 1, prior to initiation of division septum synthesis; Phase 2, during which the septum is synthesized; Phase 3, during which cells have a complete septum that divides the mother cell in two, prior to splitting into two daughter cells (Monteiro et al., 2015). Manual classification of the cell cycle phase of individual cells, based on membrane and DNA morphology, is possible but highly time-consuming and prone to user bias. Here we describe a deep learning strategy for automated classification of the cell cycle stage of *S. aureus* cells. Deep learning strategies have proven successful in image analysis in various biological contexts, promoting accurate, unbiased quantification of different cellular processes (Eulenberg et al., 2017; Fisch et al., 2019; Nagao et al., 2020; Shiaelis et al., 2020). The developed software, eHooke, can provide relevant information for individual cells in the context of cell cycle progression, including the identification of different cellular regions, measurement of fluorescence in specific subcellular regions, or measurement of morphological parameters such as area, perimeter, length, width, eccentricity and irregularity.

3. Results

eHooke, developed using Python version 3.6, is a multiplatform framework for the automated analysis of bacterial microscopy images. eHooke also implements a deep-learning classification network for classification of the cell cycle phase of individual cells. The software provides a user-friendly interface (Figure 1) which allows the user to visualize the results of the different steps performed in eHooke and adjust parameters on-the-go, to fine-tune image processing. Sections below describe the capabilities of the software, illustrated using specific examples of biological interest.

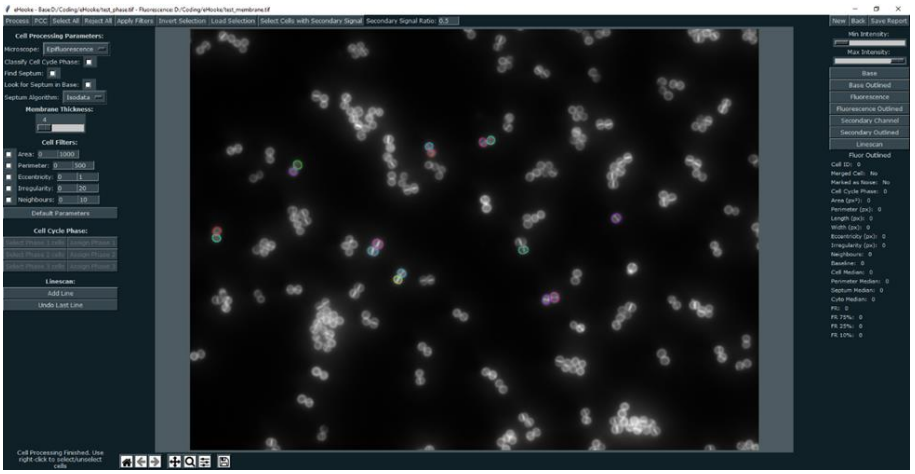

Figure 1 – Screenshot of eHooke's graphical interface.

3.1. Cell segmentation.

To segment single spherical bacterial cells in phase contrast or fluorescence microscopy images, the background is separated from the cells using an isodata thresholding algorithm (Dias Velasco, 1980). The

Euclidean distance of each foreground pixel to the background is measured to find the centre of individual cells. This segmentation step can also be performed directly on binary masks obtained with other image analysis tools. Individual cells are defined using the calculated centres and a watershed algorithm (Figure 2A, Roerdink and Meijster, 2000). eHooke will then determine the subcellular regions of *S. aureus* cells, namely the cell membrane, the division septum, and the cytoplasm (Figure 2B). Subcellular segmentation is done by expanding each cell's outline inwards, defining the membrane, and then using the isodata thresholding algorithm (Dias Velasco, 1980) to identify the brightest region inside the cell as the septum. The remaining pixels are considered the cytoplasm. At this point, the user has the option to select cells to be included in further analysis and discard inadequately segmented cells.

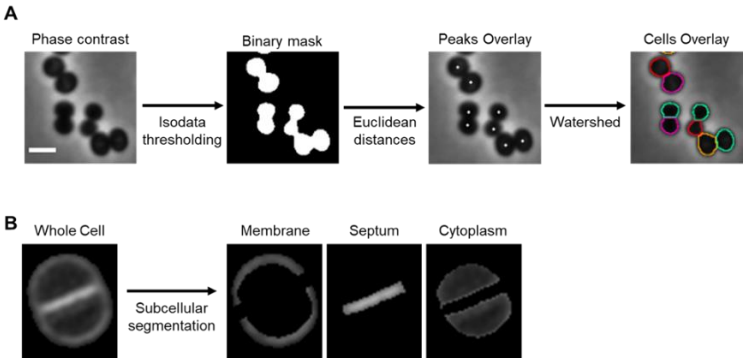

Figure 2 – Cell segmentation. A – Schematic representation of the cell segmentation workflow performed by eHooke. A base image (phase-contrast or inverted fluorescence image) is loaded, and an isodata thresholding algorithm is applied to create a binary mask. This mask separates the background from the foreground and is then used to find the centre of individual cells by measuring each pixel's Euclidean distance to the background. The pixels with the highest Euclidean distance within their surroundings are considered as peaks which, together with the binary mask, are used to define individual cells by applying a watershed algorithm. Scale bar, 1 µm. **B** – Image of an *S. aureus* cell stained with the membrane dye Nile red and imaged by structured illumination microscopy (SIM), segmented by eHooke to define three subcellular regions: membrane, septum and cytoplasm.

3.2. Automated classification of cell cycle phases.

Various cellular processes or cell phenotypes depend on the cell cycle phase of individual cells. Manually assigning a cell cycle phase to large numbers of individual cells can be significantly time-consuming, requires user training, and is subject to user bias (Figure 3).

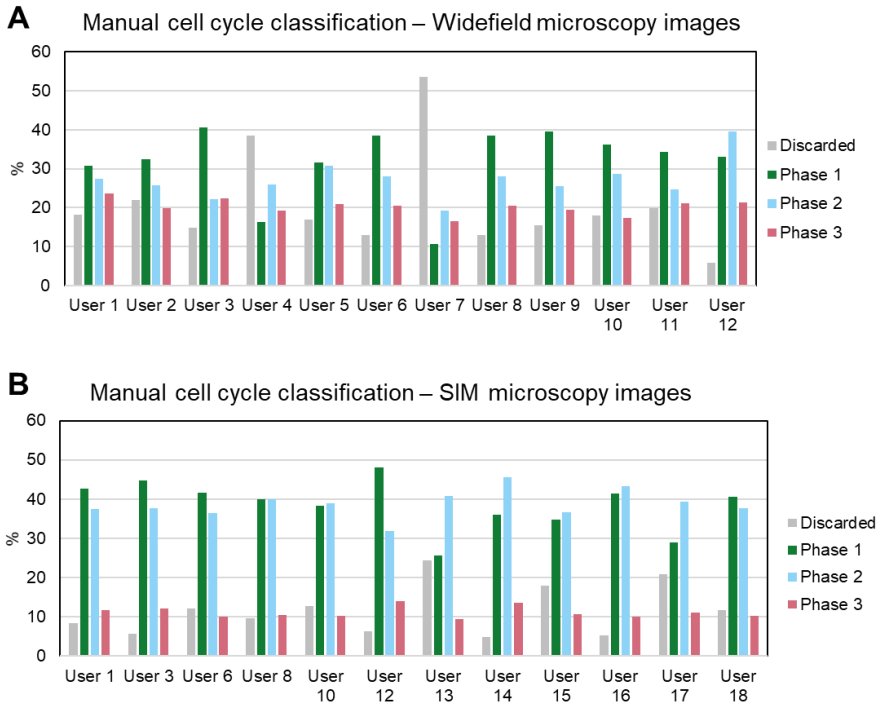

Figure 3 – Comparison of manual classification of cell cycle phases by different users. Users, members of the Pinho laboratory, were asked to classify cells according to the cell cycle stage (Phase 1-3) and discard cells thought to be incorrectly segmented by eHooke or for which they could not confidently decide on the classification. Users with the same number correspond to the same person; all users were given the same collection of cell images. **A** – User classification of 945 individual *S. aureus* JE2 cells imaged by widefield microscopy. **B** – User classification of 536 *S. aureus* JE2 cells imaged by SIM.

Here, we established an artificial neural network (ANN) to automate cell cycle classification. To do so, we trained the ANN with

manually annotated cells, imaged with either a widefield or a structured illumination microscopy (SIM) microscope. This data enabled the generation of an ANN model to adequately classify the cell cycle phase of cell images acquired in similar settings, with either a widefield or a SIM microscope. To generate the training dataset, we acquired both widefield and SIM images of *S. aureus* strain JE2 (Fey et al., 2013), labelled with membrane dye Nile red and DNA dye Hoechst 33342 (Figure 4A) and used eHooke to segment individual cells. A total of 11370 cells imaged by widefield microscopy and 9284 cells imaged by SIM were manually classified for the cell cycle phase by groups of 2 and 3 users, respectively (Figure 4B). Of those cell images, 945 widefield and 536 SIM imaged cells were classified by all 12 users, who had different levels of experience in microscopy, but were all familiar with the cell cycle of *S. aureus,* to assess user disagreement during manual classification. Figure 3 shows the considerable variation in the results obtained by different users, which was more pronounced for widefield microscopy images. Only correctly segmented cells and where the majority (at least two users of each group or at least 7 users for images classified by all users) agreed on the classification were selected for use in datasets (Figure 4B). From those, 10% of cells from each cell cycle phase were randomly selected and separated from the training dataset to be later used as a test dataset for the trained ANN. The remaining 90% of cells were adjusted by randomly discarding cells from the most frequently represented phases (Phase 1 and Phase 2), so that the training set was composed of the same number of cells for each phase, resulting in a total of 9786 cells for this dataset. The training dataset was further artificially augmented by rotating each cell image in 23 steps of 15°, producing 234864 individual cell images.

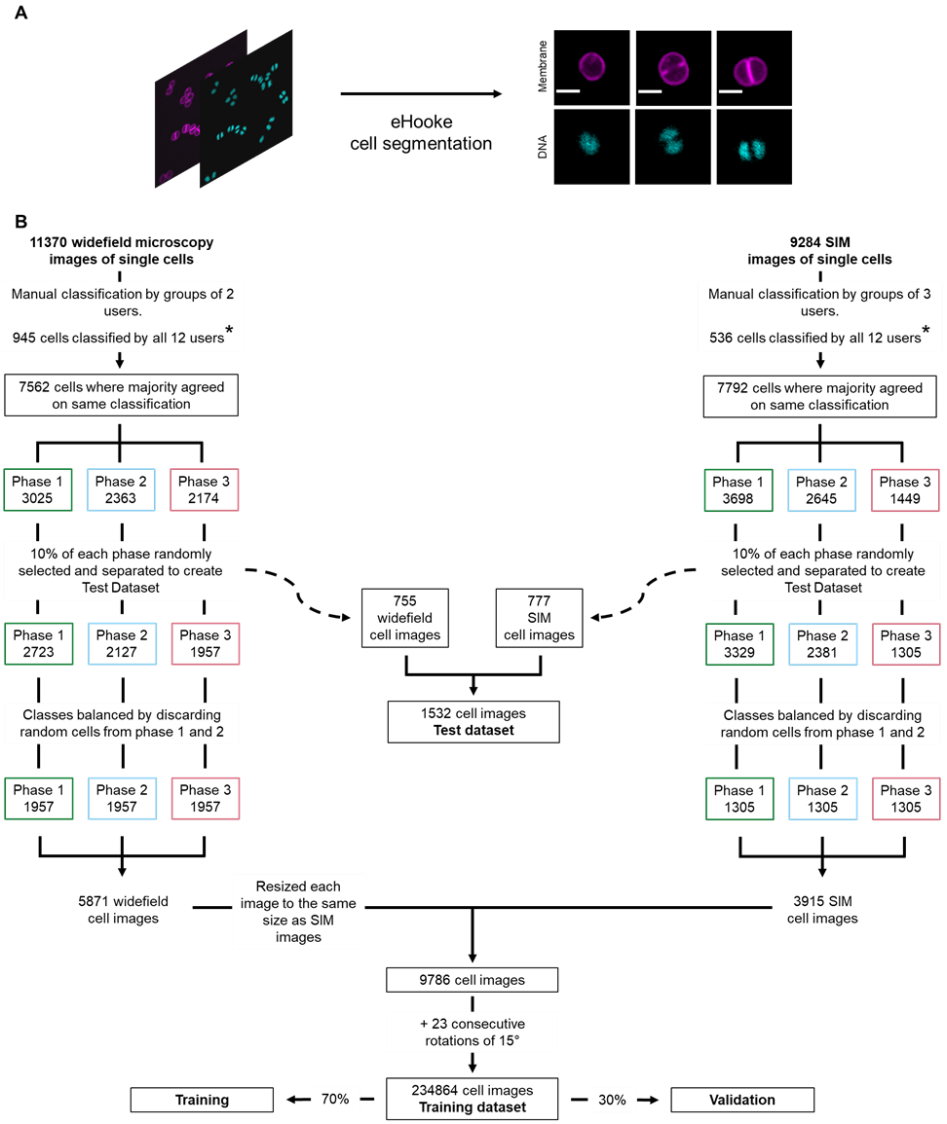

Figure 4 – Workflow for generating training and test datasets. A – *S. aureus* JE2 cells were labelled with a membrane (Nile red, in purple) and a DNA (Hoechst 33342, in cyan) dye and imaged by widefield and Structured Illumination Microscopy (SIM). eHooke was then used for cell segmentation generating 11370 and 9284 images of single cells obtained by widefield and SIM microscopy, respectively. Scale bar, 1 µm. **B** – Each cell image was manually classified according to the cell cycle phase by groups of 2 (widefield) or 3 (SIM) users; 945 widefield and 536 SIM cell images (marked *) were classified by all users and used to compare classifications between users (see Figure 3). Only cells where

the majority of users agreed on the classification were selected for use in datasets. From these selected cells, 10% of cells in each cell cycle phase were randomly selected and separated to create a test dataset. For the remaining 90% cells, the number of cells in each cell cycle phase was balanced by randomly discarding cells from Phase 1 and 2 so that each phase had the same number of cells in the training dataset. Widefield cell images were then resized to the same size as SIM images. Resized widefield images were combined with SIM images, resulting in a total of 9786 cell images. Each of these images was further rotated 23 times, 15° at a time, creating the training dataset with 234864 cell images. For training, a data split of 70% for training and 30% for validation was used.

The training dataset was then used to train a custom-made ANN, composed of seven convolution layers, each followed by a reLU activation layer with three MaxPooling layers intercalated between the first four sets of convolution and activation layers; the network also has a flatten layer, followed by a dense layer, a reLU activation layer, another dense layer and a SoftMax activation layer (see Figure 5A for a schematic representation of network architecture). For the training process, a data split of 70% for training and 30% for validation was used. During training, the ANN extracts features only from cells in the training dataset and uses those features to classify cells in both training and validation datasets. The ANN optimizes feature selection on each epoch to maximize the classification accuracy (calculated as the number of correct classifications per total number of cells) of both training and validation cells. To test whether the selected network architecture was appropriate, we performed ablation studies by training different network architectures corresponding to different depth levels (Figure 5A): depth 1 corresponds to a network architecture composed of just one convolution layer, followed by a reLU activation layer and the flatten, dense and SoftMax activation layers that are at the end of every architecture; higher depths correspond to deeper networks with

additions of MaxPooling and convolution layers (followed by reLU activation layers); depth 11 corresponds to the initial architecture, where another dense layer (followed by a reLU activation layer) is added between the flatten and the dense layer that are common to all architectures. Then, we tested the classification accuracy of each architecture, corresponding to different depth levels, using the test dataset composed of 755 and 777 individual cell images obtained by widefield and SIM microscopy, respectively, that were not used during the training step (see Figure 4). This showed that depths 7 to 10 had only minor (up to 1.6%) increases in overall accuracy (Figure 5B) and therefore we decided to keep our original network architecture which has been robustly tested by laboratory members in various experimental conditions.

The overall accuracy of the ANN for widefield and SIM images was 84% and 86%, respectively. Confusion matrices for both widefield and SIM images (Figure 6B and C) show that the trained ANN has a higher accuracy for Phase 1 and 3 cells and lower for Phase 2 cells. The trained ANN was then integrated into eHooke, which allows the user to select cells corresponding to a specific phase, as well as to manually correct any misclassification by the trained ANN.

A

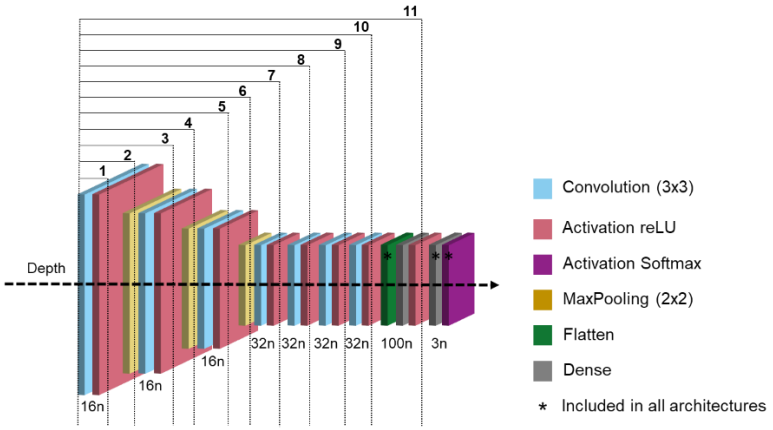

B

Depth	1	2	3	4	5	6	7	8	9	10	11
Accuracy (%)	82.0	81.6	83.7	82.5	84.0	84.7	86.4	86.5	86.4	86.0	84.9

Figure 5 – Neural network architecture and ablation studies. A – Schematic representation of the artificial neural network. The network was separated in 11 depth levels for the purpose of performing ablation studies. The final dense layer with 3 neurons and the SoftMax activation layer are kept in every architecture. Each depth level contains all the layers of the previous depths. When the dense layer from depth 11 is removed, the flatten layer is added before the final dense layer with 3 neurons for every other architecture. **B** – Classification accuracies of the test dataset (see Figure 4) obtained with artificial neural networks corresponding to each depth level.

To illustrate the usefulness of our model in a biological setting, we acquired images of *S. aureus* strain JE2 and of a mutant containing a transposon insertion in the *sle1* gene, which encodes for a peptidoglycan hydrolase (Kajimura et al., 2005) and has been previously shown to have a longer Phase 3 and, therefore, a higher fraction of Phase 3 cells in the population (Monteiro et al., 2015). The trained ANN integrated into eHooke was used to classify the cell cycle phase of each correctly segmented cell. As shown in Figure 6D, 34% of cells from JE2 parental strain were classified as being in Phase 3, while this number increased to

45% in the *sle1* mutant, in agreement with previous data (Monteiro et al., 2015). These results show that the trained ANN enables rapid and accurate cell cycle progression analysis.

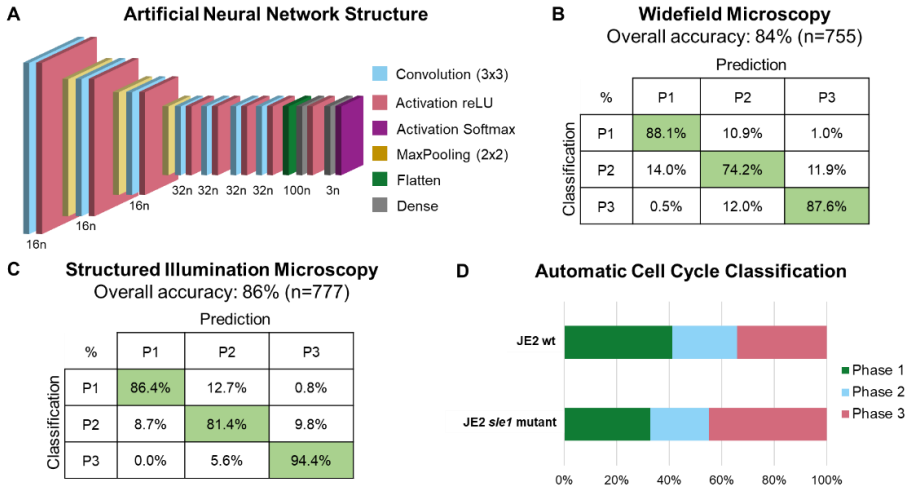

Figure 6 – Schematic representation and validation of an artificial neural network (ANN) for automated classification of cell cycle phase of *S. aureus* cells. A – Schematic representation of the structure of the used ANN; n represents the number of neurons in each layer. **B, C** – Confusion matrices for the accuracy of the trained ANN using a test dataset of (**B**) widefield images acquired using a Zeiss Axio Observer Microscope (n=755; Phase 1: 302 cells, Phase 2: 236 cells, Phase 3: 217 cells), and (**C**) SIM images acquired using a Zeiss Elyra PS.1 Microscope (n=777; Phase 1: 369 cells, Phase 2: 264 cells, Phase 3: 144 cells). **D** – Fraction of the population of parental *S. aureus* JE2 cells (n= 748) and *sle1* mutant (n= 651), previously described as being enriched in Phase 3 cells (Monteiro et al., 2015), in each phase of the cell cycle. The cell cycle phase of individual cells was assigned automatically using the trained ANN.

To determine if the trained model is generalizable to data acquired in several types of microscopes, we imaged *S. aureus* JE2 cells with labelled membrane and DNA using three different microscopes, specifically a Zeiss Axio Observer Microscope, a Zeiss Elyra PS.1

Microscope and a DeltaVision OMX SR Microscope. A fourth set of images was obtained by applying a deconvolution algorithm to the images obtained with the OMX SR microscope, using Applied Precision's softWorx software. Accuracy was equal to or above 84% for all cases except for the images where deconvolution was used, with an overall accuracy of 70% (Figure 7). This is probably caused by the fact the training dataset did not contain deconvolved images, which inherently have a different signal profile and a different signal-to-noise ratio. These results indicate that our model may be applied to images obtained with other microscopes if carefully validated.

Zeiss Axio Observer microscope
Overall accuracy: 90% (n=598)

Classification \ Prediction	%	P1	P2	P3
	P1	89.8%	10.2%	0.0%
	P2	9.1%	88.0%	2.9%
	P3	1.1%	6.3%	92.6%

Zeiss Elyra PS.1 microscope
Overall accuracy: 87% (n=613)

Classification \ Prediction	%	P1	P2	P3
	P1	96.4%	2.5%	1.1%
	P2	15.7%	77.9%	6.5%
	P3	0.0%	16.1%	83.9%

DeltaVision OMX SR microscope unprocessed
Overall accuracy: 84% (n=492)

Classification \ Prediction	%	P1	P2	P3
	P1	86.2%	11.0%	2.8%
	P2	14.6%	77.4%	7.9%
	P3	0.0%	10.0%	90.0%

DeltaVision OMX SR microscope deconvolved
Overall accuracy: 70% (n=492)

Classification \ Prediction	%	P1	P2	P3
	P1	83.9%	5.5%	10.6%
	P2	32.3%	47.6%	20.1%
	P3	0.0%	26.4%	73.6%

Figure 7 – Accuracy of automated cell cycle classification by ANN for images obtained in different microscopes. Confusion matrices of the automated cell cycle classification by the artificial neural network (ANN) for images of a culture of *S. aureus* JE2, acquired using different microscopes. Green indicates true positives.

3.3. Measurement of morphological features.

Standard morphological parameters can be automatically extracted from segmented cells, including cell area, perimeter, length, width, eccentricity and irregularity (see methods). As these parameters vary along the bacterial cell cycle, measurements obtained from all cells in an asynchronous population may hinder differences associated with specific phases of the cell cycle. eHooke facilitates morphological analysis of cells in distinct cell cycle stages after automatic cell cycle phase classification by the ANN. Users can select cells on a specific cell cycle phase for subsequent analysis. To demonstrate this application, we acquired SIM images of *S. aureus* JE2 cells stained with the membrane dye Nile red (Figure 8A) and used eHooke to automatically measure cell eccentricity, as well as to classify the cell cycle phase of individual cells. Grouping cells by cell cycle phase showed an increase in eccentricity in later stages of the cell cycle, indicating that cells become more elongated in Phase 3 (Figure 8B), in agreement with previous reports (Monteiro et al., 2015).

Analysis of cell morphology is relevant for many cell biology studies, including studying the mode of action of antimicrobial compounds. To illustrate this point, we used SIM to image *S. aureus* COL cells labelled with membrane dye Nile red, which had been previously incubated for 30 min in the absence or presence of PC190723(Figure 8C, Haydon et al., 2008). This compound targets FtsZ (the bacterial tubulin homologue), blocking cell division. Consequently, cells stop dividing, but cell wall synthesis continues, increasing the diameter of *S. aureus* cells (Haydon et al., 2008). SIM images were analysed by eHooke, individual cells were automatically identified and segmented, and morphological features, including cell area, were measured. The median area for control cells was 968 ± 161 pixels (n=173), while for cells treated with PC190723

it was 2057 ± 309 pixels (n=124), corresponding to a 2.1-fold increase, compatible with the expected inhibition of cell division (Figure 8D).

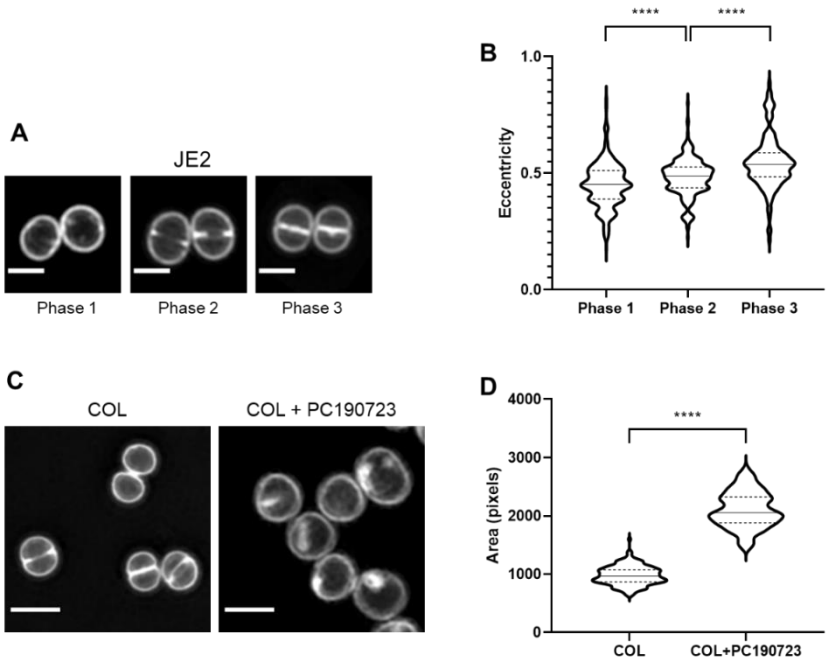

Figure 8 – Examples of single-cell morphological measurements performed by eHooke. A – *S. aureus* JE2 cells stained with membrane dye Nile red and imaged by SIM. Scale bars 1 µm. **B** – Quantification of eccentricity of JE2 cells shows an increase along the cell cycle, as previously reported (9). Phase 1 cells have a median eccentricity of 0.452 ± 0.096 (n=339), Phase 2 cells of 0.488 ± 0.081 (n=265) and Phase 3 cells of 0.538 ± 0.115 (n=150). **C** – *S. aureus* COL cells were incubated for 30 min in the absence (left) or presence (right) of the cell division inhibitor PC190723 (2.5 µg mL^{-1}), stained with membrane dye Nile red and imaged by SIM. Scale bars, 1 µm. **D** – Quantification of cell area by eHooke for both conditions shows that the presence of PC190723 leads to an increase in the median cell area, in agreement with inhibition of cell division as the mode of action for this compound (COL: n=173, COL+PC190723: n=124). **B, D** – Medians are represented by full lines and quartiles by dashed lines. Statistical analysis was performed using a two-sided Mann–Whitney U test. **** $P < 0.0001$.

3.4. Applications of eHooke in cell biology studies.

eHooke was developed to expedite various types of analyses that are useful for cell biology studies. These include:

(i) Protein localization studies**.** As an example, we analysed widefield microscopy images of *S. aureus* NCTC 8325-4 strain expressing a fluorescent derivative of Penicillin Binding Protein PBP2, an enzyme involved in the last stages of peptidoglycan synthesis and that is involved in the expression of beta-lactam resistance in *S. aureus* (Figure 9A, Scheffers and Pinho, 2005). PBP2 is a membrane-anchored protein, which is enriched at the septum of dividing cells. However, it becomes delocalized and dispersed over the cell membrane in the presence of various classes of antibiotics that inhibit peptidoglycan synthesis, such as β-lactams or glycopeptides (Pinho and Errington, 2005). PBP2 localization is a good reporter for peptidoglycan synthesis inhibition and can be assessed by calculating the ratio of the fluorescence of a PBP2 derivative at the septum versus the peripheral membrane (Pereira et al., 2007). Manual quantification of this fluorescence ratio (FR) is quite laborious. It involves tracing a line on top of each cell encompassing the background and crossing the membrane and septum, plotting the fluorescence profile, and extracting fluorescence intensity values at the septum, membrane and background. Figure 9B shows FR data obtained for cells expressing GFP-PBP2 in the presence or absence of the beta-lactam antibiotic oxacillin, either automatically using eHooke (considering the 25% brightest pixels of the septum, FR25) or manually using ImageJ (Rueden et al., 2017). eHooke data agrees well with manual quantification, showing the expected delocalization of PBP2 from the septal region in the presence of oxacillin, which leads to a reduction of FR.

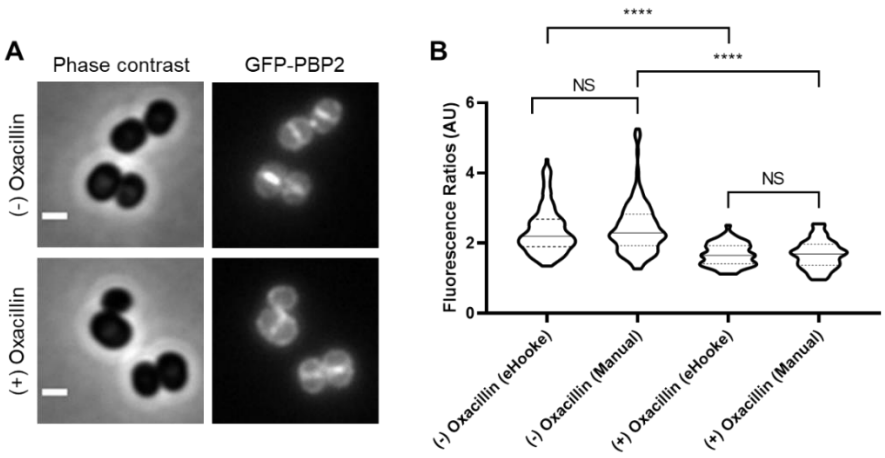

Figure 9 – Calculation of fluorescence ratios (FRs) of septal versus peripheral membrane fluorescence. A – *S. aureus* strain BCBPM090, expressing a fluorescent derivative of PBP2, was imaged by widefield microscopy. Bottom images correspond to cells incubated for 15 min with 0.5 µg mL^{-1} oxacillin prior to imaging. Scale bars 1 µm. **B** – Quantification of the fluorescence ratio (FR) value for cells as those depicted in panel B. Manual quantification ((-) Oxacillin: n=149, (+) Oxacillin: n=56) was performed using ImageJ by doing a linescan analysis, extracting the maximum values corresponding to the septum and membrane and subtracting the background value prior to calculating FR; automated analysis ((-) Oxacillin: n=168, (+) Oxacillin: n=58) was performed using eHooke, considering only the 25% brightest pixels of septum for the calculation of the FR (FR25). Both methods generated similar data showing that PBP2 delocalizes from the septum in the presence of oxacillin. Median is represented by full line and quartiles by dashed lines. Statistical analysis was performed using a two-sided Mann–Whitney U test. NS, not significant; **** $P < 0.0001$.

(ii) Analysis of mixed cell populations. Cell biology studies often require a direct comparison of fluorescence levels in two populations/mutants/strains. These comparisons are most accurate if assessed in the same microscopy image. For these pairwise comparisons, one of the samples can be labelled with a specific dye before mixing with the second sample, so that cells from each population can be easily

distinguished under the microscope. The mixed sample analysis can be made automatically in eHooke, by loading a secondary fluorescence channel image corresponding to the specific dye used to distinguish one of the samples. The primary channel corresponds to the fluorescence of the protein/dye of interest. Users can then manually select cells with a signal in the secondary channel or use an automatic selection by setting a threshold in the secondary channel. To illustrate this application, we generated mixed populations (one of which was labelled with DNA dye Hoechst 33342) of cells expressing different levels of GFP, using *S. aureus* RNpGEreporter P_{spac}-GFP (Pereira et al., 2010), a strain expressing cytoplasmic GFP under the control of the IPTG inducible P_{spac} promoter (Figure 10). eHooke was then used to measure the mean fluorescence of GFP cytoplasmic signal of both populations, distinguished automatically based on the secondary fluorescence channel (for Hoechst 33342). This simple analysis of mixed populations is helpful for various purposes, including direct comparisons of two samples, analysis of multiple samples using a fixed internal control to normalize absolute fluorescence values, or quantification of anucleate cells (lacking DNA) in a population.

(iii) Calculation of Pearson's Correlation Coefficients. Proteins that are part of the same multiprotein complex or involved in the same function often colocalize during part of, or the entire cell cycle. Analysis of protein colocalization can be made by calculating the Pearson's Correlation Coefficient (PCC, see methods) of the fluorescence signals from fluorescent derivatives of the two proteins. A PCC of 1 corresponds to a perfect correlation between the two signals, suggesting that the proteins colocalize during the entire cell cycle; a value of 0 indicates no correlation between the localization of the two proteins, while a value of -1 suggests that the two proteins are excluded from the same cellular localization.

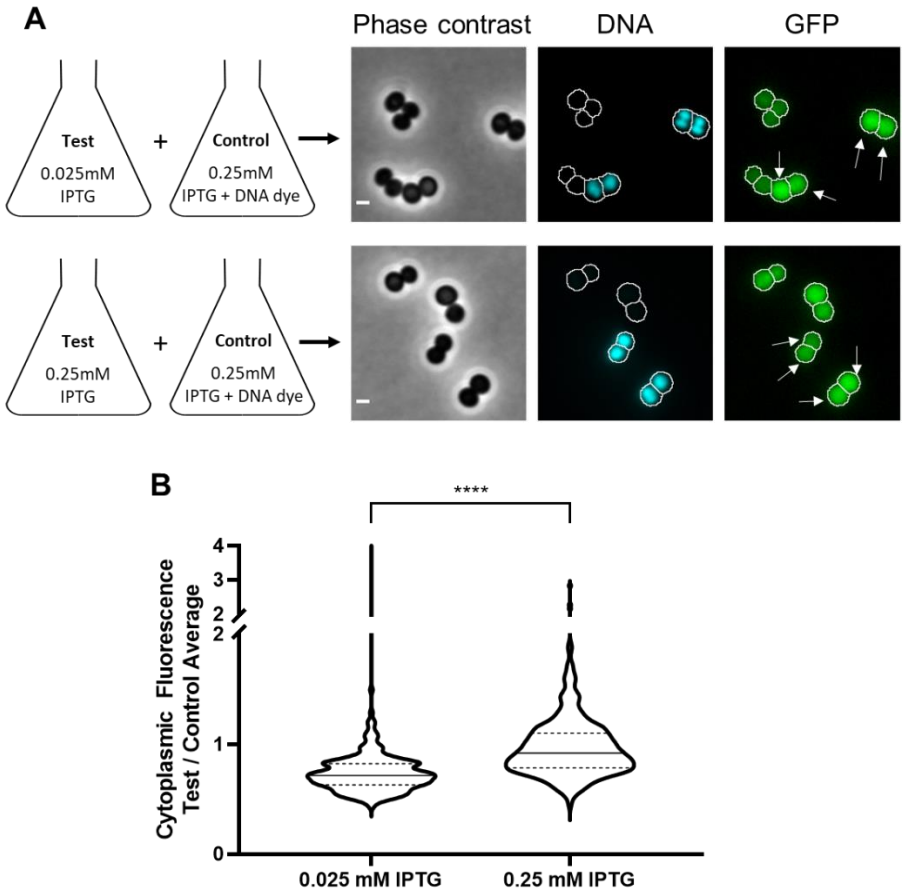

Figure 10 - Analysis of cytoplasmic fluorescence using an internal control to normalize fluorescence values. A – *S. aureus* RNpGEreporter Pspac-GFP cells were incubated with either 0.025 or 0.25 mM IPTG and mixed with control cells of the same strain incubated with 0.25 mM IPTG. These control cells were also stained with the DNA dye Hoechst 33342. White arrows in the GFP image point to control cells; white overlay in fluorescence images indicates cell outline. Scale bars 1 μm. **B** – Quantification of cytoplasmic fluorescence signal for 0.025 mM IPTG (n=214) and 0.25 mM IPTG (n=275) test cultures normalized using the control culture. As expected, when both test and control cultures were incubated with the same IPTG concentration (0.25mM), this ratio was close to 1 (0.92) and decreased (to 0.72) when test cells were incubated in the presence of lower concentration of IPTG (0.025mM) than control cells. Median is represented by full line and quartiles by dashed lines. Statistical analysis was performed using a two-sided Mann–Whitney U test. **** $P < 0.0001$.

We have previously shown that PCC measurements can be used to estimate the order of arrival of divisome proteins to the division septum as the cell cycle progresses (Monteiro et al., 2018). We have repeated that analysis using eHooke to calculate the PCC for the signal of fluorescent derivatives of two divisome proteins, FtsW and MurJ, and the early divisome protein FtsZ (Figure 11, Monteiro et al., 2018). As FtsZ is the first protein known to arrive at the divisome (Bi and Lutkenhaus, 1991), early divisome proteins correlate better with FtsZ than late divisome proteins. This type of analysis can also be helpful in other contexts, such as identifying functional pairs of proteins or screening for compounds that disrupt protein-protein interactions.

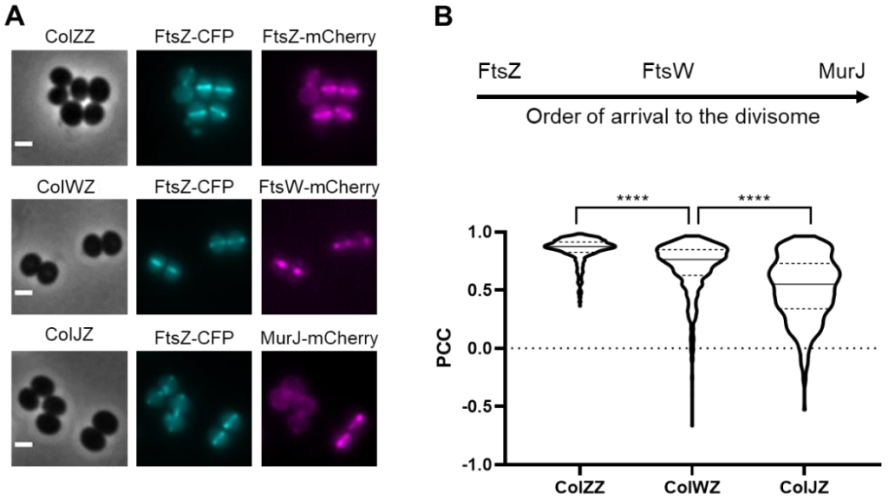

Figure 11 – Establishing the order of arrival of proteins to the divisome using Pearson's Correlation Coefficient (PCC). A – Widefield microscopy images of strains expressing two fluorescent derivatives of divisome proteins: ColZZ expressing FtsZ-CFP and FtsZ-mCherry; ColWZ expressing FtsZ-CFP and FtsW-mCherry; ColJZ expressing FtsZ-CFP and MurJ-mCherry. Scale bars 1 μm. **B** – Schematic representation of the order of arrival of FtsZ, FtsW and MurJ to the divisome (top panel), which correlates with the calculated PCC values for images of CFP and mCherry channels of the three strains mentioned in panel A: CollZZ (0.88, n=450), ColWZ (0.76 n=695) and ColJZ (0.55, n=380) (bottom panel). Median is represented by full line and quartiles by dashed lines. Statistical analysis was performed using a two-sided Mann–Whitney U test. **** $P < 0.0001$.

4. Discussion

An obvious benefit of automated image analysis is speed, allowing the analysis of large datasets that would be unmanageable if performed manually. However, an equally important advantage is reproducibility. Quantitative analysis can be straightforward, but even simple measurements, such as determining the length of a cell, imply subjective decisions, like defining the cell's edge. Qualitative analysis is even more prone to user bias and requires a "trained eye". We have asked 12 members of the laboratory to classify the cell cycle stage of a common set of cells imaged by widefield microscopy or SIM. Figure 3 shows the considerable variation of the results obtained by different users, demonstrating the limitations of analysing large datasets, where subsets are interpreted by different people. It also indicates that the ground truth of the examples used to train and test the classification network was subject to significant uncertainty since they came from manual annotations by different groups of users. Thus, the obtained accuracies for eHooke in cell cycle classification may be close to the theoretical maximum obtainable using these data as a reference. More importantly, this points to the need for objective and consistent procedures for classifying, measuring and comparing cell data. By automating these procedures, eHooke guarantees they are consistent over different samples, which is not possible with human intervention.

5. Materials and Methods

5.1. Widefield fluorescence microscopy.

Images were acquired with a Zeiss Axio Observer microscope equipped with a Plan-Apochromat 100x/1.4 oil Ph3 objective, a Retiga R1 CCD camera (QImaging), a white-light source HXP 120 V (Zeiss) and Metamorph 7.5 software (Molecular Devices). For image acquisition, the filters (Semrock) Brightline TXRED-4040B (Nile red), Brightline CFP-2432A (CFP), Brightline GFP-3035B (GFP) and Brightline DAPI-1160A (Hoechst 33342) were used.

5.2. Structured Illumination Microscopy (SIM).

SIM was performed using an Elyra PS.1 microscope (Zeiss) with a Plan-Apochromat 63x/1.4 oil DIC M27 objective. Images were acquired using five grid rotations, with 34 μm grating period for the 561 nm laser (100 mW) and 23 μm grating period for the 405 nm laser (50 mW). Images were captured with a Pco.edge 5.5 camera and reconstructed using ZEN software (black edition, 2012, version 8.1.0.484) based on a structured illumination algorithm, using synthetic, channel-specific optical transfer functions and noise filter settings ranging from −6 to −8.

5.3. Automated image analysis in eHooke.

Image analysis is initiated by loading a phase-contrast image and/or fluorescence image. The software then uses the phase-contrast or the fluorescence image to create a binary mask using the isodata algorithm for automatic thresholding (Dias Velasco, 1980), separating the background pixels from the pixels corresponding to the cells. This mask is then used to find the centres of each individual cell in the image by

applying an algorithm that computes the Euclidean distances transform (Virtanen et al., 2020). The software uses those centres and a watershed algorithm (van der Walt et al., 2014) to define the pixels corresponding to each cell. Measurement of each cell area is performed by counting the number of pixels corresponding to each cell. To measure eccentricity, the major and minor axis are defined as the major and minor axis of the smallest rectangle that can contain each cell. Eccentricity is then calculated using Equation 1 where a and b are the semi-major and semi-minor axes, respectively. eHooke will then define different cell regions: membrane, cytoplasm and, if needed, septum. The membrane is determined by dilating the outline of each cell towards the inside. The separation of the septum from the cytoplasm is done by using the isodata algorithm (Dias Velasco, 1980) to find the brightest pixels inside the cell, which eHooke then assigns to the septum. Pixels that are part of the interface between the membrane and the septum are removed from the analysis. To calculate the local median background, eHooke starts by defining a bounding box for each cell by taking the minimum and maximum x,y coordinates of pixels belonging to each cell and expanding the box to five pixels in each direction. The local median background is calculated from the background pixels defined in the binary mask in each bounding box while discarding the pixels closer to the cell defined by five rounds of binary dilations (van der Walt et al., 2014) on the binary mask. The median fluorescence of each region is measured, and the local median background is subtracted. When the user selects the option to find the septum of each cell, eHooke also calculates the fluorescence ratios (FR) of the fluorescence intensity at the septum versus the membrane (Pereira et al., 2007), according to Equation 2. FR will be calculated using all pixels from the septum (FR), or the 10% (FR10), 25% (FR25) or 75% (FR75) brightest septal pixels.

$$Eccentricity = \sqrt{1 - \frac{b^2}{a^2}} (1)$$

$$FR = \frac{Median(Septum) - Median(Background)}{Median(Membrane) - Median(Background)} (2)$$

5.4. Automated classification of cell cycle stages of *S. aureus*.

To acquire microscopy images of *S. aureus* cells at different cell cycle stages, *S. aureus* JE2 strain cultures were grown overnight in tryptic soy broth (TSB, Difco) and diluted 1:200 in fresh medium the following morning. Cultures were grown until OD_{600nm} = 0.8, and one millilitre was stained with membrane dye Nile red (5 µg mL^{-1}, Invitrogen) and DNA dye Hoechst 33342 (1 µg mL^{-1}, Invitrogen) for five minutes. Cultures were then centrifuged, washed with one millilitre of 1:3 (vol/vol) TSB/ phosphate buffered saline (PBS) solution, and resuspended in 20 µL of the same solution. Cells were mounted on microscope slides covered with a layer of 1.2% (w/v) agarose in PBS. Images were acquired by widefield microscopy or SIM. Widefield microscopy was performed to image Nile red and Hoechst 33342 with an exposure time of 100 ms. SIM was performed using a 561 nm laser (100mW) and a 405 nm laser (50mW) with an exposure time of 100 ms. Every image was segmented using eHooke and cropped around each cell (50x50 pixels for widefield and 100x100 pixels for SIM) for both fluorescence channels to create single-cell images. To remove background and fluorescence from neighbour cells from single-cell images, the fluorescence intensity of every pixel not corresponding to a cell was set to 0. Cells were then manually classified for the cell cycle phase by groups of users. Only cells with the same classification by the majority of users were used for the dataset. From these, 10% of cells in each phase were randomly selected and separated

to create the test dataset. Of the remaining images, cells from phase 1 and phase 2 were randomly discarded to balance the number of cells in each cell cycle phase. Widefield microscopy single-cell images were resized to the same size as the SIM single-cell images. Both widefield and SIM cell images were combined in a training dataset. The resulting dataset was used to train an Artificial Neural Network (ANN) to classify images of individual cells automatically. Ablation studies were performed by sequentially removing layers from the original ANN. Each architecture was trained with the training dataset and the corresponding classification accuracies tested using the test dataset. The proposed ANN model is composed of 22 layers: seven convolutions (each followed by a reLU activation layer), with the first four being intercalated by three MaxPooling, followed by one flatten, one dense, one activation reLU, another dense, and one SoftMax activation layers (Figure 6A). The generated model was integrated into eHooke. The model classifies the cell cycle phase in images where cells are labelled with a membrane dye, used as the main fluorescence channel of eHooke, and, if available, an image where cells are labelled with a DNA dye, which should be used as the secondary channel of eHooke. For biological validation, we acquired widefield microscopy images of *S. aureus* JE2 strain and a transposon mutant in the *sle1* gene (JE2 sle1::Tn , Fey et al., 2013) using the labelling strategy described above, which were then analysed using eHooke and the automated cell cycle classification ANN. To test the ANN with images obtained in different microscopes, widefield microscopy images of S. *aureus* JE2 cells were also acquired with a DeltaVision OMX SR microscope equipped with an Olympus 60X PlanApo N/1.42 oil objective and AcquireSRsoftWoRx (GE) for acquisition and deconvolution, using the 568 nm (100 mW) and 405 nm (100mW) lasers with an exposure time of 100 ms. The deconvolution algorithm used by the

AcquireSRsoftWoRx (GE) software is based on the Gold's multiplicative method (Gold, 1964), further developed by David Agard and John Sedat (Agard et al., 1989).

5.5. Effect of PC190723 on *S. aureus* cell size.

An overnight culture of *S. aureus* strain COL was back-diluted 1:200 into TSB and grown at 37°C. When the OD_{600nm} reached 0.4 the culture was separated into two flasks. PC190723 (gift by Merck) was added to one flask at a final concentration of 2.5 μg mL^{-1} and incubation was continued for 30 min at 37°C. One millilitre of each culture was stained with Nile red at a final concentration of 10 μg mL^{-1} for 5 minutes at room temperature. Cells were then centrifuged, washed with one millilitre of PBS, centrifuged again, resuspended in 20 μL of PBS, and mounted on microscope slides covered with a thin layer of 1.2% (w/v) agarose in PBS, before being imaged by SIM using the 561 nm laser with an exposure time of 100 ms. Measurement of single-cell area was done using eHooke.

5.6. Measurement of *S. aureus* cytoplasmic fluorescence.

A culture of *S. aureus* RNpGEreporter P_{spac}-GFP strain (Pereira et al., 2010) was grown overnight at 37°C in TSB with erythromycin (10 μg mL^{-1}). The culture was back-diluted 1:200 in TSB supplemented with isopropyl β-D-1-thiogalactopyranoside (IPTG, Apollo Scientific) at 0.025 mM (one flask) or 0.25mM (two flasks) and grown until OD_{600nm} = 0.8. To distinguish the 0.25 mM IPTG control from the experimental samples, DNA dye Hoechst 33342 was added to the control culture at a final concentration of 1 μg mL^{-1}. Incubation continued at 37°C for 5 minutes, and cells were washed with one millilitre of a solution of 1:3 (vol/vol)

TSB/PBS and resuspended in 20 µL of PBS. Samples were then prepared for widefield microscopy by mixing 5 µL of each sample with 5 µL of the control cells, vortexed, and the mix was mounted on microscope slides covered with a thin layer of 1.2% (w/v) agarose in PBS. Widefield microscopy images were acquired to image GFP and Hoechst 33342, with an exposure time of 3000 ms and 100 ms, respectively. The cytoplasmic fluorescence of each cell was measured using eHooke and divided by the average fluorescence of control cells.

5.7. Localization of PBP2.

S. aureus strain BCBPM090 (NCTC PBP2::P5GFPPBP2) was grown overnight in TSB at 37°C. This strain was obtained using plasmid pBCBPM061 (Tan et al., 2012) to generate a NCTC8325-4 derivative encoding a GFP fluorescent fusion to PBP2. Strain BCBPM090 was back-diluted 1:200 in TSB, grown until OD_{600nm} = 0.4. and split into two different flasks. Oxacillin (which causes PBP2 delocalization from the septum) was added to one of the flasks at a final concentration of 0.5 µg mL^{-1}. After 15 minutes, one millilitre of culture was washed with a 1:3 (vol/vol) TSB/PBS solution, resuspended in 20 µL of PBS and mounted on microscope slides covered with a thin layer of 1.2% (w/v) agarose in PBS. Images of cells incubated in the presence and absence of oxacillin were then acquired by widefield fluorescence microscopy using the filter for GFP with an exposure time of 3000 ms. Fluorescence ratios were measured using eHooke.

5.8. Measurement of Pearson's Correlation Coefficients (PCCs).

Overnight cultures of *S. aureus* COL strains ColZZ (grown in TSB with 50 µM of kanamycin and neomycin), ColWZ, and COLJZ (grown in TSB) were back-diluted 1:200 in TSB supplemented with IPTG (0.1mM for ColZZ and 0.5mM for ColWZ and COLJZ) and grown until OD_{600nm} = 0.6. One millilitre of each culture was centrifuged, washed with a PBS solution, resuspended in 20 µL of PBS, and mounted on microscope slides covered with a thin layer of 1.2% (w/v) agarose in PBS. Images were then acquired by widefield fluorescence microscopy. ColZZ images were acquired with an exposure time of 3000 ms for both CFP and mCherry channels, ColWZ with 4000 and 3000 ms, and ColJZ with 5000 and 2000 ms, respectively. PCC values were calculated for each cell using eHooke as shown in Equation 3, where X_i and Y_i correspond to pixel fluorescence intensity from two fluorescent channels and $\bar{X}$ and $\bar{Y}$ to the mean cell fluorescence intensity value on each channel. Only pixels corresponding to each cell are used for this calculation.

$$PCC = \frac{\sum_i (X_i-\bar{X})((Y_i-\bar{Y})}{\sqrt{\sum_i (X_i-\bar{X})^2}\sqrt{\sum_i (Y_i-\bar{Y})^2}}, \quad (3)$$

5.9. Statistical analysis.

Statistical analyses were done using GraphPad Prism 8 (GraphPad Software). Mann–Whitney U tests were used to compare differences between non-normal distributions. P values ≤ 0.05 were considered as significant for all analyses performed; asterisks indicate: **** P ≤ 0.0001.

6. Bibliography

Agard, D.A., Hiraoka, Y., Shaw, P., and Sedat, J.W. (1989). Fluorescence microscopy in three dimensions. Methods in Cell Biology *30*, 353–377.

Bi, E., and Lutkenhaus, J. (1991). FtsZ ring structure associated with division in *Escherichia coli*. Nature *354*, 161–164.

Dias Velasco, F.R. (1980). Thresholding using the ISODATA Clustering Algorithm. IEEE Transactions on Systems, Man, and Cybernetics *10*, 771–774.

Ducret, A., Quardokus, E.M., and Brun, Y. V. (2016). MicrobeJ, a tool for high throughput bacterial cell detection and quantitative analysis. Nature Microbiology *1*, 16077.

Eulenberg, P., Köhler, N., Blasi, T., Filby, A., Carpenter, A.E., Rees, P., Theis, F.J., and Wolf, F.A. (2017). Reconstructing cell cycle and disease progression using deep learning. Nature Communications *8*, 1–6.

Fey, P.D., Endres, J.L., Yajjala, K., Widhelm, T.J., Boissy, R.J., Bose, J.L., and Bayles, W. (2013). A genetic resource for rapid and comprehensive phenotype screening of nonessential *Staphylococcus aureus* genes. MBio *4*, 1–8.

Fisch, D., Yakimovich, A., Clough, B., Wright, J., Bunyan, M., Howell, M., Mercer, J., and Frickel, E. (2019). Defining host–pathogen interactions employing an artificial intelligence workflow. ELife *8*, e40560.

Gold, R. (1964). An iterative unfolding method for response matrices.

Haydon, D.J., Stokes, N.R., Ure, R., Galbraith, G., Bennett, J.M., Brown, D.R., Baker, P.J., Barynin, V. v., Rice, D.W., Sedelnikova, S.E., et al. (2008). An inhibitor of FtsZ with potent and selective anti-staphylococcal activity. Science *321*, 1673–1675.

Kajimura, J., Fujiwara, T., Yamada, S., Suzawa, Y., Nishida, T., Oyamada, Y., Hayashi, I., Yamagishi, J.I., Komatsuzawa, H., and Sugai, M. (2005). Identification and molecular characterization of an N-acetylmuramyl-L- alanine amidase Sle1 involved in cell separation of *Staphylococcus aureus*. Molecular Microbiology *58*, 1087–1101.

Lakhundi, S., and Zhang, K. (2018). Methicillin-Resistant *Staphylococcus aureus*: Molecular characterization, evolution, and epidemiology. Clinical Microbiology Reviews *31*, 1–103.

Monteiro, J.M., Fernandes, P.B., Vaz, F., Pereira, A.R., Tavares, A.C., Ferreira, M.T., Pereira, P.M., Veiga, H., Kuru, E., Vannieuwenhze, M.S., et al. (2015). Cell shape dynamics during the staphylococcal cell cycle. Nature Communications *6*, 1–12.

Monteiro, J.M., Pereira, A.R., Reichmann, N.T., Saraiva, B.M., Fernandes, P.B., Veiga, H., Tavares, A.C., Santos, M., Ferreira, M.T., Macário, V., et al. (2018). Peptidoglycan synthesis drives an FtsZ-treadmilling-independent step of cytokinesis. Nature *554*, 528–532.

Nagao, Y., Sakamoto, M., Chinen, T., Okada, Y., and Takao, D. (2020). Robust classification of cell cycle phase and biological feature extraction by image-based deep learning. Molecular Biology of the Cell *31*, 1346–1354.

Paintdakhi, A., Parry, B., Campos, M., Irnov, I., Elf, J., Surovtsev, I., and Jacobs-Wagner, C. (2016). Oufti: An integrated software package for high-accuracy, high- throughput quantitative microscopy analysis. Molecular Microbiology *99*, 767–777.

Pereira, P.M., Filipe, S.R., Tomasz, A., and Pinho, M.G. (2007). Fluorescence ratio imaging microscopy shows decreased access of vancomycin to cell wall synthetic sites in vancomycin-resistant *Staphylococcus aureus*. Antimicrobial Agents and Chemotherapy *51*, 3627–3633.

Pereira, P.M., Veiga, H., Jorge, A.M., and Pinho, M.G. (2010). Fluorescent reporters for studies of cellular localization of proteins in *Staphylococcus aureus*. Applied and Environmental Microbiology *76*, 4346–4353.

Pinho, M.G., and Errington, J. (2005). Recruitment of penicillin-binding protein PBP2 to the division site of *Staphylococcus aureus* is dependent on its transpeptidation substrates. Molecular Microbiology *55*, 799–807.

Roerdink, J.B.T.M., and Meijster, A. (2000). The Watershed transform: definitions, algorithms and parallelization strategies. Fundamenta Informaticae *41*, 187–228.

Rueden, C.T., Schindelin, J., Hiner, M.C., Dezonia, B.E., Walter, A.E., Arena, E.T., and Eliceiri, K.W. (2017). ImageJ2: ImageJ for the next generation of scientific image data. BMC Bioinformatics *18*, 1–26.

Saraiva, B.M., Sorg, M., Pereira, A.R., Ferreira, M.J., Caulat, L.C., Reichmann, N.T., and Pinho, M.G. (2020). Reassessment of the distinctive geometry of *Staphylococcus aureus* cell division. Nature Communications *11*, 1–7.

Scheffers, D.-J., and Pinho, M.G. (2005). Bacterial cell wall synthesis: New insights from localization studies. Microbiology and Molecular Biology Reviews *69*, 585–607.

Schindelin, J., Arganda-Carreras, I., Frise, E., Kaynig, V., Longair, M., Pietzsch, T., Preibisch, S., Rueden, C., Saalfeld, S., Schmid, B., et al. (2012). Fiji: An open-source platform for biological-image analysis. Nature Methods *9*, 676–682.

Shiaelis, N., Tometzki, A., Peto, L., McMahon, A., Hepp, C., Bickerton, E., Favard, C., Muriaux, D., Andersson, M., Oakley, S., et al. (2020). Virus detection and identification in minutes using single-particle imaging and deep learning. MedRxiv.

Tan, C.M., Therien, A.G., Lu, J., Lee, S.H., Caron, A., Gill, C.J., Lebeau-Jacob, C., Benton-Perdomo, L., Monteiro, J.M., Pereira, P.M., et al. (2012). Restoring methicillin-resistant *Staphylococcus aureus* susceptibility to β-lactam antibiotics. Science Translational Medicine *4*, 126ra35.

Tzagoloff, H., and Novick, R. (1977). Geometry of cell division in *Staphylococcus aureus*. Journal of Bacteriology *129*, 343–350.

Virtanen, P., Gommers, R., Oliphant, T.E., Haberland, M., Reddy, T., Cournapeau, D., Burovski, E., Peterson, P., Weckesser, W., Bright, J., et al. (2020). SciPy 1.0: fundamental algorithms for scientific computing in Python. Nature Methods *17*, 261–272.

van der Walt, S., Schönberger, J.L., Nunez-Iglesias, J., Boulogne, F., Warner, J.D., Yager, N., Gouillart, E., and Yu, T. (2014). Scikit-image: Image processing in python. PeerJ *2*, e453.

CHAPTER III

Screening of a transposon insertion mutant library of *Staphylococcus aureus* for novel cell cycle regulators

Saraiva, B. M., contribution:

Saraiva, B. M., performed all described experiments and data analysis, except growth of the Nebraska Transposon Mutant Library mutant strains for the microscopy experiments (performed by Sporniak, M.) and manual qualitative analysis of the acquired library images (performed together with several other members of the lab, named below).

Acknowledgements:

We thank Ambre Josselin, Ana Raquel Pereira, Andreia Tavares, Helena Veiga, João Monteiro, Mário Ferreira, Marta Sporniak, Moritz Sorg, Nathalie Reichmann, Patricia Reed, Pedro Fernandes, and Simon Schäper for their outstanding contribution in the manual qualitative analysis of the library images.

Chapter III Summary

1. Abstract

Cell cycle regulation is understudied in most bacteria, particularly in bacterial pathogens such as the clinically relevant *Staphylococcus aureus*. In order to identify genes involved in cell cycle regulation in *S. aureus,* we imaged 1920 mutants in non-essential gene from the Nebraska Transposon Mutant Library and performed visual inspection to identify mutants which had aberrant cell morphology or DNA segregation. In total we identified 233 out of the 1920 mutants with an altered phenotype. This analysis by visual inspection was followed by automatic analysis using eHooke to identify alterations in cell area and eccentricity. eHooke was also used to automatically quantify the frequency of each cell cycle phase to identify mutants with an overrepresentation of cells in a specific phase of the cell cycle and therefore possibly impaired in cell cycle progression.

2. Introduction

Staphylococcus aureus is an almost spherical bacteria that is often the cause of hospital acquired infections. Multi-drug resistant *S. aureus* strains are especially problematic as successful treatment is still challenging (Turner et al., 2019). A proper understanding of *S. aureus* cell cycle and morphogenesis can be key to find targets for novel treatment strategies.

Previous work in our group has characterized the cell cycle of *S. aureus* as being comprised of three different phases: Phase 1, when cells are approximately spherical and then become slightly elongated, before septum synthesis has initiated; Phase 2, when cells initiate and complete the synthesis of the division septum; Phase 3, when cells with a complete septum, undergo septum maturation, slight cell elongation and then split in two Phase 1 daughter cells (Monteiro et al., 2015). This splitting occurs in a "popping"-like event within milliseconds (Monteiro et al., 2015; Zhou et al., 2015). After splitting, the flat division septum is reshaped into a curved surface, with this reshaping generating less than one hemisphere of each daughter cell (Monteiro et al., 2015).

The mechanisms and proteins involved in the regulation of the cell cycle of bacteria are not yet fully understood. One of the key aspects for cell cycle progression is proper chromosome segregation. During cell division, cells need to duplicate and segregate the full genome. Since *S. aureus* nucleoid occupies most of the cell volume, proper segregation is required to avoid DNA bisection by the division septum, which can lead to DNA degradation and anucleate cells (Veiga et al., 2011). In *S. aureus*, the nucleoid occlusion protein Noc, is responsible for the inhibition of divisome assembly in its proximity, controlling where the septum is going to be placed (Wu and Errington, 2004). Deletion of Noc in *S. aureus* leads

to the septum closing over the nucleoid, generating DNA breaks and anucleate cells (Veiga et al., 2011). However, an *S. aureus* strain lacking Noc will still divide, even if abnormally (Veiga et al., 2011). Other key players in chromosome segregation are Spo0J and the structural maintenance of chromosomes (SMC) (Chan et al., 2020; Yu et al., 2010). In *Bacillus subtilis*, Spo0J was shown to contribute to the positioning of chromosome's origins (Lee et al., 2003). SMC requires Spo0j for its recruitment and was shown to also bind to the origins of the chromosome (Chan et al., 2020; Wang et al., 2014). Studies in *B. subtilis*, proposed that SMC constrains adjacent DNA segments, drawing replicated origins away from each other (Wang et al., 2014). Even though *S. aureus* cells lacking either Spo0J or SMC show segregation problems resulting in anucleate cells, the lack of one or both proteins is not lethal (Chan et al., 2020). The fact that the absence of either Spo0J, SMC or Noc is not lethal in *S. aureus* cells is a strong indication that *S. aureus* must have other unknown mechanisms capable of compensating for the lack of these proteins and continue cell cycle progression.

The Nebraska Transposon Mutant Library (Fey et al., 2013) consists of mutants with a *bursa aurealis* transposon insertion in virtually every non-essential gene (Figure 1). We took advantage of this powerful tool to look for mutants with phenotypes that could be related to cell cycle progression including mutants affected in cell morphology, DNA segregation, membrane, and septum synthesis, or cell cycle progression. By identifying these mutants and the respective genes inactivated by the transposon insertion, we expect to find new key players in cell cycle regulation.

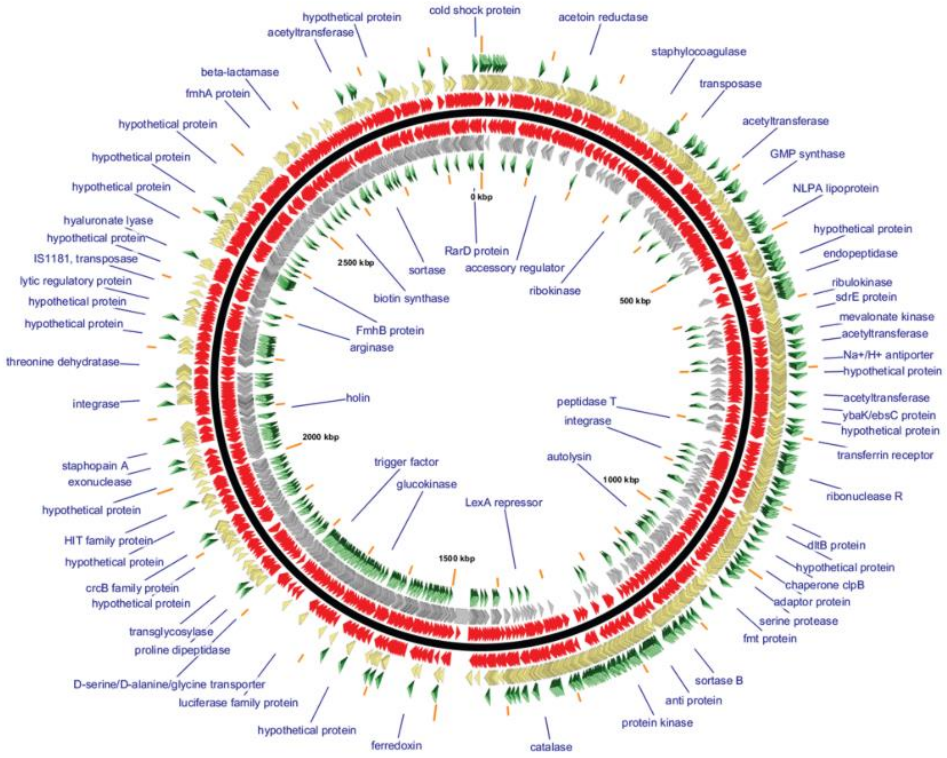

Figure 1 – Map of transposon insertion mutants in the Nebraska Transposon Mutant Library. Gview (Petkau et al., 2010) was used to generate a map of all the *bursa aurealis* transposon insertion (Tn) mutants of the Nebraska Transposon Mutant Library. Map backbone (black) separates the strand corresponding to the GenBank sequence (outside) from the reverse complement strand (inside). Annotated genes are shown as gold or grey arrowheads, Tn insertion mutants are depicted as red arrowheads and mutants that were not obtained are shown as green arrows. Reproduced from (Fey et al., 2013).

3. Results

3.1. Nebraska Transposon Mutant Library (NTML) image acquisition.

NTML consists of 1920 transposon insertion mutants in non-essential genes. Mutants were grown overnight until an OD_{600nm} between 0.5 and 0.8 was obtained and labelled with the membrane dye Nile red and the DNA dye Hoechst 33342 and imaged by widefield fluorescence microscopy in batches of 48 (Figure 2). Parental strain JE2 was imaged before and after each batch as quality control of the image acquisition process. We acquired images of at least 5 fields of view for each strain, resulting in an image library of over 10,000 images.

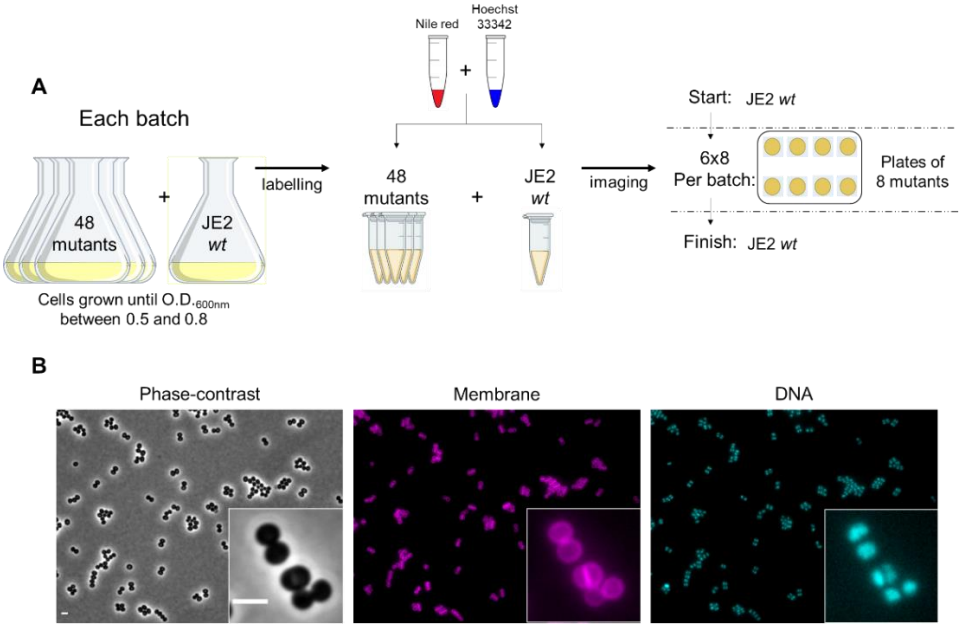

Figure 2 – NTML image acquisition. A – Batches of 48 mutants (8 per plate) were imaged alongside NTML parental strain JE2. Both the mutants and JE2 were labelled with 0.4 µL of membrane dye Nile red (10 mg mL^{-1}) and of DNA dye Hoechst 33342 (5 mg mL^{-1}). The parental strain JE2 was imaged before and after each batch for image quality control purposes. **B** – Example phase-contrast and widefield fluorescence microscopy images from JE2 cells. Bottom-right crops corresponds to zoomed in views of each image. Scale bars, 2 µm.

3.2. Qualitative analysis of NTML images.

All NTML images were assigned to one of five groups of two people to be visualized with the purpose of identifying images of mutants with any phenotype that differs from the parental strain JE2. For this task users were provided with a graphical interface (built with Python) where they could select which phenotypes were visible in each mutant microscopy images (Figure 3). At this stage, no measurements were done. Phenotype assignment was based on visual inspection only.

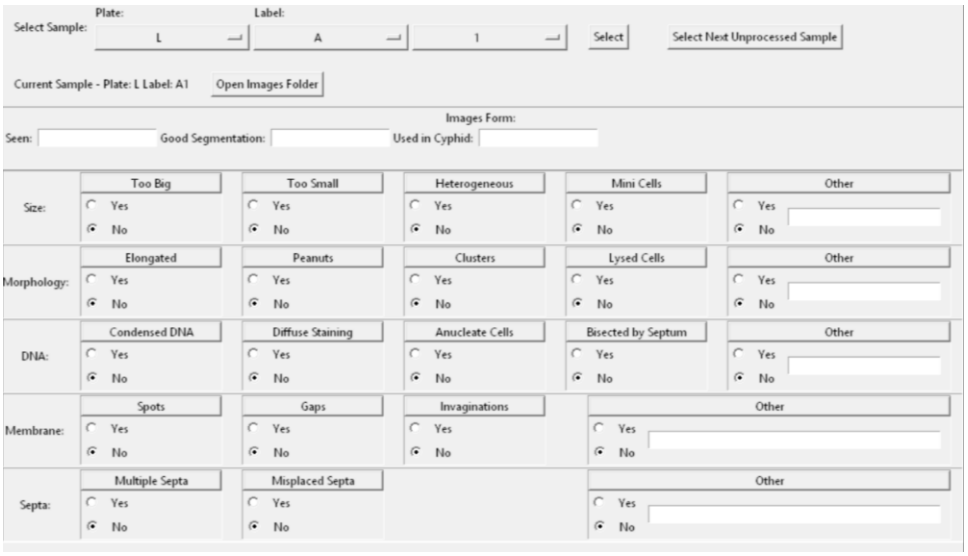

Figure 3 – Graphical interface for recording phenotypes of NTML mutants assessed by visual inspection of microscopy images.

A total of 741 mutants were identified by at least one person as showing at least one altered phenotype related to: cell morphology (altered cell size and shape, cell size heterogeneity, presence of mini cells, cell clusters or lysed cells), DNA (anucleate cells, condensed or diffuse DNA staining and nucleoid bisection by septa), membrane (membrane

spots, gaps, and invaginations) and septum (multiple and/or misplaced septa). These 741 mutants were analysed a second time by a different group of two people to confirm the phenotypes, resulting in a total of 233 mutants identified as having alterations. Of these mutants, 147 were identified as having a phenotype associated with cell morphology (Figure 4B). 47 mutants were identified as showing an altered membrane staining (Figure 4C). It should be noted that as samples were taken to the microscope in batches of 8 samples at a time, membrane labelling phenotypes may be exacerbated (or even artifacts) for cells that waited longer on the microscope slide before imaging. 28 mutants showed an alteration in septum localization/number (Figure 4D) and 54 mutants showed problems compatible with chromosome segregation defects (Figure 4E).

3.3. Automatic morphology analysis of NTML library.

Manual analysis is adequate to evaluate qualitative phenotypes, such as misplacement of the septum or cell clustering but not for quantitative parameters such as cell area or eccentricity. We used eHooke (Saraiva et al., 2021) in a Python script to automatically segment and analyse all acquired images of the NTML library. During manual qualitative analysis, users were also tasked with identifying the images that were properly segmented by eHooke. Using data only from these images, without any further curation of cell selection in terms of correct segmentation, the median area and eccentricity of every mutant were calculated by eHooke. To analyse which mutants were more affected in terms of morphology we ordered mutants according to their median cell area and eccentricity.

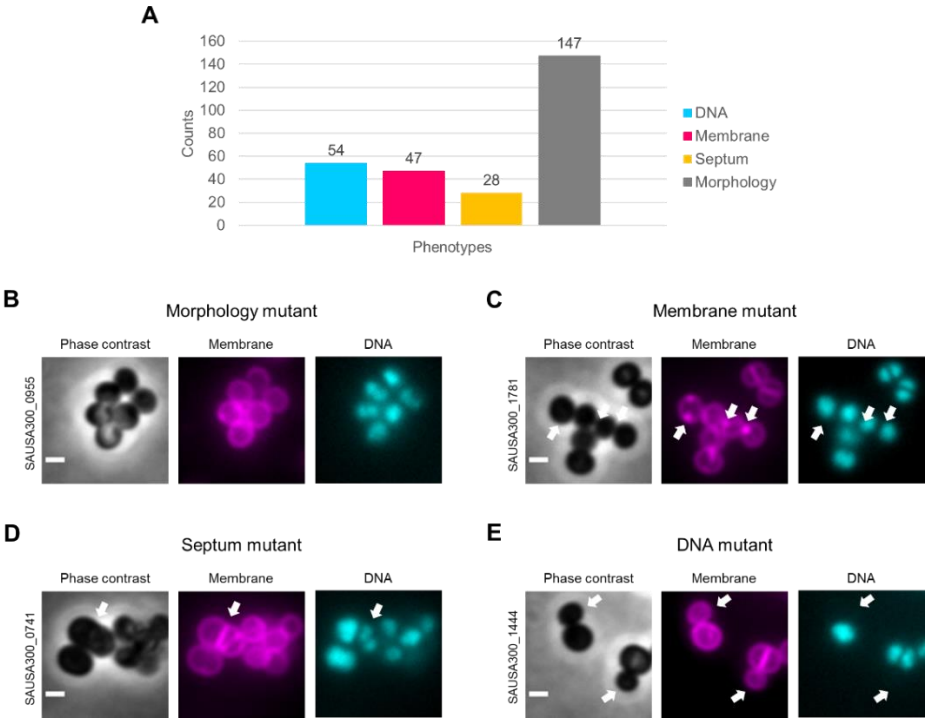

Figure 4 – Qualitative analysis of NTML mutants' images by visual inspection identified mutants with altered phenotypes. A – Distribution of identified phenotypes in NTML library. Visual inspection of microscopy images identified mutants showing a phenotype associated with: DNA (anucleate cells, condensed or diffuse DNA staining and nucleoid bisection by septa), membrane (membrane spots, gaps, and invaginations), septum (multiple and/or misplaced septa) or morphology (altered cell size and shape, cell size heterogeneity, presence of mini cells, cell clusters or lysed cells). **B** – SAUSA300_0955 (with inactivated *atl* gene) images showing cell clustering. **C** – SAUSA300_171 (transposon insertion in *hemG* gene) images showing cells with spot in membrane labelling. **D** – SAUSA300_0741 (transposon insertion in *uvrB* gene) images showing cells with multiple septa (white arrows). **E** – SAUSA300_1444 (transposon insertion in *scpB* gene) images showing anucleate cells (white arrows). Scale bars, 1 µm.

Interestingly, the fourth and fifth mutants with lowest eccentricity, were the mutants SAUSA300_1512 and SAUSA300_2040, corresponding to transposon insertions in *pbp3* and *rodA* genes, respectively. In *S.*

aureus, the proteins encoded by these genes, PBP3 and RodA, were shown to form a cognate pair and mediate the slight elongation observed in *S. aureus* cells (Reichmann et al., 2019). This indicates that the screening was sensitive enough to identify cell elongation mutants, despite this being a very mild phenotype (0.50±0.15 median cell eccentricity for JE2 wt vs 0.45±0.46 and 0.45±0.45 for the PBP3 and RodA mutants, respectively).

Besides ordering mutants by their median cell area and eccentricity, we plotted the standardized area and eccentricity after normalization to an average of 0 and standard deviation of 1 (Figure 5). The distance to the origin of the plot indicates how affected is the cell morphology of each mutant, either due to changes in cell area, eccentricity, or both. This measurement can be used to rank mutants in terms morphology alterations and to select which mutants to prioritize for further studies. Top mutants in this ranking were SAUSA300_1792, SAUSA300_2364, SAUSA300_1472, SAUSA300_0691, and SAUSA300_0903, corresponding to transposon insertion in genes encoding for a hypothetical chromosome segregation protein SMC, IgC-binding protein SBI, exodeoxyribonuclease VII large subunit XseA, DNA binding response regulator SaeR, and a hypothetical protein, respectively. These mutants will be characterized in further studies.

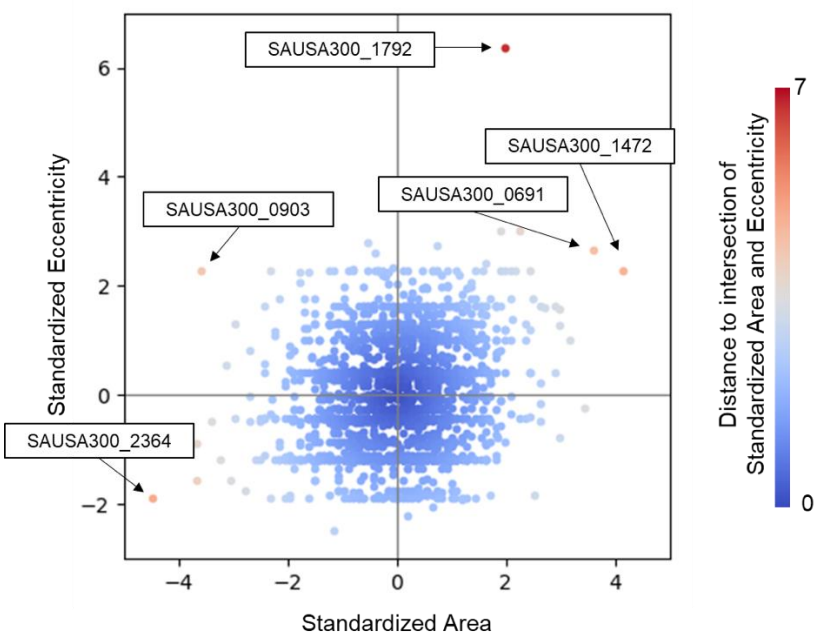

Figure 5 – Automatic quantification of cell area and eccentricity of NTML mutants. Plot of standardized (average=0, standard deviation=1) median cell area and eccentricity of each mutant. Colour map represents the distance to the origin of the plot, which corresponds to a measurement of how the morphology of each mutant is affected compared to the overall population. Labels correspond to the top5 most different mutants.

This analysis was performed blindly without any user intervention. To determine whether these results were accurate or caused by incorrect segmentation or cell selection by eHooke, we re-analysed the images of two mutants using eHooke but now manually adjusting the parameters to ensure correct cell segmentation and selecting only properly segmented cells. For this we selected SAUSA300_1472 (Figure 6A), the mutant with the highest median cell area value, with a transposon insertion in the *xseA* gene, and SAUSA300_2040 (Figure 6C), the mutant with a transposon insertion in the *rodA* gene, reported to have a decreased eccentricity when compared

to the wildtype strain JE2 (Reichmann et al., 2019). Mutant SAUSA300_1472 had a median cell area of 365.5±89 pixels (n=260), which was 1.35 times higher than the median of JE2 (327 pixels±69, n=252) (Figure 6B). The median eccentricity of mutant SAUSA300_2040 (0.44±0.14, n=219), as expected, was lower than that of JE2 (0.50±0.15, n=252) (Figure 6D). These results are a good indication than the initial, blind, eHooke analysis can be reliably used to select mutants for further studies.

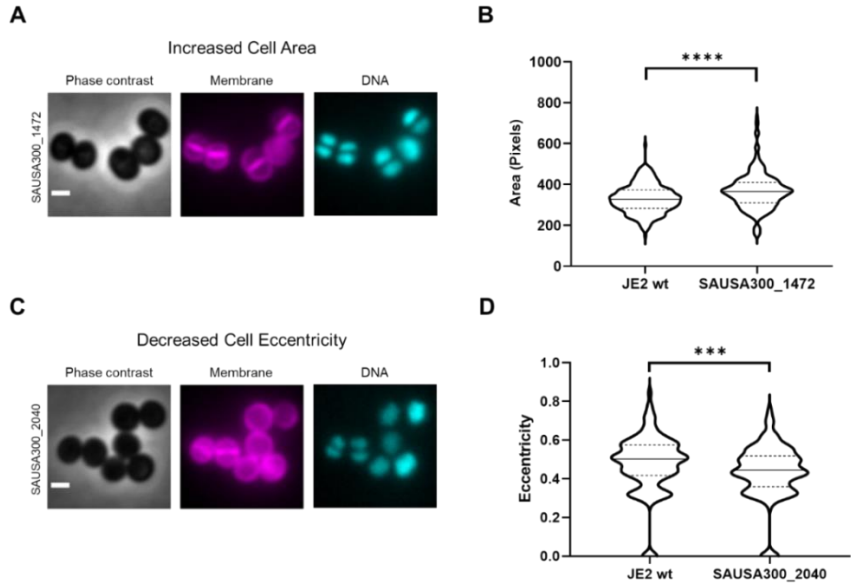

Figure 6 – Validation of the blind automatic analysis of NTML mutants by re-analysis of images with user defined parameters for cell segmentation and cell selection. A – Example images of SAUSA300_1472, which has a transposon insertion in the *xseA* gene. Scale bar, 1 µm. **B** – eHooke analysis of cell area for SAUSA300_1472 and JE2 strains shows that the transposon mutant has an increased median cell area (365.5±89 pixels, n=260 vs 327±69.22 pixels, n=252, respectively). **C** – Example images of SAUSA300_2040, with a transposon insertion in the *rodA* gene. Scale bar, 1 µm. **D** – eHooke analysis of cell eccentricity for SAUSA300_2040 and JE2 strains shows that the transposon mutant has a decreased median cell eccentricity (0.44±0.14, n=219 vs 0.50±0.15, n=252, respectively). **B, D** - Medians are represented by full line and quartiles by dashed lines. Statistical analysis was performed using a two-sided Mann–Whitney U test. *** P = 0.0007; **** P < 0.0001

3.4. Automated cell cycle analysis of NTML library mutants.

To find mutants in which the transposon was inserted in genes encoding proteins that regulate cell cycle progression, we used eHooke's artificial neural network to automatically classify the cell cycle phase of each cell in the images of NTML mutants (see chapter II). Mutants impaired in cell cycle progression, and therefore delayed in a specific phase, are expected to have an overrepresentation of cells in that cell cycle phase in non-synchronized populations, when compared to the wildtype strain JE2. To validate this approach, we looked at data for the mutant with transposon insertion in the *sle1* gene (SAUSA300_0438). Deletion of this gene was previously described as causing an increase in the frequency of cell in Phase 3 (Monteiro et al., 2015). SAUSA300_0438 corresponded to the 20th mutant (out of the 1920 mutants analysed) with highest frequency of Phase 3 cells. This indicates that automatic cell cycle classification by eHooke of all NTML mutants should identify mutants with cell cycle perturbations. However, just analysing mutants with the highest/lowest frequency of cells in each cell cycle phase might overlook mutants that have smaller differences on all cell cycle phases. Therefore, we applied a principal component analysis (PCA) to the frequency of each cell cycle phase of all NTML mutants. This PCA was done by projecting each mutant in terms of its two principal components. Then, we measured the distance of each mutant to the intersection of the principal components. Comparing the mutants using this calculated distance allowed us to detect strains with one strongly altered (increased/decreased) cell cycle phase but also strains with smaller changes across all three Phases (Figure 7). The transposon mutants that deviate the most from average were SAUSA300_1668 (OsmC/Ohr family protein), SAUSA300_0055 (alcohol dehydrogenase AdhC), SAUSA300_1792 (hypothetical chromosome segregation protein SMC),

SAUSA300_2385 (putative membrane protein KimA), and SAUSA300_0999 (spermidine/putrescine ABC transporter PotA).

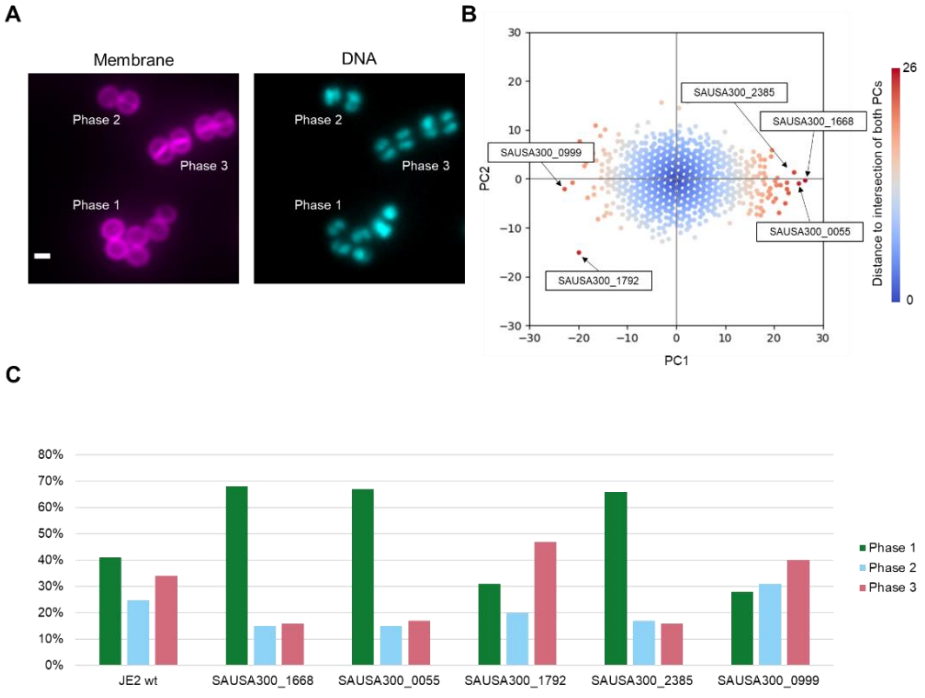

Figure 7 – Automatic quantification of frequency of each cell cycle phase of NTML mutants. A – Images of *S. aureus* strain JE2 showing cells in Phase 1-3 of the cell cycle. **B** – Projection of each mutant cell cycle phases' frequency, obtained using eHooke, in the first two principal components. Colour scale represents the distance to the intersection between both principal components and shows, for each mutant, how different the frequency of cells in each phase of the cell cycle is relative to all NTML mutants. **C** – Frequency of cells in each phase of the cell cycle for JE2 and 5 mutants that deviate most from the overall population, according to the PCA analysis. eHooke's automatic cell cycle classification was used to count the number of cells on each phase of the cell cycle.

4. Discussion

The Nebraska Transposon Mutant Library is a powerful tool containing mutants with a transposon insertion in virtually all non-essential genes of *S. aureus* strain JE2. Visual qualitative inspection of widefield fluorescence microscopy images of NTML mutant library allowed the identification of mutants with strong phenotypes. For example, images of mutant SAUSA300_0955, with a transposon insertion in the *atl* gene that encodes a major autolysin involved in separation of daughter cells (Oshida et al., 1995; Sugai et al., 1995), showed cell clusters, which is in accordance with the phenotype described in the literature (Biswas et al., 2006). Another example is SAUSA300_0741 which was identified as showing DNA associated (condensed DNA and diffuse staining). This mutant has the transposon insertion in the gene *uvrB*. The protein encoded by this gene has been described as playing an important role in the detection of DNA damage in *E. coli* (Verhoeven et al., 2002). A transposon insertion in *uvrB* may impair DNA repair, which is likely the cause of the found phenotype. It is intriguing that this mutant was also identified as showing cells with multiple septa (Figure 4D). One of the mutants found to contain anucleate cells was SAUSA300_1444 (Figure 4E), with the transposon insertion in the *scpB* gene. This gene encodes for the ScpB protein, whose role in *S. aureus* has not been previously described. However, in *Bacillus subtilis,* ScpB and its complex counterpart, ScpA, are proposed to help stabilize the engagement of head domains of the Structural Maintenance of Chromosomes (SMC) protein, which may affect its ATPase activity (Knust and Graumann, 2020). This regulation of the SMC ATPase activity is proposed to play a role in the dynamic interactions between SMC proteins and DNA. As such, it is expected that interfering with the expression of ScpB can cause chromosome segregation defects.

Further analysis of the library was performed using eHooke to measure morphological parameters of cells and comparing mutants with *S. aureus* parental strain JE2. The mutant SAUSA300_1472, a *xseA* mutant, was found to have the highest median area, 1.35x largest than the median area of JE2 (Figure 6B). This gene encodes for an exonuclease that degrades single-stranded DNA (Liu et al., 2021) that is part of Exonuclease VII complex, which was proposed in *Escherichia coli* to protect the chromosome by repairing damaged DNA (Huang et al., 2021; Jung et al., 2015). As such the observed phenotype could be caused by the lack of this predicted DNA repair mechanism. It should be noted that this mutant was also identified as having anucleate cells and cells with condensed DNA, which is more in line with what we would expect for its predicted function. Strain SAUSA300_2040, a *rodA* mutant, had one of the lowest eccentricities among the library mutants. The corresponding protein, RodA, is a member of the shape, elongation, division, and sporulation (SEDS) protein family. In rod-shaped and ovococci bacteria this protein is part of the elongasome, the protein complex responsible for cell elongation (Pinho et al., 2013). However, *S. aureus* only undergoes a slight elongation keeping a near spherical shape (Monteiro et al., 2015) but still possess RodA. This protein was shown to have transglycosylase activity (Emami et al., 2017) and in *S. aureus* it forms a cognate pair with PBP3 that is responsible for the synthesis of sidewall peptidoglycan (Reichmann et al., 2019). This sidewall synthesis of peptidoglycan is responsible for the slight elongation of *S. aureus* and its perturbation results in cells with lower eccentricity (Reichmann et al., 2019). The fact that this mutant was identified as affected in elongation by the initial blind eHooke analysis, is a strong indication of the power of this analysis.

eHooke contains an artificial neural network (described in chapter II) that was developed with the purpose of automatically classifying the cell cycle phase of cells in a microscopy image. The use of eHooke for this task instead of a manual analysis, tremendously reduces the time required, as eHooke takes approximately one hour to classify the ~10,000 images obtained from the library as opposed to the approximately 30 minutes per image that a manual analysis would take. Doing this classification in an automated manner also removes the user bias associated with manual analysis, as shown in the previous chapter (see Figure 3 from Chapter II).

This work led to the identification of several mutants impaired in cell cycle progression and therefore constitutes the basis for further studies that will investigate the exact role played by each gene. In the follow up studies, strains where the respective genes are deleted should be constructed, to ensure that the identified phenotypes are caused by the transposon inactivation of the specific gene and not caused by polar effects or by other mutations eventually present in the genome. Study of these strains should result in the discovery of new mechanisms for cell cycle regulation.

5. Materials and Methods

5.1. Nebraska Transposon Mutant Library (NTML) image acquisition.

Batches of 48 mutants of the NTML (Fey et al., 2013) were imaged per day, with JE2 (Fey et al., 2013) imaged before and after the first and last group of 8 mutants, respectively. Each strain was grown overnight at 37ºC in TSB supplemented with erythromycin, at a final concentration of 25 μg mL^{-1}, with the exception of JE2 which was grown without antibiotic. Then, each overnight was back-diluted 1:200 in TSB and grown until OD_{600nm}=0.8. From each sample, 300 μL of culture were incubated with 0.4 μL of both Nile red (10 mg mL^{-1}) and Hoechst 33342 (5 mg mL^{-1}) for 5 minutes at 37ºC with shaking. Samples were then pelleted and resuspended in 10 μL of a solution of 1:3 (vol/vol) TSB/ phosphate buffered saline (PBS). One microliter of each sample was mounted on top of a layer of layer of 1.2% (w/v) agarose in 1:3 (vol/vol) TSB/PBS placed on a Bio-Rad Mini-PROTEAN Short Plate (eight samples per plate), with a coverslip placed on top of each sample. At least 5 images per mutant were acquired with a Zeiss Axio Observer microscope equipped with a Plan-Apochromat 100x/1.4 oil Ph3 objective, a Retiga R1 CCD camera (QImaging), a white-light source HXP 120 V (Zeiss) and Metamorph 7.5 software (Molecular Devices). The filters (Semrock) Brightline TXRED-4040B (Nile red) and Brightline DAPI-1160A (Hoechst 33342) were used for image acquisition. Phase contrast and widefield fluorescence microscopy images were acquired to image cells labelled with Nile red and Hoechst 33342, with an exposure time of 100 ms for all channels.

5.2. Qualitative analysis of NTML mutants.

Five images of each mutant strain were visualised by one of five groups of two users that were assigned to do a manual analysis of these images. Users were provided with a Python script that creates a graphical user interface where they could select the observed phenotypes (Figure 3). For this analysis, each group was asked to look for phenotypes related to membrane, septum, morphology, and DNA. All the mutants that were identified as having one of these phenotypes were then further analysed by a second group of users tasked with confirming the phenotypes. Only mutants that were identified as having the same phenotype in the first visual inspection and confirmation analysis were selected.

5.3. Automatic analysis of cell morphology and cell cycle progression.

Automatic analysis of all the mutants was accomplished using eHooke to quantify the morphological parameters: area, perimeter, axis sizes, eccentricity, and irregularity. The initial analysis was performed using eHooke as part of a script to analyse the full library and selecting only the images with a good signal and overall good segmentation (selected by the users during the manual qualitative analysis). A rank of the mutants with most altered morphology was performed by plotting the standardized median cell area and eccentricity values, normalized to have an average of 0 and standard deviation of 1, and measuring the distance to the origin of the plot. Comparison of two selected mutants with JE2 strain was done with eHooke after fine tuning cell segmentation parameters and performing a curation of the cell selection in terms of proper segmentation. Every mutant was also analysed in terms of the frequency of each cell cycle phase, using the automatic cell cycle classification included in eHooke, which uses a trained artificial neural

network model (described in the previous chapter). A principal components analysis was performed on the cell cycle classification data, using the python library scikit-learn (Pedregosa et al., 2011) separating the data for two principal components. The Euclidean distance to the intersection of both principal components was calculated as way to rank how different each mutant was from the other mutants in the library.

5.4. Statistical analysis.

Statistical analyses were done using GraphPad Prism 8 (GraphPad Software). Mann–Whitney U tests were used to compare differences between non-normal distributions. P values ≤ 0.05 were considered as significant for all analyses performed; asterisks indicate: *** $P \leq 0.001$ and **** $P \leq 0.0001$.

6. Bibliography

Biswas, R., Voggu, L., Simon, U.K., Hentschel, P., Thumm, G., and Gotz, F. (2006). Activity of the major staphylococcal autolysin Atl. FEMS Microbiol Lett *259*, 260–268.

Chan, H., Söderström, B., and Skoglund, U. (2020). Spo0J and SMC are required for normal chromosome segregation in *Staphylococcus aureus*. MicrobiologyOpen *9*.

Emami, K., Guyet, A., Kawai, Y., Devi, J., Wu, L.J., Allenby, N., Daniel, R.A., and Errington, J. (2017). RodA as the missing glycosyltransferase in *Bacillus subtilis* and antibiotic discovery for the peptidoglycan polymerase pathway. Nature Microbiology 2017 2:3 *2*, 1–9.

Fey, P.D., Endres, J.L., Yajjala, K., Widhelm, T.J., Boissy, R.J., Bose, J.L., and Bayles, W. (2013). A genetic resource for rapid and comprehensive phenotype screening of nonessential *Staphylococcus aureus* genes. MBio *4*, 1–8.

Huang, S.Y.N., Michaels, S.A., Mitchell, B.B., Majdalani, N., Broeck, A. vanden, Canela, A., Tse-Dinh, Y.C., Lamour, V., and Pommier, Y. (2021). Exonuclease VII repairs quinolone-induced damage by resolving DNA gyrase cleavage complexes. Science Advances *7*.

Jung, H., Liang, J., Jung, Y., and Lim, D. (2015). Characterization of cell death in *Escherichia coli* mediated by XseA, a large subunit of exonuclease VII. Journal of Microbiology (Seoul, Korea) *53*, 820–828.

Knust, T., and Graumann, P.L. (2020). *Bacillus subtilis* Smc condenses chromosomes in a heterologous cell system, which is down-regulated by ScpAB. BMC Research Notes *13*, 4–6.

Lee, P.S., Lin, D.C.H., Moriya, S., and Grossman, A.D. (2003). Effects of the chromosome partitioning protein Spo0J (ParB) on oriC positioning and replication initiation in *Bacillus subtilis*. Journal of Bacteriology *185*, 1326–1337.

Liu, L., Ingmer, H., and Vestergaard, M. (2021). Genome-wide identification of resveratrol intrinsic resistance determinants in *Staphylococcus aureus*. Antibiotics *10*, 1–9.

Monteiro, J.M., Fernandes, P.B., Vaz, F., Pereira, A.R., Tavares, A.C., Ferreira, M.T., Pereira, P.M., Veiga, H., Kuru, E., Vannieuwenhze, M.S., et al. (2015). Cell shape dynamics during the staphylococcal cell cycle. Nature Communications *6*, 1–12.

Oshida, T., Sugai, M., Komatsuzawa, H., Hong, Y.M., Suginaka, H., and Tomasz, A. (1995). A *Staphylococcus aureus* autolysin that has an N-acetylmuramoyl-L-alanine amidase domain and an endo-β-N-acetylglucosaminidase domain: Cloning, sequence analysis, and characterization. Proceedings of the National Academy of Sciences of the United States of America *92*, 285–289.

Pedregosa, F., Varoquaux, G., Gramfort, A., Michel, V., Thirion, B., Grisel, O., Blondel, M., Prettenhofer, P., Weiss, R., Dubourg, V., et al. (2011). Scikit-learn: Machine Learning in Python. Journal of Machine Learning Research *12*, 2825–2830.

Petkau, A., Stuart-Edwards, M., Stothard, P., and van Domselaar, G. (2010). Interactive microbial genome visualization with GView. Bioinformatics *26*, 3125–3126.

Pinho, M.G., Kjos, M., and Veening, J.W. (2013). How to get (a)round: mechanisms controlling growth and division of coccoid bacteria. Nature Reviews. Microbiology *11*, 601–614.

Reichmann, N.T., Tavares, A.C., Saraiva, B.M., Jousselin, A., Reed, P., Pereira, A.R., Monteiro, J.M., Sobral, R.G., VanNieuwenhze, M.S., Fernandes, F., et al. (2019). SEDS–bPBP pairs direct lateral and septal peptidoglycan synthesis in *Staphylococcus aureus*. Nature Microbiology *4*, 1368–1377.

Saraiva, B.M., Krippahl, L., Filipe, S.R., Henriques, R., and Pinho, M.G. (2021). eHooke: a tool for automated image analysis of spherical bacteria based on cell cycle progression. Biological Imaging 1–25.

Sugai, M., Komatsuzawa, H., Akiyama, T., Hong, Y.M., Oshida, T., Miyake, Y., Yamaguchi, T., and Suginaka, H. (1995). Identification of endo-β-N-acetylglucosaminidase and N-acetylmuramyl-L- alanine amidase as cluster-dispersing enzymes in *Staphylococcus aureus*. Journal of Bacteriology *177*, 1491–1496.

Turner, N.A., Sharma-kuinkel, B.K., Maskarinec, S.A., Eichenberger, E.M., Shah, P.P., Carugati, M., Holland, T.L., and Fowler, V.G. (2019). Methicillin-resistant *Staphylococcus aureus*: an overview of basic and clinical research. Nature Reviews Microbiology *17*, 203–218.

Veiga, H., Jorge, A.M., and Pinho, M.G. (2011). Absence of nucleoid occlusion effector Noc impairs formation of orthogonal FtsZ rings during *Staphylococcus aureus* cell division. Molecular Microbiology *80*, 1366–1380.

Verhoeven, E.E.A., Wyman, C., Moolenaar, G.F., and Goosen, N. (2002). The presence of two UvrB subunits in the UvrAB complex ensures damage detection in both DNA strands. EMBO Journal *21*, 4196–4205.

Wang, X., Tang, O.W., Riley, E.P., and Rudner, D.Z. (2014). The SMC condensin complex is required for origin segregation in *Bacillus subtilis*. Current Biology *24*, 287.

Wu, L.J., and Errington, J. (2004). Coordination of cell division and chromosome segregation by a nucleoid occlusion protein in *Bacillus subtilis*. Cell *117*, 915–925.

Yu, W., Herbert, S., Graumann, P.L., and Götz, F. (2010). Contribution of SMC (Structural Maintenance of Chromosomes) and SpoIIIE to Chromosome Segregation in Staphylococci. Journal of Bacteriology *192*, 4067.

Zhou, X., Halladin, D.K., Rojas, E.R., Koslover, E.F., Lee, T.K., Huang, K.C., and Theriot, J.A. (2015). Mechanical crack propagation drives millisecond daughter cell separation in *Staphylococcus aureus*. Science *348*, 574–578.

CHAPTER IV

Reassessment of the distinctive geometry of *Staphylococcus aureus* cell division

Saraiva, B. M., contribution:

Saraiva, B. M., developed the new software tools used in this performed and performed all data analysis. Microscopy image acquisition was performed by Ana Raquel Pereira and Moritz Sorg. Constructions of strains for this work was performed by Moritz Sorg

Acknowledgements:

We thank Sérgio R. Filipe (FCT-NOVA) and Helena Veiga (ITQB-NOVA) for helpful discussions and Ana Jorge for the construction of strain BCBAJ096.

Data contained in this chapter was published in:

Saraiva, B.M.*, Sorg, M.*, Pereira, A.R., Ferreira, M.J., Caulat, L.C., Reichmann, N.T., and Pinho, M.G. (2020). Reassessment of the distinctive geometry of *Staphylococcus aureus* cell division. Nature Communications *11*, 1–7

* equal contribution to the work.

Chapter IV Summary

1. Abstract

Staphylococcus aureus is generally thought to divide in three orthogonal planes over three consecutive division cycles. Although this mode of division was proposed over four decades ago, the molecular mechanism that ensures this geometry of division has remained elusive. Here we show, for three different strains, that *S. aureus* cells do not regularly divide in three alternating perpendicular planes as previously thought. Imaging of the divisome shows that a plane of division is always perpendicular to the previous one, avoiding bisection of the nucleoid, which segregates along an axis parallel to the closing septum. However, one out of the multiple planes perpendicular to the septum which divide the cell in two identical halves can be used in daughter cells, irrespective of its orientation in relation to the penultimate division plane. Therefore, division in three orthogonal planes is not the rule in *S. aureus*.

2. Introduction

Multi-drug resistant *Staphylococcus aureus* is a major cause of hospital acquired infections, as well as infections in the community setting that are becoming increasingly difficult to treat (Turner et al., 2019). Besides its clinical relevance, *S. aureus* is also a good model to study cell growth and division of spherical cocci. Bacterial species with the suffix 'cocci' comprise species with near spherical cells, such as *S. aureus*, as well as the so-called ovococci such as *Streptococcus pneumoniae* or *Enterococcus faecalis*, which have an ovoid shape caused by peptidoglycan synthesis at the lateral wall, near the division site, that results in cell elongation (Pinho et al., 2013). We have recently shown that *S. aureus* cells are not perfectly spherical, as they undergo slight elongation mediated by the action of the penicillin binding protein PBP3, a peptidoglycan transpeptidase, and the SEDS (Shape, Elongation, Division and Sporulation) protein RodA proposed to be a peptidoglycan synthase with glycosyltransferase activity (Emami et al., 2017; Meeske et al., 2016; Monteiro et al., 2015; Reichmann et al., 2019).

While both rod-shaped bacteria and ovococci divide in successive parallel planes, perpendicular to the long axis of the cell, a distinctive characteristic of *S. aureus* division is that it is thought to occur in three alternating orthogonal planes over three consecutive division cycles. This mode of division was proposed in the 1970s on the basis of light microscopy images of individual *S. aureus* cells embedded in soft agar undergoing three consecutive divisions (Tzagoloff and Novick, 1977) or scanning electron microscopy images of cubic packages of *S. aureus* cells grown in conditions that impair cell separation (Koyama et al., 1977). Division in three orthogonal planes requires that cells retain some form of “memory” of the two previous division planes. However, the

mechanism involved, possibly shared by other cocci with a similar mode of division such as *Micrococcus luteus* (shown to form cubic packets of cells when mutants impaired in cell separation were observed by scanning electron microscopy (Monodane et al., 1978; Yamada et al., 1975)), has remained elusive. Two models have been proposed for *S. aureus* division in three orthogonal planes, both based on the presence of perpendicular "scars" of the previous divisions, present at the cell surface (Turner et al., 2010; Yamada et al., 1996). Turner and colleagues have shown that a large belt of peptidoglycan is formed at the division site which, after cell division, remains as orthogonal ribs that encode the location of previous divisions (Figure 1A, Turner et al., 2010). These structures could be used as epigenetic information to determine the orthogonality of the division planes over generations (Turner et al., 2010). We have proposed that the junction between orthogonal ribs could be used as a geometric cue for the orientation of the axis of chromosome segregation (Figure 1B, Veiga et al., 2011). *S. aureus* encodes the nucleoid occlusion protein Noc which preferentially binds to the origin proximal half of the chromosome and inhibits assembly of FtsZ, the first protein known to localize at the future division site (Veiga et al., 2011; Wu and Errington, 2004, 2011). As a consequence, progression of chromosome segregation releases midcell from Noc inhibition, allowing the FtsZ ring to be assembled at that position and therefore defining the plane of division (Wu and Errington, 2004, 2011). Importantly, both models assume that scars of the two previous divisions divide the cell in quadrants. However, we have recently shown that upon cell division, the septum of a staphylococcal cell does not generate one hemisphere of each daughter cell, but only approximately one third (Monteiro et al., 2015). Therefore, the scar of a previous division is not placed at midcell, but off-centre (Figure 1C, Monteiro et al., 2015). This asymmetry makes it less

likely that the peptidoglycan rib structures can be used as geometric cues to determine orthogonal division planes. We therefore questioned if *S. aureus* does indeed divide according to this geometry. Using super resolution fluorescence microscopy, we showed that although a plane of division is always perpendicular to the previous one, it is not necessarily perpendicular to the penultimate division plane. Consequently, most *S. aureus* cells do not divide in three alternating orthogonal planes.

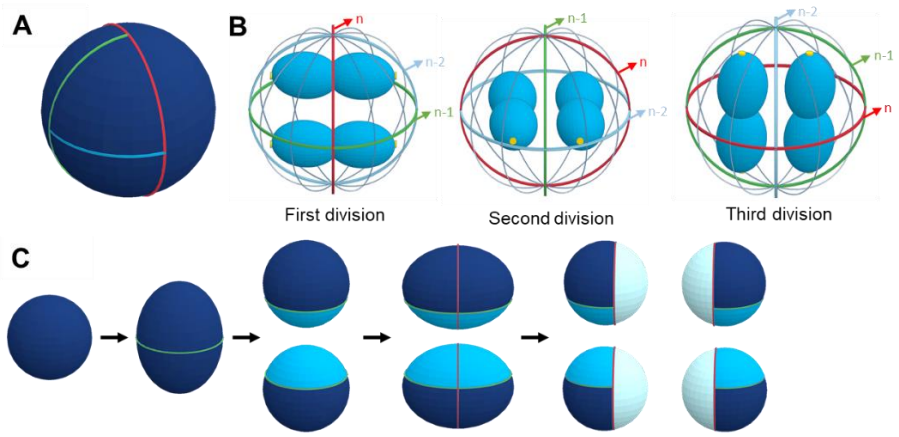

Figure 1. Specific peptidoglycan structures at the cell surface could provide epigenetic information to determine future division sites in *S. aureus*. A – Schematic representation of the cell wall surface of *S. aureus* showing scars of previous division planes that result from the formation of large belts of peptidoglycan at the division site, before septum formation. The right hemisphere corresponds to new peptidoglycan, originating from the septum of the mother cell, and therefore contains no scars. The left hemisphere contains scars from the last three rounds of division indicated by red (most recent), green and blue lines, all perpendicular to each other. These scars could encode the required epigenetic information to divide accurately in three alternating perpendicular planes (Turner et al., 2010). **B** – Illustration of *S. aureus* cell showing the orientation of the current division plane (n, red), the previous one (n-1, green) and that from two divisions ago (n-2, blue). Chromosomes are shown in blue with origins of replication shown as small yellow disks. This model assumes that chromosomes segregate towards the junction of the two previous division planes (cross between blue and green circles). This releases only one

possible division plane (red) that does not bisect the nucleoid. With each division, each scar ages by one generation, resulting in division in three alternating orthogonal planes (Veiga et al., 2011). **C** – Depiction of two consecutive divisions in orthogonal planes. Newly divided cells are approximately spherical but become slightly elongated during cell cycle progression. After the first cell division, the surface cell wall composition of each daughter cell consists of approximately two thirds of old peptidoglycan (dark blue) and approximately one third of newly synthesized peptidoglycan. As the septum does not originate one complete hemisphere of each daughter cell, the peptidoglycan scars are not placed in the middle of the cell but are off centre (Monteiro et al., 2015).

3. Results

3.1. *S. aureus* does not necessarily divide in three orthogonal planes

To follow the planes of division of cells of the methicillin-resistant *S. aureus* (MRSA) strain COL, we labelled the membrane with Nile Red and the cell wall with a fluorescent derivative of wheat germ agglutinin (WGA-488), a lectin that binds N-acetylglucosamine residues present in the peptidoglycan and in teichoic acids of the *S. aureus* cell wall. After labelling, the excess of non-bound WGA-488 was removed by washing the cells with fresh medium, but Nile Red was maintained in the medium. Cells were placed on an agarose pad containing growth medium and imaged at 20 min intervals (Figure 2 and 3). While Nile Red diffuses over the cell membrane, the WGA-488 labelling is retained at its initial position on the cell wall and therefore can be used as a marker to follow the orientation of division planes. This is important because splitting of the septum of *S. aureus* cells occurs via an extremely fast (less than 2 milliseconds) "popping" event, often leading to two daughter cells connected by a hinge (Figure 3A, Monteiro et al., 2015; Zhou et al., 2015). This movement, and the consequent change in relative position of the

daughter cells, decreases the accuracy in determining the orientation of division planes if no marker besides the membrane dye is used.

Time-lapse images of dividing COL cells showed that each division plane is perpendicular to the previous one (Figure 2A, B). However, we could observe various examples of cells that did not divide in three alternating orthogonal planes over three division cycles (see arrows in Figure 2C and Figure 3B), suggesting that this mode of division is not always respected. Using this approach, we could quantify the number of cells dividing in two consecutive perpendicular planes (Figure 2B), but we could not reliably determine the fraction of cells that did not divide in three consecutive alternating perpendicular planes, as daughter cells that result from divisions in a plane parallel to the microscopy slide become superimposed, often hindering imaging.

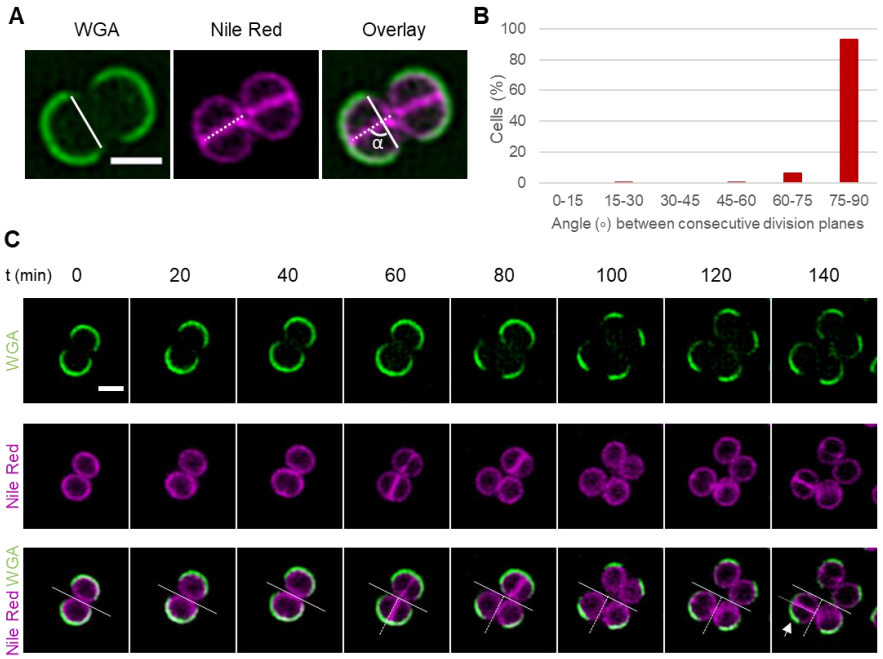

Figure 2. *S. aureus* cells divide in two, but not necessarily in three, alternating orthogonal planes. *S. aureus* strain COL cells were initially stained with cell wall dye WGA-488 (green) and membrane dye Nile Red (magenta). Excess of non-bound WGA-488 was removed by washing and Nile Red was added again before cells were placed on a medium-containing agarose pad and imaged every 20 min by structured illumination microscopy. **A** – The border of the WGA-488 labelled region provides information on the orientation of the previous division plane (solid line) while the Nile Red labelled septum indicates the orientation of the current division plane (dotted line). The angle (α) between the full and dotted lines corresponds to the angle between the two consecutive planes of division. **B** – Histogram of the angle α formed between two consecutive planes of division shows that these planes are orthogonal (with an average deviation from 90° of 6.7°, n=183 cells examined over three biological replicates). Source data are provided as a Source Data file. **C** – First, second and third division planes are indicated by solid, dashed and dotted lines, respectively, showing that in the cell indicated by the arrow the third division plane is parallel, not perpendicular, to the first plane of division. Scale bars, 1 μm. A full field of view can be accessed in https://figshare.com/s/4808495d92a138aae36c

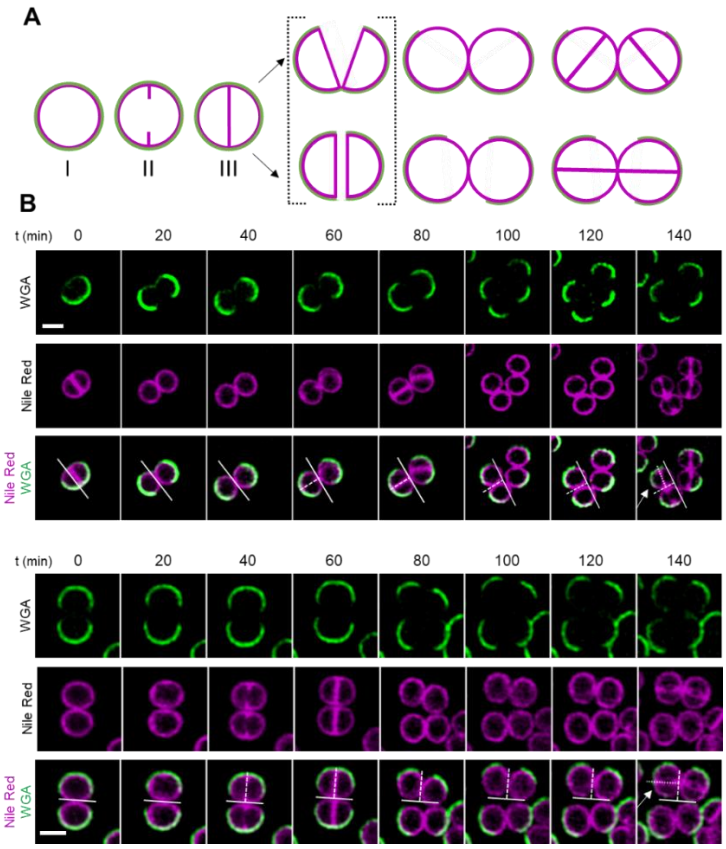

Figure 3. Examples of *S. aureus* cells that did not divide in three alternating orthogonal planes over three division cycles. **A** – Schematic representation of *S. aureus* cell cycle depicting cells initially stained with cell wall dye WGA-488 (green) and membrane dye Nile Red (magenta) where excess of non-bound WGA-488 is removed by washing and Nile Red is added again before cells are placed on medium-containing agarose pad and allowed to grow. The stage of the cell cycle can be assessed based on the membrane dye labelling, showing cells with no septum (I), a forming septum (II) or a complete septum (III), which is rapidly split in a process that takes only a few milliseconds (cells in dashed brackets). This process can lead to changes in the orientation of the daughter cells, leading to two daughter cells connected by a hinge (top). In other cases, cells retain their relative orientation after splitting (bottom). **B** – *S. aureus* strain COL cells were labelled as described above and imaged every 20 min by structured illumination microscopy. First, second and third division planes are indicated by solid, dashed and dotted lines, respectively, showing that in cells indicated by arrows the third division plane is parallel, not perpendicular, to the first plane of division. Scale bars, 1 μm.

3.2. Sister cells do not always divide on the same division plane

As an alternative approach to follow the orientation of division planes in *S. aureus*, we reasoned that if cells always divided in three alternating orthogonal planes, two sister cells would, inevitably, divide along the same plane, given that they share the same "history" or "scar" orientation from previous divisions (Figure 4A, left panel). It follows that if two sister cells do not divide along the same division plane, then the distinctive geometry of division in three alternating orthogonal planes is not being adhered to in at least one of them (Figure 4A, right panel). We observed that in *S. aureus*, the early divisome is assembled in a D-shape in each of the two sister cells prior to septum splitting (Figure 4B). Sister cells at this specific stage (still attached) allow a window of opportunity to image the exact orientation of the future division planes, before any eventual change in orientation occurs during cell splitting. The angle between two D-shaped divisomes in sister cells is therefore informative about the orthogonality of sequential division planes.

We labelled the early divisome of *S. aureus* using available fluorescent derivatives of three early cell division proteins, the tubulin homologue FtsZ (Monteiro et al., 2018), the FtsZ regulator EzrA, a protein which directly interacts with FtsZ and is therefore often used as a proxy for its localization (Monteiro et al., 2018), and the DNA translocase FtsK (Veiga and Pinho, 2017). While the FtsZ fusion to GFP is not functional (Monteiro et al., 2018) and was therefore expressed from a cadmium inducible promoter in a background that contains the native FtsZ protein, EzrA-GFP (Reichmann et al., 2019) and GFP-FtsK (Veiga and Pinho, 2017) fusions are functional, and were expressed from the native locus, under the control of the native promoter, in the absence of the corresponding native gene.

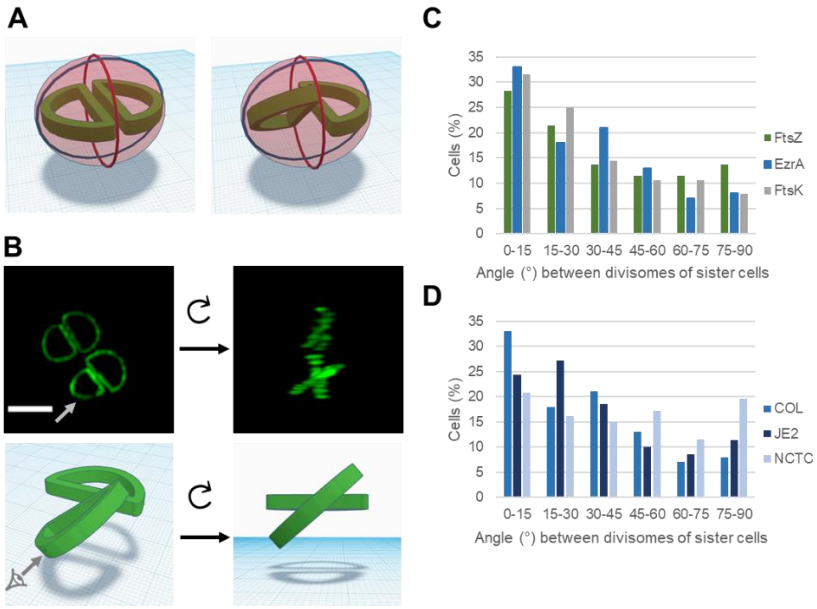

Figure 4. Sister cells can divide in different planes. A – Model of cells undergoing division showing the previous (blue line), current (red line) and next (green D shape) division planes. Left image: if cells divide in three consecutive orthogonal planes then sister cells will inevitably divide in same plane, perpendicular to the previous and current division planes. Right image: if the future division plane is not the same in both sister cells, then the orthogonal geometry of division is not respected in at least one of the sister cells, as exemplified by the left hemisphere where the next division will occur in a plane that is perpendicular to the current plane in red of division but not to the previous one in blue. **B** – Top panel: top view of 3D rendering of a Z-stack of images of COL EzrA-sGFP cells. Left panel shows the top view and right panel shows the view after rotating the 3D reconstruction to a perspective where division planes become perpendicular to the viewing plane, appearing as a cross. Scale bar, 1 µm. Bottom panel: model of the divisome of two sister cells, illustrating their orientation before and after rotation. Grey arrow indicates point of view after rotation. A full field of view can be accessed in https://figshare.com/s/907e54dd2d24e7c5dd05. **C, D** – Histograms of angles formed by divisomes of sister cells showing that two sister cells very often select different planes of division. Measurements were performed using Z-stacks of images obtained from (**C**) COL strains expressing FtsZ$^{55\text{-}56}$GFP (n=131), EzrA-GFP (n=100) and GFP-FtsK (n=76) and (**D**) COL (n=100), JE2 (n=70) and NCTC (n=87) strains expressing EzrA-GFP and analysed using automated software (see methods). Two to four biological replicates were imaged for each strain. Quantifications were done from a single experiment for each strain.

3D reconstructions of Z-stack images from dividing COL cells expressing one of these three fluorescent fusions clearly showed that the orientation of the divisome is often not the same in two attached sister cells (Figure 4B). To manually measure the angle between the two division planes of sister cells, we rotated each 3D reconstruction to an orientation where division planes become perpendicular to the viewing plane, appearing as a cross (Figure 4B, Figure 5). The smallest angle formed by the two divisomes was then measured for each pair of sister cells, where those dividing in the same plane would have an angle close to 0° (Figure 5A). These measurements indicated that for the majority of sister cells (>85%, n=77), the two divisomes are not aligned (defined as divisomes at an angle larger than 15°). However, while for some cells angle measurement was straightforward (see examples in Figure 5B), for others, particularly when the angle was small, it was prone to user bias, as the orientation of the two divisomes was difficult to assess (see examples in Figure 5C). We therefore developed a script to automatically measure the angles between divisomes by generating kymographs to convert the 3D information into 2D data (see methods and Figure 6 and 7). This method enabled us to eliminate user bias, and so was used for subsequent analysis.

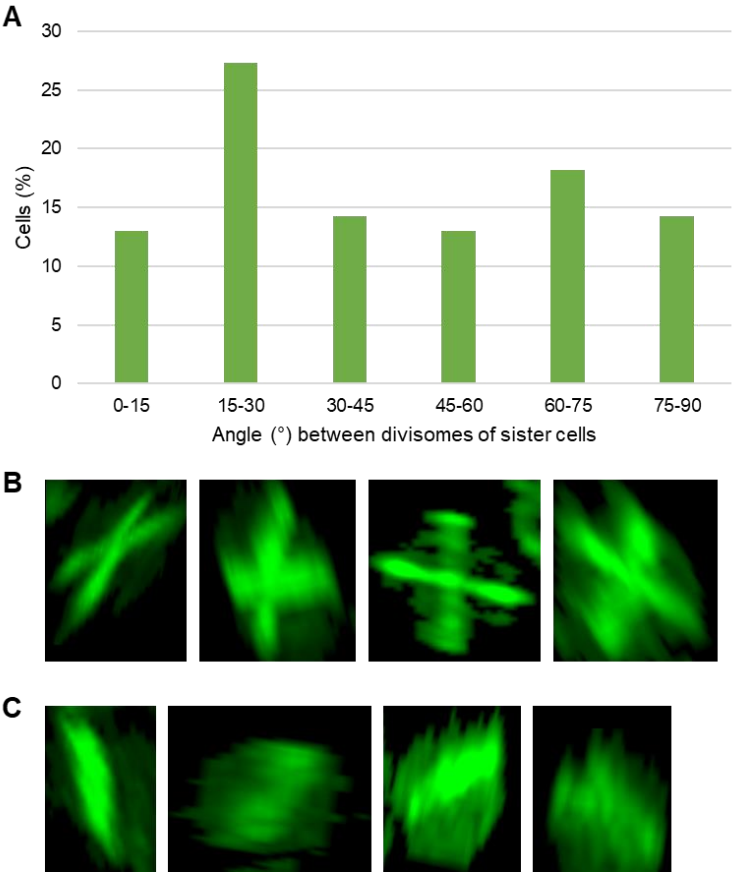

Figure 5. Manual measurement of angles between sister cells division planes shows that *S. aureus* cells do not necessarily divide in three alternating orthogonal planes. **A** – Histogram of angles formed by divisomes of sister cells showing that two sister cells very often select different planes of division. Manual measurements of angles were performed on rotated 3D renders of Z-stacks of ColFtsZ$^{55\text{-}56}$sGFP images (n=77, from one experiment). Source data are provided as a Source Data file. **B** – Examples of 3D reconstructions of Z-stacks of images of strain ColFtsZ$^{55\text{-}56}$sGFP rotated so that division planes become perpendicular to the viewing plane, used to manually measure the angle of divisomes in sister cells. **C** – Examples of rotated 3D reconstructions that were discarded for angle measurements, due to the low resolution after rotation of the 3D rendering, impairing accurate assessment of the relative position of each division plane.

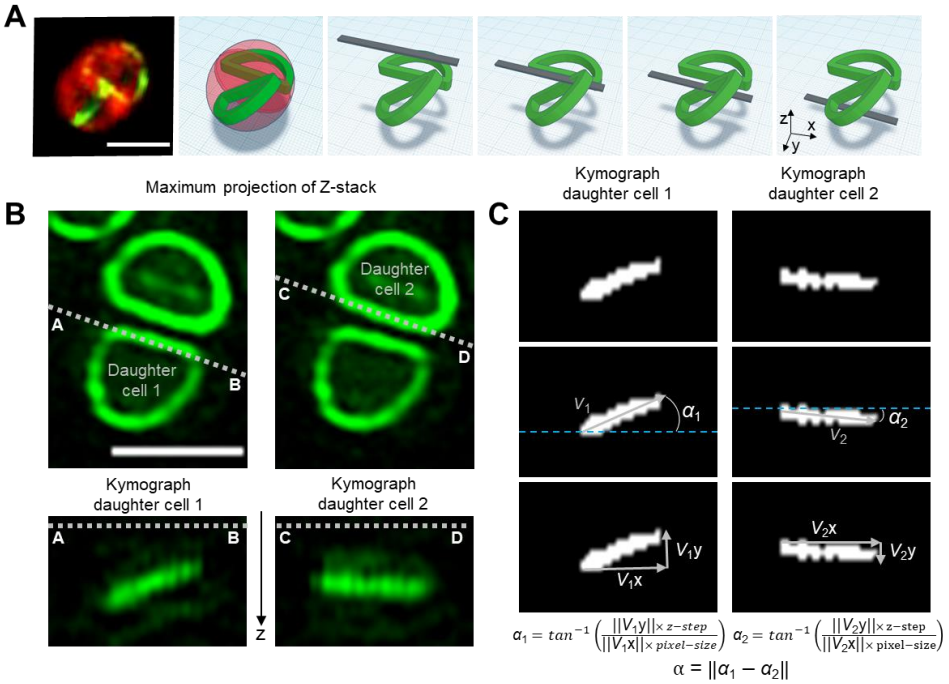

Figure 6. Strategy to measure the angle between division planes of two sister cells using Z-stacks kymographs. **A** – The left image shows a cell of strain COL *sfgfp-ftsK* labelled with membrane dye FM5-95 and imaged by SIM, where the septum has been formed and the divisome has assembled in each sister cell (scale bar 1 μm); the second image shows a model of that cell where the divisomes are seen as green D-shapes; the next four images illustrate the process used to generate the kymographs in panel b, where each line corresponds to the fluorescence signal obtained for a Z plane (grey rectangle) of a 3D reconstruction of the cells encoding a fluorescent derivative of a divisome protein (FtsZ, EzrA or FtsK). **B** – Maximum projection of a Z-stack (top) obtained by imaging a single dividing cell (containing two attached sister cells) of strain ColFtsZ$^{55\text{-}56}$sGFP and corresponding kymographs of the divisome of each sister cell (bottom). Kymographs were generated by tracing two lines (dotted) that cross/overlap the divisome of each sister cell and are parallel to its flat region. Scale bar, 1 μm. **C** – To measure the angle formed between the divisome of each sister cell, the fluorescence signal in the kymographs was first converted to a binary image (top panel, see methods); a vector indicating the orientation of the kymograph line (V_1 and V_2, for sister cell 1 and 2, respectively) was then calculated by using the coordinates of the white pixels as input for a Principal Component Analysis (PCA, Jolliffe and Cadima, 2016) and choosing the first component as the orientation vector. The angle between this vector and the microscopy imaging plane (dashed

blue line) is indicated as α_1 and α_2, for sister cell 1 and 2, respectively (middle panel). The bottom panel shows the x and y components of V_1 and V_2 used to calculate α_1 and α_2. This was done by determining the arctangent of the ratio between the norms of *V*x and *V*y. Norms of *V*x were corrected by multiplying by the camera pixel size. Norms of *V*y were corrected by multiplying by the step size between each plane of the Z-stack. The angle α between the divisome of the two daughter cells is calculated as the absolute difference between α_1 and α_2, as indicated in the equation.

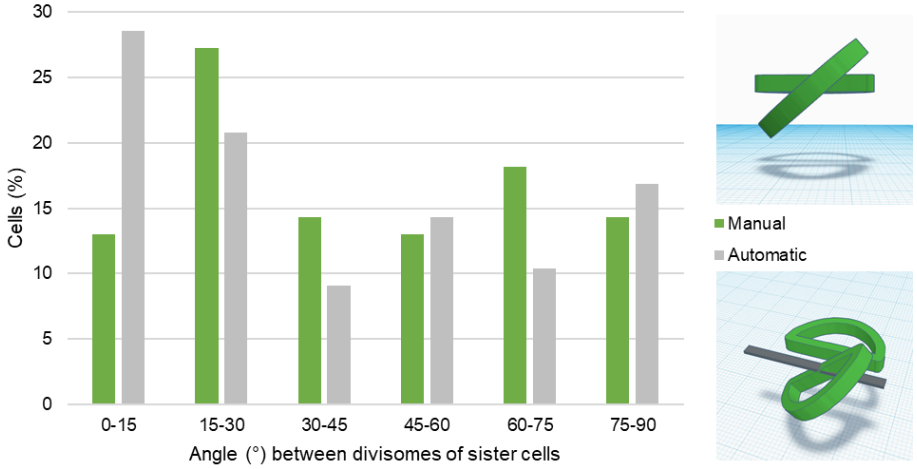

Figure 7. Manual and automatic kymographs show similar angle distribution. Histograms of angles formed by divisomes of sister cells of strain ColFtsZ$^{55\text{-}56}$sGFP measured both manually (green) and with automated software (grey), n=77 from one experiment. Both methods show that sister cells can divide in different planes.

As seen in Figure 4C, divisomes in sister cells of *S. aureus* strain COL can be placed at any angle from 0-90°. Although there was some preference for smaller angles, the majority of cells with a complete septum had the divisomes of the two future daughter cells placed at angles larger than 15° (>~70%, n=307). This observation was independent of the fluorescent fusion used to label the divisome (FtsZ$^{55\text{-}56}$GFP, EzrA-GFP or GFP-FtsK) and therefore it is unlikely to be an artefact

due to the presence of the fluorescent proteins. It is also not due to free movement of the divisome, as we showed that once this structure is assembled, its orientation is essentially maintained (Figure 8).

To determine if the mode of division observed for COL was common to other *S. aureus* strains, we determined the placement of the divisome in the community-acquired MRSA strain JE2 and in methicillin susceptible *S. aureus* (MSSA) strain NCTC8325-4, using EzrA-GFP to localize the divisome (Figure 4D). Like in strain COL, the majority of sister cells in NCTC8325-4 or JE2 strains (>75%, n=87 and n=70, respectively) had the divisomes placed at an angle larger than 15°, clearly indicating that division in three alternating orthogonal planes over consecutive generations is often not respected in all tested *S. aureus* strains.

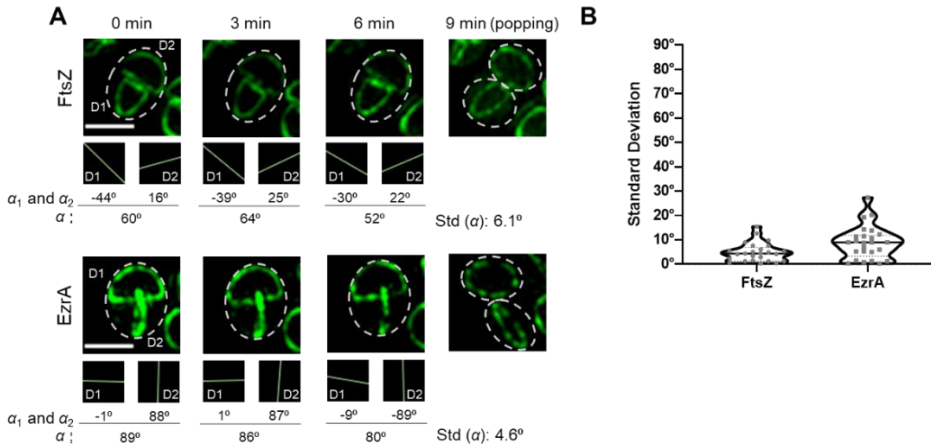

Figure 8. Assembled *S. aureus* divisomes do not freely move/rotate. **A** – Examples of timelapse images (maximum projections of Z-stacks) of strains ColFtsZ$^{55\text{-}56}$sGFP (top) and COL EzrA-sGFP(bottom) acquired every 3 minutes by SIM. Dashed lines indicate the outline of cells. In both examples shown, cells divided and "popped" between 6 and 9 min timepoints. Squares with green lines indicate orientation of the divisomes in two daughter cells (D1 and D2), determined as described in Figure 6. α_1 and α_2 correspond to the angle of the divisome of daughter cells D1 and D2 to the microscopy imaging plane. α corresponds to the angle between the divisomes of the two daughter cells D1 and D2. If a cell moves on the slide during the timelapse, the absolute values of α_1 and α_2 will vary, but α should remain constant, unless the two divisomes move relatively to each other. Scale bars, 1 µm. **B** – Violin plots where each data point corresponds to the standard deviation of the angles α obtained at different time points for one cell, for strains ColFtsZ$^{55\text{-}56}$sGFP (left, n=25 cells examined from two biological replicates) and COL EzrA-sGFP (right, n=25 cells examined from two biological replicates). Solid line indicates median and dashed lines indicate 25 and 75 percentiles.

4. Discussion

Cell division in three consecutive orthogonal planes has been considered a hallmark of *S. aureus,* ever since it was proposed, over four decades ago (Koyama et al., 1977; Tzagoloff and Novick, 1977). This model was based on scanning electron microscopy images, which do not allow analysis over consecutive division cycles, or on phase contrast microscopy images of dividing *S. aureus* cells, where the geometry of division can only be followed based on the relative position of daughter cells, which is difficult to determine with precision, mainly when cells divide in the plane of the microscope slide. This geometry of division in alternating orthogonal planes implies "memory" of the two previous division planes, and therefore it suggests that *S. aureus* cells should have a specific molecular mechanism to ensure this mode of division, which we and others have tried, without success, to identify. Using super resolution structured illumination microscopy and acquiring Z-stacks that provide 3D information of the division planes, we have now shown that such a mechanism is not required by staphylococcal cells, as they often do not divide in three consecutive alternating orthogonal planes (see video in https://youtu.be/2Bw-SKu7pbQ for an animation of three consecutive division cycles). It is important to note, however, that each division plane is always perpendicular to the previous plane, although not necessarily to the one before that. Cell division in two perpendicular planes has been proposed for other cocci. In *Neisseria gonorrhoeae* this mode of division is ensured by the Min system, a nucleoid-independent system to position the cell division plane through localized inhibition of FtsZ assembly (Rowlett and Margolin, 2015). Although the localization of gonococcal Min proteins is unknown, expression of GFP-tagged *N. gonorrhoeae* MinD in round (*rodA*-deficient) *E. coli* cells has shown that the protein oscillates in a plane parallel to the complete septum (Ramirez-Arcos et al., 2002).

This movement should generate a region with minimal MinD concentration in a plane perpendicular to the previous septum, making it the most probable division site (Ramirez-Arcos et al., 2002). A similar mechanism has been recently proposed for division of *Deinococcus radiodurans* in two perpendicular planes (Floc'h et al., 2019).

However, *S. aureus* does not have a Min system, and division in two perpendicular planes is instead dictated by the nucleoid occlusion effector Noc (Veiga et al., 2011), which preferentially binds the origin proximal region of the chromosome and prevents FtsZ polymerization over that region of the chromosome (Wu and Errington, 2011). Therefore, once the axis of chromosome segregation is established, there is only one possible plane of division that does not bisect the nucleoid (green circumference in Figure 9A).

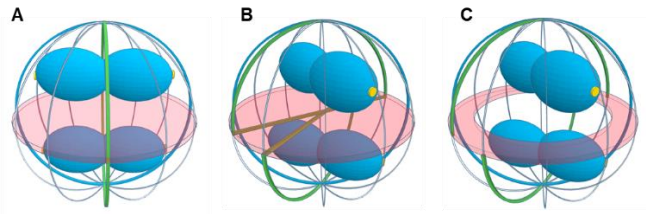

Figure 9. New model for the geometry of cell division in *S. aureus*. Scheme of dividing *S. aureus* cells showing the scar of the previous division plane (blue ring), the current division plane (red disk) and the localization of the future division plane, where the divisome assembles (green ring). Chromosomes are shown in blue with origins of replication shown as small yellow disks. **A** – The axis of chromosome segregation, which is parallel to the closing septum, establishes the division plane in *S. aureus,* as the origin proximal region is bound by the nucleoid occlusion effector Noc, which prevents FtsZ assembly. The only division plane that does not lead to bisection of the nucleoid is the plane indicated in green. **B** – Chromosome segregation towards any of the meridians (grey lines) is geometrically equivalent. Therefore, chromosomes in sister cells can segregate in different orientations, releasing different planes for division (green lines). **C** – Chromosome segregation can precede septum formation suggesting that positioning of the chromosomes, and not only of the septum, may prevent chromosome segregation towards the poles.

The role of chromosome segregation in driving division site selection has been also proposed in the ovococci *S. pneumoniae,* which interestingly lacks not only a Min system but also a nucleoid occlusion effector (van Raaphorst et al., 2017). Chromosome segregation in *S. aureus* likely occurs along an axis parallel to the closing septum, as segregation perpendicularly to the septum (towards the "poles") would be less favourable for chromosome demixing due to spatial constraints (Jun and Wright, 2010). It follows that a plane of division that does not bisect the nucleoid is necessarily perpendicular to the previous division plane (red disk in Figure 9A) and so no other mechanism is in principle required to ensure division in two perpendicular planes. However, segregation towards any of the "meridians" (grey lines in Figure 9) is geometrically equivalent, as long as the cell is circular at the division plane. We now propose that the choice of axis of segregation is essentially random, as long as it is parallel to the closing septum. As a consequence, (i) each division plane is always perpendicular to the previous one, but not necessarily to that of two divisions ago (blue circumferences in Figure 9) and (ii) sister cells can, and often do, choose different division planes. Nevertheless, it is possible that some cells have a small geometric deformation, leading to a septum that is not a perfect circle, which could favour a specific orientation of the chromosomes in both sister cells, along a slightly longer axis, explaining the preference seen towards small angles particularly in strains COL and JE2.

Interestingly, we observed that, in a fast-growing strain, chromosome segregation can start before completion of the previous closing septum (scheme in Figure 9C and Figure 10). We observed cells in which an early divisome was present (assessed by the presence of an open EzrA or FtsZ ring) but with no signs of membrane invagination at the division plane, and two separated chromosome replication origins

could already be seen in one of the future daughter cells (see cells marked with an asterisk in Figure 10). Therefore, it is possible that it is not the division septum that constrains a chromosome to one daughter cell and impairs segregation towards the "poles", but the physical presence of the other chromosome.

Finally, we show for the first time, to the best of our knowledge, that FtsZ can initially assemble as a "D" shaped structure, instead of as a ring, in live bacterial cells. Non-ring shapes of FtsZ have been previously observed in sculpted *E. coli* cells forced into unnatural shapes, including squares, hearts, stars and also "Ds" (Soderstrom et al., 2018). This implies that the curvature of the FtsZ polymers is not constant around the cell and that the shape of the FtsZ structure may be dictated by the bacterial cell shape. It will be interesting to determine in the future if the dynamics of FtsZ polymers is affected by the curvature of the Z-ring and what impact the rapid *S. aureus* popping has on the assembling divisome.

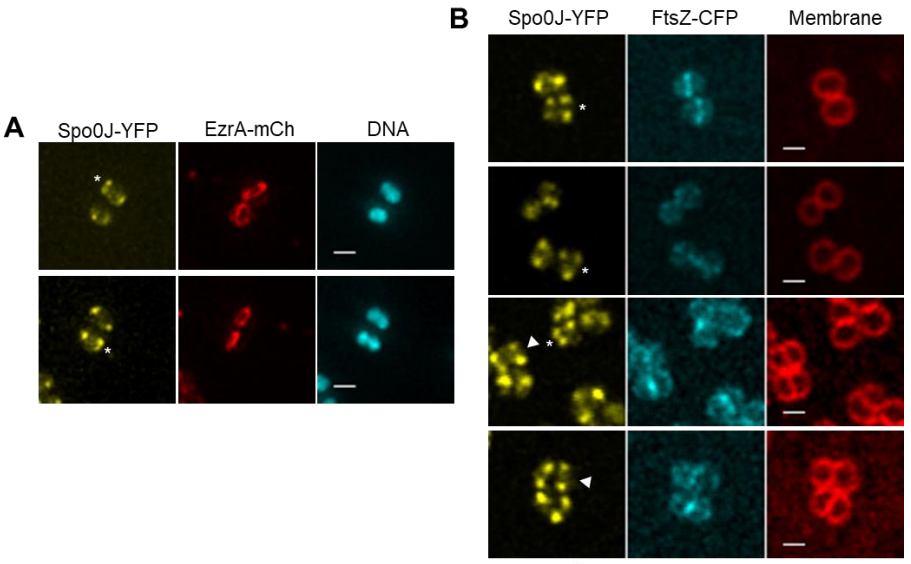

Figure 10. Chromosome's segregation precedes divisome assembly in daughter cells. A – Maximum projection of Z-stacks of deconvolved epifluorescence images of strain BCBAJ096 (COL expressing EzrA-mCherry and Spo0J-YFP fusions), labelled with the DNA dye Hoechst 33342. Spo0J binds near the chromosome origin of replication, so Spo0J-YFP localization can be used as a proxy for origin localization. Asterisks show cells where chromosome segregation in one of the daughter cells is observed prior to closure of the divisome ring. **B** – Confocal images of strain BCBHV005 (RN4220 expressing FtsZ-CFP and Spo0J-YFP fusions) labeled with the membrane dye FM5-95. Arrowheads show cells where chromosome segregation precedes divisome assembly in attached sister cells. Asterisks show cells where two origins can be observed in at least one of the future sister cells before any sign of membrane invagination at the division plane (11% of pre-septal cells, n=430 cells examined from three biological replicates). Scale bars, 1 μm.

5. Materials and Methods

5.1. Strains and growth conditions

Strains used in this study are listed in Table 1. *S. aureus* strains were grown in tryptic soy broth (TSB, Difco) at 200 rpm with aeration at 37 °C or on tryptic soy agar (TSA, VWR) at 37 °C. When necessary, culture media was supplemented with antibiotics (10 μg ml^{-1} erythromycin or 50 μg ml^{-1} kanamycin and 50 μg ml^{-1} neomycin), with 100 μg ml^{-1} 5-Bromo-4-chloro-3-indolyl β-D-galactopyranoside (X-gal, Apollo Scientific), with 0.1 mM isopropyl β-D-1-thiogalactopyranoside (IPTG, Apollo Scientific) or with 0.1 μM cadmium chloride (Sigma-Aldrich).

To introduce the *ezrA-sgfp* fusion in different *S. aureus* strains, pMAD-ezrAsgfp (Reichmann et al., 2019) was transduced into strains COL, NCTC8325-4 and JE2, using phage 80α as previously described (Oshida and Tomasz, 1992). Integration–excision of the plasmid resulted in the introduction of a 3′ *sgfp* fusion to the native copy of the *ezrA* gene. To construct COL *sfgfp-ftsK*, the plasmid pBCBHV017 (Veiga and Pinho, 2017) was transduced into COL followed by integration-excision which resulted in the introduction of a 5' *sgfp* fusion to the native copy of the *ftsK* gene.

To obtain strain BCBAJ096, the integrative plasmid pBCBHV004 (encoding a spo0J-yfp fusion, Veiga et al., 2011) was introduced into strain BCBAJ012 (COL ezrA:ezrA-mCherry, Jorge et al., 2011). The expression of *spo0J-YFP* in BCBAJ096 is under the control of the native promoter while a second copy of *spo0J* is under the control of the *Pspac* promoter.

Table 1. Strains used and constructed in this study

Strains	Description	Source
RN4220	Restriction-negative derivative of NCTC8325-4	(Mwangi et al., 2013)
NCTC8325-4	MSSA strain	R. Novick
USA300 JE2	CA-MRSA	(Fey et al., 2013)
COL	HA-MRSA	(Gill et al., 2005)
8325-4*sfgfp-ftsK*	NCTC8325-4 *ftsK::sfgfp-ftsK*	(Veiga and Pinho, 2017)
COL *sfgfp-ftsK*	COL *ftsK::sfgfp-ftsK*	This work
COL EzrA-sGFP	COL *ezrA::ezrA-sgfp*	This work
ColFtsZ$^{55\text{-}56}$sGFP	COL pCN-ftsZ$^{55\text{-}56}$sGFP; Kan^{r}	(Monteiro et al., 2018)
JE2 EzrA-sGFP	JE2 *ezrA::ezrA-sgfp*	This work
NCTC EzrA-sGFP	NCTC *ezrA::ezrA-sgfp*	This work
BCBHV005	RN4220 *ftsZ*::pBCBHV006 *spo0J*:: pBCBHV004, expressing *ftsZ-cfp* and *spo0J-yfp* fusions; Kan^{r}, Ery^{r}	(Veiga et al., 2011)
BCBAJ012	COL *ezrA::ezrA-mCherry*	(Jorge et al., 2011)
BCBAJ096	COL *ezrA::ezrA-mCherry spo0J*:: pBCBHV004, expressing *spo0J-yfp*; Ery^{r}	This work

5.2. Microscopy images acquisition

For time-lapse microscopy, overnight cultures of strain COL were back-diluted 1:500 in TSB and grown to mid-exponential phase (OD_{600nm}≈0.5). One milliliter of the culture was incubated for 5 min with the membrane dye Nile Red (5 μg ml^{-1}, Invitrogen) and the cell wall dye

wheat germ agglutinin conjugated to Alexa Fluor488 (WGA-488 1 µg ml^{-1}, Invitrogen), subsequently pelleted and resuspended in 20 µl TSB containing Nile Red (5 µg ml^{-1}, Invitrogen). One microliter of the labelled culture was then placed on a microscope slide covered with a thin layer of agarose (1.2% (w/v) in 1:1 phosphate buffered saline (PBS)/TSB solution). Time-lapse images were acquired every 20 min by structured illumination microscopy (SIM) in an Elyra PS.1 microscope (Zeiss) using a Plan-Apochromat 63x/1.4 oil DIC M27 objective. SIM images were acquired using three grid rotations, with 34 µm grating period for the 561 nm laser (100 mW) and 28 µm period for 488 nm laser (100 mW). Images were captured using a Pco.edge 5.5 camera and reconstructed using ZEN software (black edition, 2012, version 8.1.0.484) on the basis of a structured illumination algorithm (Heintzmann and Cremer, 1999).

For visualization of divisome proteins, overnight cultures of *S. aureus* strains were back-diluted 1:500 in TSB (supplemented with $CdCl_2$ in the case of ColFtsZ$^{55\text{-}56}$sGFP) and allowed to grow to an OD_{600nm} of approximately 0.8. One milliliter of each culture was pelleted and resuspended in 20 µl PBS. One microliter of this culture was then placed on a microscope slide covered with a thin layer of agarose (1.2% (w/v) in PBS). Z-stacks of 20-25 images, with a 110 nm increment, were acquired by SIM using an Elyra PS.1 microscope (Zeiss) and a 488 nm laser, as described above.

For time-lapse microscopy of fluorescent protein fusions with acquisition of a Z-stack at each time point (Supplementary Figure 6), cultures of COL EzrA-sGFP or ColFtsZ$^{55\text{-}56}$sGFP were grown to exponential phase in TSB or TSB supplemented with $CdCl_2$, respectively. One milliliter of each culture was pelleted and resuspended in 30 µl of TSB. One microliter of this culture was placed on a microscope slide covered with

a thin layer of agarose (1.2% (w/v) in PBS:TSB in a proportion of 3:2), incubated at 37°C in a DeltaVision OMX SR microscope (GE). Z-stacks of 19 images, with a Z step of 125 nm were acquired every 3 min by SIM using an Olympus 60X PlanApo N/1.42 oil objective. A 488 nm laser (100 mW) was used at 11-18 W cm^{-2} with an exposure time of 10 msec. The software AcquireSRsoftWoRx (GE) was used for image acquisition and reconstruction of the SIM images.

To image strain BCBAJ096, which expresses fluorescent derivatives of EzrA and Spo0J (fused to mCherry and YFP, respectively), cells were grown in TSB containing erythromycin and IPTG to an OD of 0.8. To label the DNA, 1 ml of the culture was incubated with the DNA dye Hoechst 33342 (1 μg ml^{-1}) for 5 min, pelleted and resuspended in 30 μl of PBS. Cells (1 μl) were placed on a thin layer of agarose (1.2% (w/v) in PBS) mounted on a microscope slide. Z-stacks of 21 epifluorescence images with a Z step of 125 nm were acquired using a DeltaVision OMX SR microscope (GE) with an Olympus 60X PlanApo N/1.42 oil objective. The fluorophores were excited with a 488 nm laser (100 mW), a 568 nm laser (100 mW) and a 405 nm laser (100 mW). The software AcquireSRsoftWoRx (GE) was used for image acquisition and deconvolution.

To image strain BCBHV005, which expresses fluorescent derivatives of FtsZ and Spo0J (fused to CFP and YFP, respectively), cells were grown in TSB supplemented with IPTG, kanamycin, neomycin and erythromycin to mid-exponential phase. One milliliter of cell culture was labelled with the membrane dye FM5-95 (250 ng ml^{-1}, Invitrogen) for 5 min, pelleted and resuspended in 20 μl PBS. Cells were placed on a thin layer of agarose (1.2% (w/v) in PBS) and imaged using a Zeiss LSM 880 inverted confocal laser scanning microscope with a Plan-Apochromat 63x/1.4 Oil DIC M27

objective. For YFP visualization, a 514 nm argon laser (25 mW) was used for excitation and wavelengths between 518-566 nm were detected using a gallium arsenide phosphide (GaAsP) detector. CFP and FM5-95 were imaged simultaneously; CFP was excited with a 458 nm argon laser (25 mW) and wavelengths between 462-556 nm were detected with a GaAsP detector, while FM5-95 was excited with a 561 nm laser (20 mW) and wavelengths between 650-758 nm were detected with a photomultiplier tube (PMT) detector. The gain was set to 700 for all detectors and the Zeiss Zen 2.3 (black edition) software was used for image acquisition. The smooth option of FIJI (Schindelin et al., 2012) was applied to the images.

5.3. Analysis of planes of division over two generations

The relative angle between consecutive planes of division was measured with FIJI (Schindelin et al., 2012) using time-lapse images of COL cells labelled with both WGA-488 and Nile Red. WGA-488 was used to determine the orientation of the previous division plane, defined as the line that connects the two ends of WGA-488 labelled region in each cell (see Figure 1a). Nile Red was used to determine the orientation of the current plane of division. The smallest angle between the plane of the septum and the previous division plane was measured for each cell. The average difference to 90° was also calculated.

5.4. Analysis of the orientation of divisomes in sister cells

The divisomes of two attached sister cells in dividing *S. aureus* cells showing a closed septum were visualized using GFP fluorescent derivatives of the divisome proteins FtsZ, EzrA or FtsK. The angle between divisomes assembled in attached sister cells was measured

using kymographs, generated using FIJI (Schindelin et al., 2012), obtained from Z-stacks of fluorescence images, by drawing a line crossing or overlapping the divisome of each sister cell, parallel to the flat region adjacent to the septum (see Figure 6A, B). A binary image of the kymograph was generated using a threshold corresponding to the 95 percentile of all pixel intensities. The coordinates of the pixels with an intensity above the threshold (considered as signal) were extracted and used as input data for a Principal Component Analysis (PCA) (Jolliffe and Cadima, 2016). The first principal component, corresponding to the eigenvector with highest eigenvalue, was used as the vector that defines the orientation of fluorescence signal in the kymograph. Two vectors were generated for each pair of sister cells (V_1 and V_2, for sister cells 1 and 2 respectively, see Figure 6C). The slope of the vector was corrected to account for the pixel size of the camera and the acquisition step between each Z-plane, by multiplying the x coordinates by the pixel size and the y coordinates by the Z-step. Vectors with a positive slope were considered to generate positive angles while vectors with negative slope generated negative angles. The smallest angle of V_1 and V_2 relative to the axis corresponding to the plane of microscopy imaging was measured for each pair of sister cells and named α_1 and α_2 (Figure 6C). The amplitude of the angle between the divisomes of pairs of sister cells was calculated as the absolute value of the difference between α_1 and α_2.

6. Bibliography

Emami, K., Guyet, A., Kawai, Y., Devi, J., Wu, L.J., Allenby, N., Daniel, R.A., and Errington, J. (2017). RodA as the missing glycosyltransferase in *Bacillus subtilis* and antibiotic discovery for the peptidoglycan polymerase pathway. Nature Microbiology 2017 2:3 *2*, 1–9.

Fey, P.D., Endres, J.L., Yajjala, K., Widhelm, T.J., Boissy, R.J., Bose, J.L., and Bayles, W. (2013). A genetic resource for rapid and comprehensive phenotype screening of nonessential *Staphylococcus aureus* genes. MBio *4*, 1–8.

Floc'h, K., Lacroix, F., Servant, P., Wong, Y.S., Kleman, J.P., Bourgeois, D., and Timmins, J. (2019). Cell morphology and nucleoid dynamics in dividing *Deinococcus radiodurans*. Nature Communications *10*, 3815.

Gill, S.R., Fouts, D.E., Archer, G.L., Mongodin, E.F., Deboy, R.T., Ravel, J., Paulsen, I.T., Kolonay, J.F., Brinkac, L., Beanan, M., et al. (2005). Insights on evolution of virulence and resistance from the complete genome analysis of an early methicillin-resistant *Staphylococcus aureus* strain and a biofilm-producing methicillin-resistant *Staphylococcus epidermidis* strain. Journal of Bacteriology. *187*, 2426–2438.

Heintzmann, R., and Cremer, C.G. (1999). Laterally modulated excitation microscopy: improvement of resolution by using a diffraction grating. Proc. SPIE 3568, Optical Biopsies and Microscopic Techniques III 185.

Jolliffe, I.T., and Cadima, J. (2016). Principal component analysis: a review and recent developments. Philosophical Transactions of the Royal Society A Mathematical, Physical and Engineering Sciences Sci *374*, 20150202.

Jorge, A.M., Hoiczyk, E., Gomes, J.P., and Pinho, M.G. (2011). EzrA Contributes to the Regulation of Cell Size in *Staphylococcus aureus*. PLOS ONE *6*, e27542.

Jun, S., and Wright, A. (2010). Entropy as the driver of chromosome segregation. Nature Reviews Microbiology *8*, 600–607.

Koyama, T., Yamada, M., and Matsuhashi, M. (1977). Formation of regular packets of *Staphylococcus aureus* cells. Journal of Bacteriology *129*, 1518–1523.

Meeske, A.J., Riley, E.P., Robins, W.P., Uehara, T., Mekalanos, J.J., Kahne, D., Walker, S., Kruse, A.C., Bernhardt, T.G., and Rudner, D.Z. (2016). SEDS proteins are a widespread family of bacterial cell wall polymerases. Nature *537*, 634–638.

Monodane, T., Matsushima, Y., Kotani, S., Monodane, T., Matsushima, Y., and Kotani, S. (1978). Process of consecutive cell divisions and separations in a regular tetrads-forming mutant of *Micrococcus lysodeikticus (luteus)*. Microbiology and Immunology *22*, 453–462.

Monteiro, J.M., Fernandes, P.B., Vaz, F., Pereira, A.R., Tavares, A.C., Ferreira, M.T., Pereira, P.M., Veiga, H., Kuru, E., Vannieuwenhze, M.S., et al. (2015). Cell shape dynamics during the staphylococcal cell cycle. Nature Communications *6*, 1–12.

Monteiro, J.M., Pereira, A.R., Reichmann, N.T., Saraiva, B.M., Fernandes, P.B., Veiga, H., Tavares, A.C., Santos, M., Ferreira, M.T., Macario, V., et al. (2018). Peptidoglycan synthesis drives an FtsZ-treadmilling-independent step of cytokinesis. Nature *554*, 528–532.

Mwangi, M.M., Kim, C., Chung, M., Tsai, J., Vijayadamodar, G., Benitez, M., Jarvie, T.P., Du, L., and Tomasz, A. (2013). Whole-genome sequencing reveals a link between beta-lactam resistance and synthetases of the alarmone (p)ppGpp in *Staphylococcus aureus*. Microbiology Drug Resistance *19*, 153–159.

Oshida, T., and Tomasz, A. (1992). Isolation and characterization of a Tn551-autolysis mutant of *Staphylococcus aureus*. Journal of Bacteriology *174*, 4952–4959.

Pinho, M.G., Kjos, M., and Veening, J.W. (2013). How to get (a)round: mechanisms controlling growth and division of coccoid bacteria. Nature Reviews. Microbiology *11*, 601–614.

van Raaphorst, R., Kjos, M., and Veening, J.W. (2017). Chromosome segregation drives division site selection in *Streptococcus pneumoniae*. Proceedings of the Nationall Academy of Sciences U S A *114*, E5959–E5968.

Ramirez-Arcos, S., Szeto, J., Dillon, J.A., and Margolin, W. (2002). Conservation of dynamic localization among MinD and MinE orthologues: oscillation of *Neisseria gonorrhoeae* proteins in *Escherichia coli*. Molecular Microbiology *46*, 493–504.

Reichmann, N.T., Tavares, A.C., Saraiva, B.M., Jousselin, A., Reed, P., Pereira, A.R., Monteiro, J.M., Sobral, R.G., VanNieuwenhze, M.S., Fernandes, F., et al. (2019). SEDS-bPBP pairs direct lateral and septal peptidoglycan synthesis in *Staphylococcus aureus*. Nature Microbiology *4*, 1368–1377.

Rowlett, V.W., and Margolin, W. (2015). The Min system and other nucleoid-independent regulators of Z ring positioning. Frontiers in Microbiology *6*, 478.

Schindelin, J., Arganda-Carreras, I., Frise, E., Kaynig, V., Longair, M., Pietzsch, T., Preibisch, S., Rueden, C., Saalfeld, S., Schmid, B., et al. (2012). Fiji: An open-source platform for biological-image analysis. Nature Methods *9*, 676–682.

Soderstrom, B., Badrutdinov, A., Chan, H., and Skoglund, U. (2018). Cell shape-independent FtsZ dynamics in synthetically remodeled bacterial cells. Nature Communications *9*, 4323.

Turner, N.A., Sharma-Kuinkel, B.K., Maskarinec, S.A., Eichenberger, E.M., Shah, P.P., Carugati, M., Holland, T.L., and Fowler Jr., V.G. (2019). Methicillin-resistant *Staphylococcus aureus*: an overview of basic and clinical research. Nature Reviews Microbiol *17*, 203–218.

Turner, R.D., Ratcliffe, E.C., Wheeler, R., Golestanian, R., Hobbs, J.K., and Foster, S.J. (2010). Peptidoglycan architecture can specify division planes in *Staphylococcus aureus*. Nature Communications *1*.

Tzagoloff, H., and Novick, R. (1977). Geometry of cell division in *Staphylococcus aureus*. Journal of Bacteriology *129*, 343–350.

Veiga, H., and Pinho, G.M. (2017). *Staphylococcus aureus* requires at least one FtsK/SpoIIIE protein for correct chromosome segregation. Molecular Microbiology *103*, 504–517.

Veiga, H., Jorge, A.M., and Pinho, M.G. (2011). Absence of nucleoid occlusion effector Noc impairs formation of orthogonal FtsZ rings during *Staphylococcus aureus* cell division. Molecular Microbiology *80*, 1366–1380.

Wu, L.J., and Errington, J. (2004). Coordination of cell division and chromosome segregation by a nucleoid occlusion protein in *Bacillus subtilis*. Cell *117*, 915–925.

Wu, L.J., and Errington, J. (2011). Nucleoid occlusion and bacterial cell division. Nature Reviews. Microbiology *10*, 8–12.

Yamada, M., Hirose, A., and Matsuhashi, M. (1975). Association of lack of cell wall teichuronic acid with formation of cell packets of *Micrococcus lysodeikticus (luteus)* mutants. Journal of Bacteriology *123*, 678.

Yamada, S., Sugai, M., Komatsuzawa, H., Nakashima, S., Oshida, T., Matsumoto, A., and Suginaka, H. (1996). An autolysin ring associated with cell separation of *Staphylococcus aureus*. Journal of Bacteriology *178*, 1565–1571.

Zhou, X., Halladin, D.K., Rojas, E.R., Koslover, E.F., Lee, T.K., Huang, K.C., and Theriot, J.A. (2015). Bacterial division. Mechanical crack propagation drives

millisecond daughter cell separation in *Staphylococcus aureus*. Science *348*, 574–578.

CHAPTER V

General discussion and future perspectives

Chapter V Summary

Over the past decades, fluorescence microscope techniques were developed to a point where we are now able to acquire images at a speed and resolution that was previously unheard of. The current bottleneck is often the analysis of the huge amount of data that we can currently acquire. Personally, this makes working on image analyses tools an extremely interesting and important challenge. By providing automated solutions that can reliably and accurately speed up the processing of all the acquired data, we can empower researchers working on biological questions and allow them to get the needed answers faster. This can be especially important when the questions are directly related to human health. The rise of antibiotic resistant infections caused by pathogens, such as *Staphylococcus aureus*, makes finding a solution for this problem an urgent matter. I sincerely hope the work described in this thesis enables a step further in the chase for solutions for this problem.

1. The need for unbiased and reproducible quantitative analysis

With the ongoing development of microscopy techniques, the need for the development of tools to automate processing and analysis of the generated data is rising. The capacity of the human brain is amazing and still unparalleled when compared to computational approaches. Nevertheless, the fact that our brains try to perceive patterns when analysing data can be problematic. The first model for the mode of division of *S. aureus* was based on work developed in the 1970s (Koyama et al., 1977; Tzagoloff and Novick, 1977). This model proposed that *S. aureus* cells divided in three alternating planes over three consecutive division cycles and was based on the microscopy observation that cells

would often organize in cell packets with a cubic three-dimensional arrangement (Koyama et al., 1977). Interestingly, in scanning electron microscopy images described in this work it is possible to observe cells that were not obeying to the inherent rules of the proposed model (Koyama et al., 1977). This observation was likely seen as an outlier and not considered to challenge the proposed mode of division.

A mode of division in three alternating perpendicular planes requires that cells retain some sort of "memory" of where they previously divided. Several efforts were made to find a mechanism to explain how cells could retain this information and keep dividing in the three sequentially orthogonal planes (Turner et al., 2010; Veiga et al., 2011). However, in Chapter IV we were able to show that cells do not always divide in three alternating orthogonal planes. In fact, more than two thirds of the cells do not follow the proposed model (Saraiva et al., 2020). This work was based on the careful measurement of the angles of division planes in sister cells and highlights the importance of basing models on quantitative data, instead of observations that are subjected to our own bias and predisposition to find patterns.

Another relevant problem that comes with manual analysis of data is reproducibility. The way two users perceive the features of cells can be different, leading to user bias. In Chapter II, we show that when we asked users to use the same dataset of single cell images to classify the cell cycle phase of each cell, we obtained differences in the frequency of cells in one cell cycle phase as high as 30% (Saraiva et al., 2021). While we can try to explain these differences based on the user experience or aversion to error, the key point is that user bias can impair the extraction of meaningful conclusions from data obtained from different users. Therefore, the development of automated tools that not only speed up the

analysis, but also remove any human bias that might interfere with the analysis, is essential to increase reproducibility. Even if an automated solution has its own bias, it will be a constant bias, independent of the number of times the data is analysed, ensuring the reproducibility of the analysis.

2. Current eHooke's capabilities and future development needs

eHooke, described in Chapter II, is a tool for the automated analysis of *S. aureus* images (Saraiva et al., 2021). It is capable of segmenting single cells, defining the subcellular regions, measuring both morphological and fluorescence features of singles cells and classifying their cell cycle phase. While eHooke is a powerful tool it has shortcomings and areas where it could be improved. In its current state, the graphical user interface tries to simplify the analysis process as much as possible in an effort to make it more accessible. In some cases, this design choice can be limiting. For example, eHooke currently only allows the user to load three different images, which can hinder some analyses. An interface like the one provided by ImageJ (Rueden et al., 2017; Schindelin et al., 2012) or Napari (Sofroniew et al., 2022) where users can load any number of images and then select which ones to use for each task is more flexible and eHooke's could either be updated to allow this or be remade as a plugin of either ImageJ or Napari in the future.

Currently, eHooke's segmentation of single cells is based on a combination of traditional thresholding algorithms, such as Isodata (Dias Velasco, 1980), and watershed (Roerdink and Meijster, 2000). This approach uses a set of variable parameters that users can manually adjust

to fine-tune segmentation and improve analysis, as segmentation is a key step for the automated analysis of cellular features. While, according to our experience, the parameters set by default in eHooke work well for the vast majority of *S. aureus* images, they still need to be adjusted for images of other bacteria, especially for bacteria with different cellular shapes. To make eHooke more inclusive in the type of organisms it can analyse, it would be important to automate the choice of parameters by using a machine learning approach capable of selecting the best parameters for the loaded images or by providing other segmentation approaches. As an alternative, the current segmentation approach could be replaced by segmentation based on deep learning models. Models such as StarDist (Schmidt et al., 2018; Weigert et al., 2020) have been shown to work well for this task, as well as several other deep learning models that are powerful tools for microscopy image segmentation (Spahn et al., 2021). As such, deep learning based approaches could potentially provide a more generalized solution to expand eHooke capabilities.

Although it is possible to use eHooke to measure morphological and fluorescence features of different organisms, its automatic cell cycle classification algorithm is restricted to *S. aureus* and requires labelling of cells with a membrane and DNA dye. Since this task is based on the training of an artificial neural network, it should be possible to retrain our model using a different labelling strategy or images of different organisms to expand eHooke cell cycle classifications capabilities. This task can be challenging to a user not familiar with programming, so providing an easy-to-use solution such as a Jupyter Notebook in Google Colab, similar to what ZeroCostDL4Mic (von Chamier et al., 2021) provides, could be an interesting alternative to help users with the model retraining.

eHooke's integrated artificial neural network model for automatic cell cycle classification of *S. aureus* cells was essential for the analysis of the data obtained in the screening of the Nebraska Transposon Mutant Library. Although the performance of the model is sufficient for our current needs, there are a few steps that could be taken to try to increase its classification accuracy. The training dataset could potentially be improved by providing users, tasked with manual classification of the images, with other fluorescence channels that can help them decide the cell cycle phase of each cell. For example, providing users with images of fluorescence derivatives of early and late divisome proteins could potentially provide cues that help assess whether a cell is still in Phase 1 or is in Phase 2, already starting to synthetise the septum. While these new fluorescence channels would be used to annotate the training dataset more accurately, to train the model we would still only use the channels corresponding to the membrane and DNA dyes, keeping them as the only requirement for the automatic classification performed by the trained model. Another thing that could potentially improve the model performance is changing how we deal with cell images for which users did not agree on the classification. In its current implementation, only cell images for which the majority of the users agreed on the cell cycle classification were used for training. This likely results in an underrepresentation of more ambiguous images, for example, images of cells in early and late Phase 2. An alternative could be to train the model using the probability of a cell being in each cell cycle phase, instead of the current implementation that uses a single defined classification for each cell. This would allow every image to be used for training as the classifications of every user would contribute to the probability of a cell being in a certain phase. While this would expand the training dataset to include images that are more ambiguous to classify, it could also

inadvertently include human errors as part of the training, as incorrect classifications would contribute to a probability of assigning the incorrect cell cycle phase. A network trained in this way would output the probability of a cell being in each of the three cell cycle phases. Using this to our advantage, instead of assuming that a cell would necessarily be one of the three phases, we could create subclasses of classifications. For example, if a cell would have a similar probability of being either phase 1 or phase 2, we could probably classify it as a transitory phase from 1 to 2. Alternatively, one could define a threshold for the probability of a cell being in one phase below which the classification would be considered inaccurate and the cell would be discarded from the analysis.

3. Chromosome segregation is key for cell cycle progression and morphogenesis

Although in recent years great advances have been made towards understanding how *S. aureus* cells grow and divide, there is still a lot more to be discovered before we have a full understanding of all the mechanisms responsible for the regulation of the cell cycle. One important step is certainly chromosome segregation. In this work, we found evidence that the axis of chromosome segregation might be the major factor that determines the localization of the plane of division in *S. aureus*. Contrary to the previous models that assumed an underlying mechanism to ensure division in three consecutive orthogonal planes (Turner et al., 2010; Veiga et al., 2011), we observed that staphylococcal cells can divide in any orientation as long as it remains perpendicular to the previous plane of division. This is likely because chromosome segregation occurs along an axis parallel to the previous division plane

and the nucleoid occlusion protein Noc, which preferentially binds the origin half of the chromosome, inhibits assembly of the divisome in its proximity (Wu and Errington, 2004, 2011). Therefore, the only plane of division which is not subjected to Noc inhibition is perpendicular to the axis of chromosome segregation and also perpendicular to the previous division plane. What mechanism, if any, controls the orientation of the axis of segregation remains unknown. In L-forms of *Bacillus subtilis* cell geometry plays a dominant role in defining the axis of chromosome segregation (Wu et al., 2020). Since chromosome segregation in *S. aureus* starts before cell splitting and each attached daughter cell is shaped as half of an ellipsoid (Chapter IV), chromosome segregation is probably favoured along the longer axis available inside each daughter cell. Alternatively, an unknown molecular mechanism may enforce chromosome segregation along an axis parallel to the septum. An interesting approach to try to identify this possible mechanism would be to measure the distribution of angles between planes of division of sister cells in the Nebraska Transposon Mutant Library (NTML, Fey et al., 2013). We would select mutants that were identified as showing DNA associated phenotypes (Chapter III) and compare the distribution of angles between planes of division of sister cells with the distribution obtained for wildtype strains. Mutants with an altered distribution of these angles may have transposon insertions in genes involved in a possible mechanism that defines the chromosome segregation axis.

Interestingly, one of the NTML mutants with most alterations in morphology and frequency of cell cycle phases, was SAUSA300_1792, with the transposon insertion in a gene encoding for a hypothetical protein with similarities to structural maintenance of chromosomes (SMC) protein family. SMC protein where previously shown to be involved in chromosome segregation in *S. aureus*, with the absence of

SMC resulting in a higher frequency of anucleate cells (Chan et al., 2020). The fact that a transposon insertion in a gene encoding for a hypothetical SMC protein, likely associated with chromosome segregation, corresponds to the mutant with the highest change in morphology and fourth in frequency of cell cycle phases, shows how important chromosome segregation is for morphogenesis and cell cycle regulation.

4. New strategies for fighting antibiotic resistant infections

Infections by antibiotic resistant bacteria are a rampant problem in our society. It is expected that this type of infections will be responsible for more than 300 million deaths over the next 30 years, making it a more frequent cause of death than cancer (O'Neill, 2014). *S. aureus* is one of the main culprits of these infections, mainly due to resistance to most the common class of antibiotics, β-Lactam antibiotics (Worthington and Melander, 2013). β-Lactams, such as penicillin and methicillin, act by inhibiting the synthesis of peptidoglycan. These antibiotics irreversibly bind to the to penicillin binding proteins (PBPs), preventing the final step of peptidoglycan crosslinking and disrupting cell wall synthesis (Fisher et al., 2005). Methicillin-resistant *S. aureus* (MRSA) have an extra PBP, PBP2a, with low affinity for β-Lactams and, as such, still capable of synthesising peptidoglycan when exposed to these antibiotics. Understanding the mechanisms behind cell morphogenesis and cell cycle progression could unveil new potential targets for new antibiotics, capable of dealing with current antibiotic resistant strains. FtsZ has been proposed as a potential suitable target (Kusuma et al., 2019), since its function is essential for cell division in most bacteria. PC190723, an FtsZ inhibitor, has been shown to effectively inhibit cell division in *S. aureus*,

including in multi-drug resistant strains (Haydon et al., 2008). This result shows how targeting other players involved in cell division or morphogenesis can be a viable strategy to fight antibiotic resistant infections. In this work, we identified several genes that are potentially involved in the cell cycle regulation of *S. aureus.* Considering the identified genes come from the NTML, which only contains transposon insertions in non-essential genes of *S. aureus* JE2 (Fey et al., 2013), it is unlikely that these genes can be used as primary targets for new antibiotics. However, these genes could still be good secondary targets for new antibiotics with synergistic effects with the ones currently available. During the cell cycle, bacteria undergo major morphological changes, and it is likely that they are more susceptible to antibiotics in certain stages of the cell cycle. By targeting cell cycle regulators, we could potentially trap cells in these vulnerable stages, making the action of antibiotics more effective and possibly overcoming their resistance.

5. Bibliography

von Chamier, L., Laine, R.F., Jukkala, J., Spahn, C., Krentzel, D., Nehme, E., Lerche, M., Hernández-Pérez, S., Mattila, P.K., Karinou, E., et al. (2021). Democratising deep learning for microscopy with ZeroCostDL4Mic. Nature Communications 2021 12:1 *12*, 1–18.

Chan, H., Söderström, B., and Skoglund, U. (2020). Spo0J and SMC are required for normal chromosome segregation in *Staphylococcus aureus*. MicrobiologyOpen *9*.

Dias Velasco, F.R. (1980). Thresholding using the ISODATA Clustering Algorithm. IEEE Transactions on Systems, Man, and Cybernetics *10*, 771–774.

Fey, P.D., Endres, J.L., Yajjala, K., Widhelm, T.J., Boissy, R.J., Bose, J.L., and Bayles, W. (2013). A genetic resource for rapid and comprehensive phenotype screening of nonessential *Staphylococcus aureus* genes. MBio *4*, 1–8.

Fisher, J.F., Meroueh, S.O., and Mobashery, S. (2005). Bacterial Resistance to β-Lactam Antibiotics: Compelling Opportunism, Compelling Opportunity†. Chemical Reviews *105*, 395–424.

Haydon, D.J., Stokes, N.R., Ure, R., Galbraith, G., Bennett, J.M., Brown, D.R., Baker, P.J., Barynin, V. v., Rice, D.W., Sedelnikova, S.E., et al. (2008). An inhibitor of FtsZ with potent and selective anti-staphylococcal activity. Science *321*, 1673–1675.

Koyama, T., Yamada, M., and Matsuhashi, M. (1977). Formation of regular packets of *Staphylococcus aureus* cells. Journal of Bacteriology *129*, 1518–1523.

Kusuma, K.D., Payne, M., Ung, A.T., Bottomley, A.L., and Harry, E.J. (2019). FtsZ as an Antibacterial Target: Status and Guidelines for Progressing This Avenue. ACS Infectious Diseases *5*, 1279–1294.

O'Neill, J. (2014). Antimicrobial resistance: tackling a crisis for the health and wealth of nations. Wellcome Collection.

Roerdink, J.B.T.M., and Meijster, A. (2000). The Watershed transform: definitions, algorithms and parallelization strategies. Fundamenta Informaticae *41*, 187–228.

Rueden, C.T., Schindelin, J., Hiner, M.C., Dezonia, B.E., Walter, A.E., Arena, E.T., and Eliceiri, K.W. (2017). ImageJ2 : ImageJ for the next generation of scientific image data. BMC Bioinformatics *18*, 1–26.

Saraiva, B.M., Sorg, M., Pereira, A.R., Ferreira, M.J., Caulat, L.C., Reichmann, N.T., and Pinho, M.G. (2020). Reassessment of the distinctive geometry of *Staphylococcus aureus* cell division. Nature Communications *11*, 1–7.

Saraiva, B.M., Krippahl, L., Filipe, S.R., Henriques, R., and Pinho, M.G. (2021). eHooke: a tool for automated image analysis of spherical bacteria based on cell cycle progression. Biological Imaging 1–25.

Schindelin, J., Arganda-Carreras, I., Frise, E., Kaynig, V., Longair, M., Pietzsch, T., Preibisch, S., Rueden, C., Saalfeld, S., Schmid, B., et al. (2012). Fiji: An open-source platform for biological-image analysis. Nature Methods *9*, 676–682.

Schmidt, U., Weigert, M., Broaddus, C., and Myers, G. (2018). Cell Detection with Star-convex Polygons. Lecture Notes in Computer Science (Including Subseries Lecture Notes in Artificial Intelligence and Lecture Notes in Bioinformatics) *11071 LNCS*, 265–273.

Sofroniew, N., Lambert, T., Evans, K., Nunez-Iglesias, J., Bokota, G., Bussonnier, M., Peña-Castellanos, G., Winston, P., Yamauchi, K., Pop, D.D., et al. (2022). napari/napari: 0.4.14.

Spahn, C., Laine, R.F., Pereira, P.M., Gómez-de-Mariscal, E., Chamier, L. von, Conduit, M., Pinho, M.G. de, Jacquemet, G., Holden, S., Heilemann, M., et al. (2021). DeepBacs: Bacterial image analysis using open-source deep learning approaches. BioRxiv 2021.11.03.467152.

Turner, R.D., Ratcliffe, E.C., Wheeler, R., Golestanian, R., Hobbs, J.K., and Foster, S.J. (2010). Peptidoglycan architecture can specify division planes in *Staphylococcus aureus*. Nature Communications *1*.

Tzagoloff, H., and Novick, R. (1977). Geometry of cell division in *Staphylococcus aureus*. Journal of Bacteriology *129*, 343–350.

Veiga, H., Jorge, A.M., and Pinho, M.G. (2011). Absence of nucleoid occlusion effector Noc impairs formation of orthogonal FtsZ rings during *Staphylococcus aureus* cell division. Molecular Microbiology *80*, 1366–1380.

Weigert, M., Schmidt, U., Haase, R., Sugawara, K., and Myers, G. (2020). Star-convex Polyhedra for 3D Object Detection and Segmentation in Microscopy. The IEEE Winter Conference on Applications of Computer Vision (WACV).

Worthington, R.J., and Melander, C. (2013). Overcoming Resistance to β-Lactam Antibiotics. The Journal of Organic Chemistry *78*, 4207.

Wu, L.J., and Errington, J. (2004). Coordination of cell division and chromosome segregation by a nucleoid occlusion protein in *Bacillus subtilis*. Cell *117*, 915–925.

Wu, L.J., and Errington, J. (2011). Nucleoid occlusion and bacterial cell division. Nature Reviews. Microbiology *10*, 8–12.

Wu, L.J., Lee, S., Park, S., Eland, L.E., Wipat, A., Holden, S., and Errington, J. (2020). Geometric principles underlying the proliferation of a model cell system. Nature Communications 2020 11:1 *11*, 1–13.

ITQB NOVA, Avenida da República, 2780-157 Oeiras, Portugal | Tel +351 214 469 100 | itqb.unl.pt